12-2011

Water Ice Films in Cryogenic Vacuum Chambers

Jesse Michael Labello
jlabello@utsi.edu

To the Graduate Council:

I am submitting herewith a dissertation written by Jesse Michael Labello entitled "Water Ice Films in Cryogenic Vacuum Chambers." I have examined the final electronic copy of this dissertation for form and content and recommend that it be accepted in partial fulfillment of the requirements for the degree of Doctor of Philosophy, with a major in Physics.

<div align="right">Christian G. Parigger, Major Professor</div>

We have read this dissertation and recommend its acceptance:

Horace W. Crater, Trevor M. Moeller, Lloyd M. Davis, Norman Mannella

<div align="right">Accepted for the Council:
Carolyn R. Hodges</div>

<div align="right">Vice Provost and Dean of the Graduate School</div>

(Original signatures are on file with official student records.)

Water Ice Films in Cryogenic Vacuum Chambers

A Dissertation

Presented for the

Doctor of Philosophy

Degree

The University of Tennessee, Knoxville

Jesse Michael Labello

December 2011

Dedicated to my lovely wife, Amanda, and my wonderful family.

Acknowledgements

I would like to thank Dr. Heard Lowry for steadfast support, guidance, and patience throughout my graduate career. I would also like to thank Dr. Christian Parigger for his belief in me and words of encouragement when I was stuck, and also for the rather desperately needed golf lessons. Thanks also to Dr. Horace Crater for allowing me to work with him on other topics in physics and expanding my knowledge and experience. I would like to thank all the members of my graduate committee for their attention and feedback. I would also like to thank the U.S. Air Force and Aerospace Testing Alliance for financially supporting me and other graduate students like me, special thanks to Jim Burns and John Prebola. Thanks to the outstanding members of the space chamber support group at AEDC, with special thanks to Ken Bynum, Stephen Cole, Danny Crews, Ben Klingler, and Dan Zielinski for sharing their expertise. Thanks to Jason King for pointing me towards Blender for the flux calculations, and I also need to thank my fellow graduate students William Ring and James Rogers for discussions, ideas, shared joy, and shared misery.

To achieve great things, two things are needed; a plan, and not quite enough time.

Leonard Bernstein

v

Abstract

The space simulation chambers at Arnold Engineering Development Complex (AEDC) allow for the testing and calibration of seeker sensors in cryogenic, high vacuum environments. During operation of these chambers, contaminant films can form on components in the chamber and disrupt operation. Although these contaminant films can be composed of many molecular species, depending on the species outgassed by warm chamber components and any leaks or virtual leaks that may be present, water vapor is most common, and it will be the focus of this dissertation. In this dissertation, some properties of the water molecule and low pressure ices are reviewed with a focus on the optical properties. The method of angular coefficients is utilized to calculate flux distributions for general three dimensional situations and the program written is applied to a model of the AEDC 10V space simulation chamber. The optical effects of varying amounts of contamination on a generic germanium window and gold mirror, along with the effects on two components specific to the space chambers, is determined. Also, an experiment to measure the thickness and other properties of contaminant films is discussed, and initial results are given for the first two tests of the experimental setup.

Contents

Approved for public release; distribution is unlimited.

List of Figures

Approved for public release; distribution is unlimited.

Introduction

Vacuum chambers are used in many experiments and industrial processes. A classification of vacuum is given by levels of pressure. While the S.I. unit for pressure is Pascal ($Pa = N/m^2$), Torr, which is equivalent to mmHg, is widely used. It is related to Pascals by 1 Torr = 133.32 Pa. Atmospheric pressure is 760 Torr. The levels of vacuum can be demarcated by physical parameters or characteristic quantities. As a guide, the different classifications are displayed in Figure 1. The applications of vacuum are many and varied. They stretch from manufacturing the reflective inserts in headlights and freeze drying to space simulation and nuclear fusion. Indeed, the
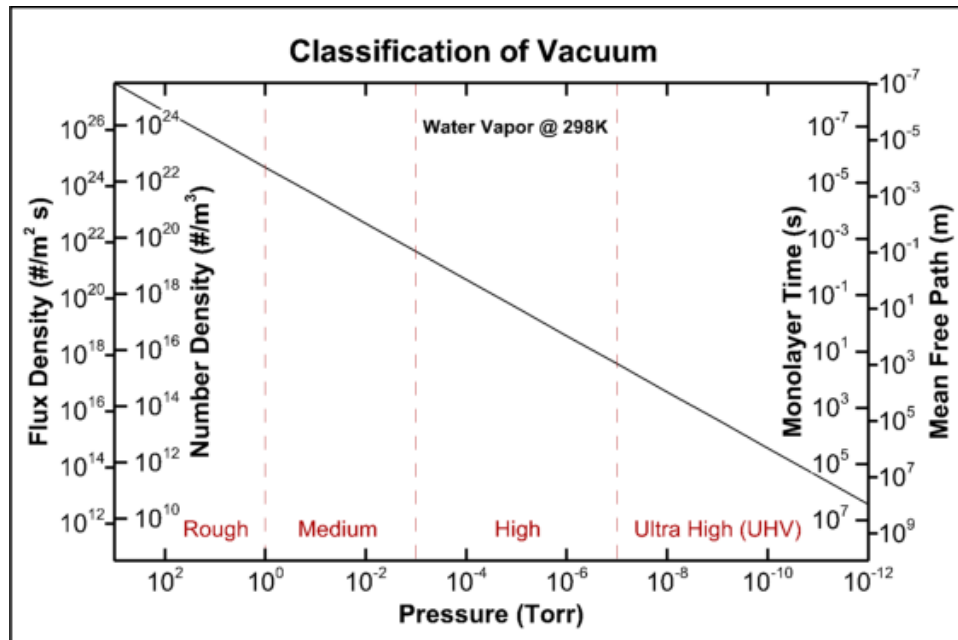
Figure 1: The levels of vacuum are displayed with associated quantities.

generation of vacuum has become an indispensable part of industry and research. A few examples of this are shown in Figure 2. No single type of vacuum pump can take a chamber from atmospheric pressures to UHV, a dynamic range of some 10^{10} Torr. Rather, pumps are designed to work within certain pressure ranges. The pumps that are employed at atmospheric pressure into the rough or medium vacuum ranges are termed 'roughing' pumps. If lower pressures are required, other pumps can be used to achieve high and ultra high vacuums. Figure 3 illustrates common vacuum pump types in use for different pressure regions.
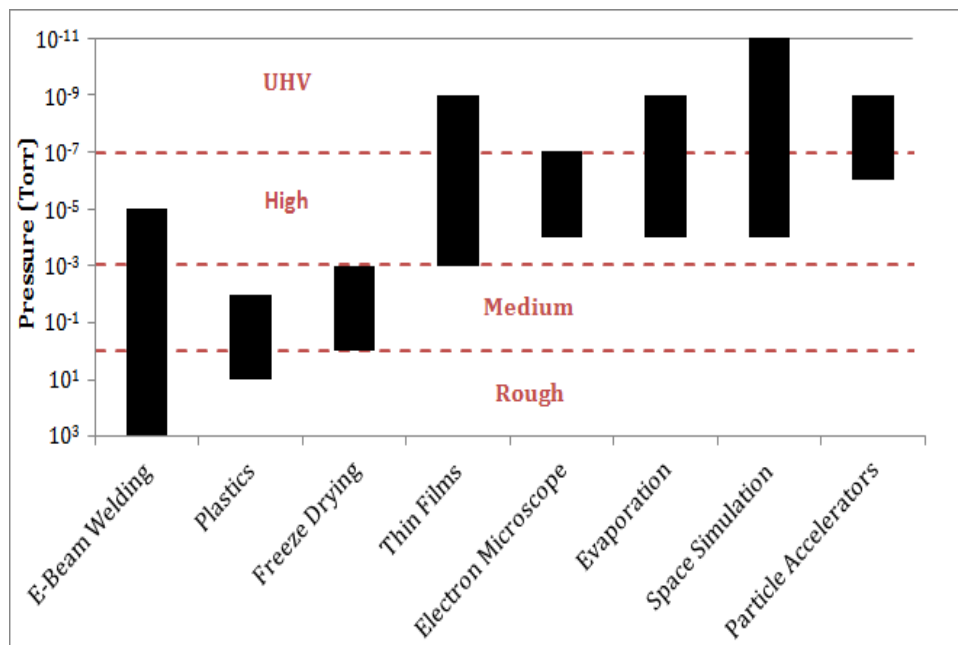
Figure 2: Some applications of vacuum and the common pressure ranges used in them. This figure is adapted from Figures 2.71 and 7.1 of Umrath (2007).

Cryogenic vacuum chambers are used in applications that require low pressures and low temperatures. These chambers are double walled. A vacuum is pulled in the volume contained by the outer wall. The inner wall is wrapped with cooling lines where a cryogen (typically liquid nitrogen (LN2) or gaseous helium (GHe)) can flow. Cooling the inner wall to cryogenic temperatures transforms the entire inner wall, and any surface in thermal contact with the inner wall, into a cryogenic capture
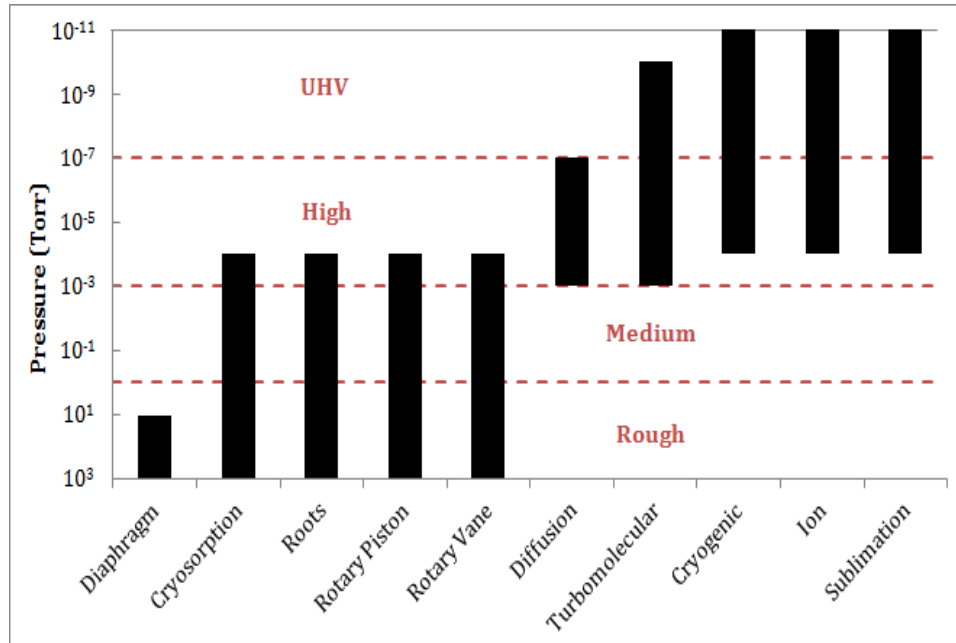
Figure 3: The normal working ranges of some common types of vacuum pumps. This figure is adapted from Figure 9.16 of Umrath (2007).

pump. At the low pressures and temperatures of a cryogenic vacuum environment most molecular species are below their triple points. As such, the sublimation curve is identical to the vapor pressure curve. Triple points and vapor pressure of some common gases are shown in Table 1 and Figure 4 respectively (Day (2007)).

The sensor test complex at Arnold Engineering Development Complex (AEDC) contains two primary space simulation chambers, 7V and 10V. The requirements for space simulation testing are driven by strenuous specifications for current surveillance, tracking, and interceptor sensor systems. The main objective of the chambers is to fully characterize infrared seekers and sensors. This is accomplished by providing visible to long-wavelength-infrared (LWIR), real-time, high-fidelity, threat simulation against mission backgrounds. The nominal operating conditions of both chambers is 10^{-6} Torr at 20K (Lowry et al. (2004, 2005)). The chambers contain extensive optical systems consisting of large, high-precision components that are cooled to the operating temperature. Figure 5 displays some details of the space simulation

3

Table 1: Triple points of some common gases. Helium does not have a solid state and, hence, no triple point.

Gas	Pressure (Torr)	Temperature (K)
H_2	52.5	14
O_2	1.1	54
N_2	93.8	63
CH_4	87.4	91
NH_3	45.8	196
CO_2	3825.3	217
H_2O	4.6	273
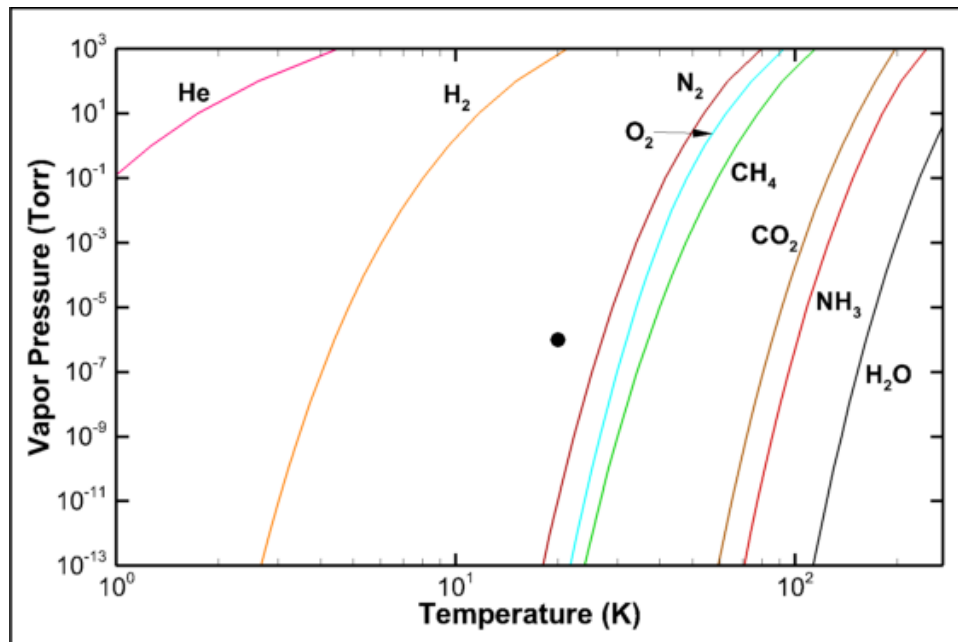
Figure 4: The saturation vapor pressure curves for some common gases (Honig and Hook (1960); AVS: Science & Technology of Materials, Interfacing, and Processing (2011)). The dot (•) marks the nominal operating point of the space chambers at AEDC.

4

chambers at AEDC. During cool down of the chambers, the optics can be maintained at a higher temperature than the walls to prevent gases from depositing on them. To begin tests however, the optics are cooled to wall temperatures. The chambers can run weeks at a time. With such long run times even small rates of leaking or outgassing can lead to significant build-up of ice (water or otherwise) on the optics. These cryodeposits can absorb, scatter, and cause unwanted optical interference in the system. This dissertation aims to provide methods for predicting and accounting for such cryodeposits. As inferred by Figure 4, these contaminant films can be composed of many species, just about anything besides hydrogen and helium, as most gases form a solid in the cryogenic vacuum conditions, however water vapor is by far the most prevalent species and it will be the primary focus.

5
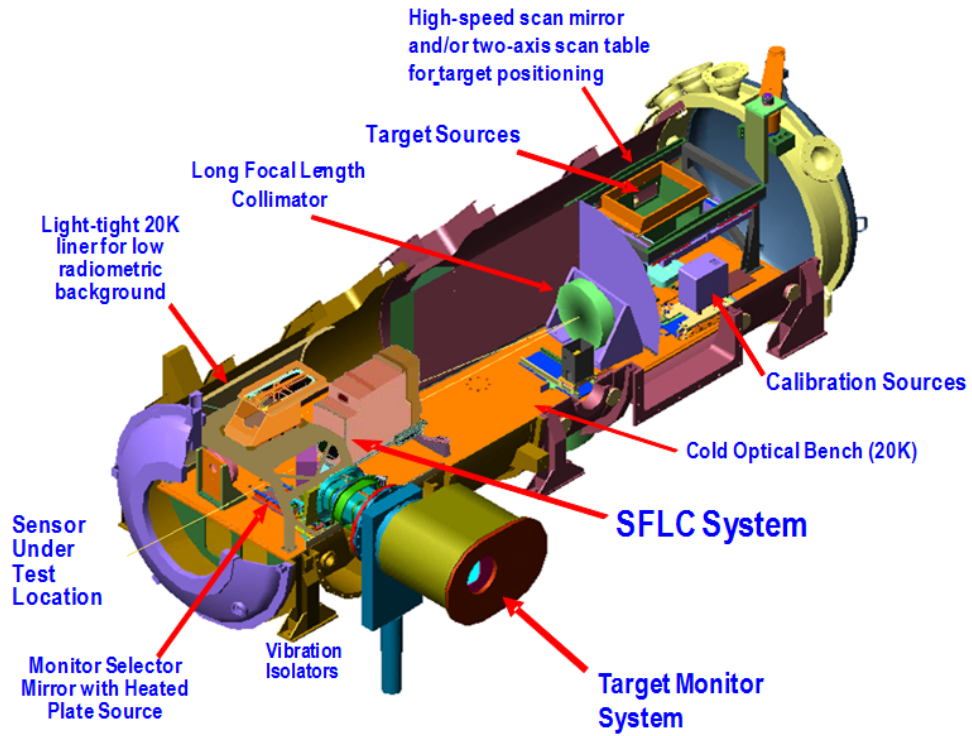
(a) A cutaway view of 7V. The dimensions are 7 feet in diameter by 21 feet long.
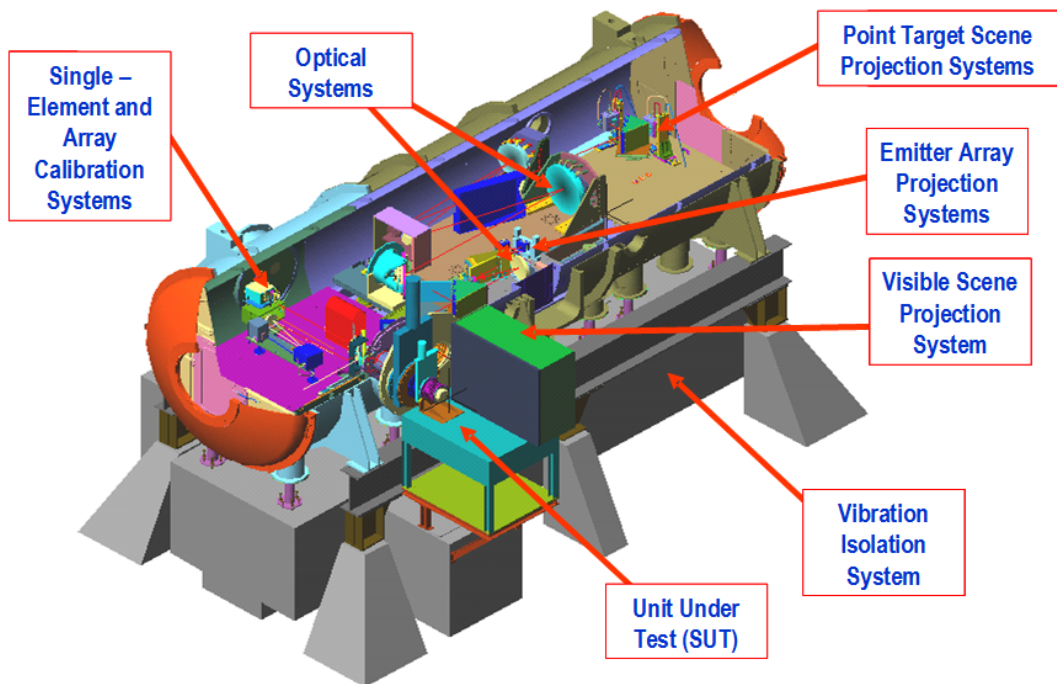
(b) A cutaway view of 10V. The dimensions are 10 feet in diameter by 30 feet long.

Figure 5: Isometric views of the two primary space simulation chambers at AEDC (Lowry et al. (2006)).

Chapter 1

Properties of Water Ice

Water is one of the most common and well-studied materials on the planet, yet it remains one of the least understood. The non-linear geometry of the water molecule leads to complex interactions and interesting properties. In solid form especially, the phases of water ice continue to fascinate and surprise scientists. For example, the newest form of ice discovered, very high density amorphous (VHDA), was only found in 1996 (Mishima (1996)). As another example, the most common form of ice, hexagonal I_h, has a structure that leaves some residual entropy. This leads to the belief that, although it is the most common, it is not the most stable. Cooling I_h doped with a catalyst to 60K at atmospheric pressure leads to ice XI, which is believed to be a more stable form. Ice XI has an intrinsic macroscopic dipole and one of the current open questions is whether ice XI is found in space as the electrical properties of grains of ice XI could lead to more rapid planet formation than current models predict (Grossman (2011)). This section reviews some of the properties of water and films of low pressure ice.

1.1   The Water Molecule

The water molecule is composed of two hydrogen atoms and an oxygen atom arrayed in a triangle. The mass of the most abundant forms of hydrogen and oxygen are 1

Approved for public release; distribution is unlimited.

and 16 amu respectively giving the H_2O molecule a mass of 18 amu or 3×10^{-26} kg. The hydrogen isotope deuterium, ^{2}H or simply D, can bond with oxygen to form heavy water in the form of either HDO or D_2O. The triangular configuration of the water molecule leads to a permanent electric dipole for the water molecule that contributes to many of the physical properties of water. The equilibrium O-H bond length, H-O-H angle, and electric dipole are shown in Figure 1.1 (Fletcher (1970)).
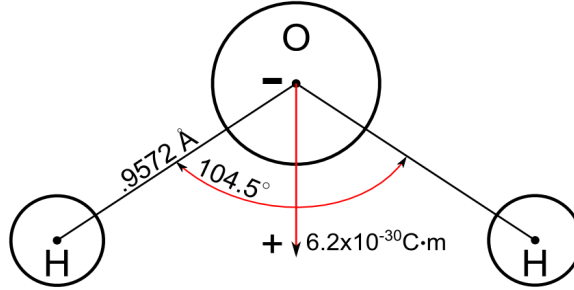
Figure 1.1: The geometrical structure of a water molecule.

As a 3 atom molecule, water has 9 degrees of freedom. Three of the degrees relate to translations and, as a molecule with non-linear geometry, three relate to rotations. The three remaining degrees of freedom are associated with the normal modes of vibration and are termed ν_1, ν_2, and ν_3 (see Figure 1.2). The vibrational spectrum of water is described by the expression for an anharmonic oscillator as

$$\frac{1}{hc}E(\nu_1, \nu_2, \nu_3) = \sum_{i=1}^{3}\gamma_i\left(\nu_i + \frac{1}{2}\right) + \sum_{i=1}^{3}\sum_{j\geq i}^{3}x_{ij}\left(\nu_i + \frac{1}{2}\right)\left(\nu_j + \frac{1}{2}\right), \qquad (1.1)$$

where the γ_i's are the harmonic wavenumbers and the x_{ij}'s indicate anharmonicity. Some values for these are shown in Table 1.1. The vibrational ground state energy is given by $E(0,0,0)$ and is $.58eV$ using the values in Table 1.1. The wavenumbers associated with the normal modes of vibration are given by the transition energy from

8

Table 1.1: Constants of the vibrational spectrum of the water molecule (Benedict et al. (1956)).

Property	cm^{-1}
γ_1	3832.17
γ_2	1648.47
γ_3	3942.53
x_{11}	-42.58
x_{22}	-16.81
x_{33}	-47.57
x_{12}	-15.93
x_{13}	-165.82
x_{23}	-20.33

the ground state to the normal mode (Hobbs (1974)),

$$
\begin{aligned}
\bar{\nu}_1 &= \frac{1}{hc}\left(E(1,0,0) - E(0,0,0)\right) = 3656\,cm^{-1}, \\
\bar{\nu}_2 &= \frac{1}{hc}\left(E(0,1,0) - E(0,0,0)\right) = 1597\,cm^{-1}, \\
\bar{\nu}_3 &= \frac{1}{hc}\left(E(0,0,1) - E(0,0,0)\right) = 3754\,cm^{-1}.
\end{aligned}
\tag{1.2}
$$

The strength of absorption by the vibrational modes depends on the strength of the restoring force. The O-H restoring force responsible for ν_1 and ν_3 is stronger than the H-O-H bond angle restoring force responsible for ν_2. As a result, water absorbs much more strongly at the wavenumbers near $\bar{\nu}_1$ and $\bar{\nu}_3$ than at $\bar{\nu}_2$ (see Figure 1.3).

(a) ν_1 **(b)** ν_2 **(c)** ν_3
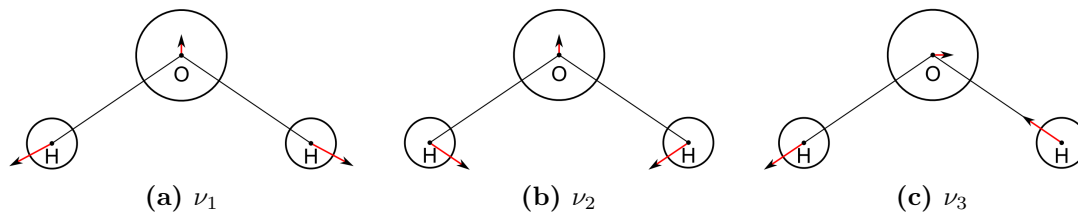
Figure 1.2: The normal vibrational modes of a water molecule.

9
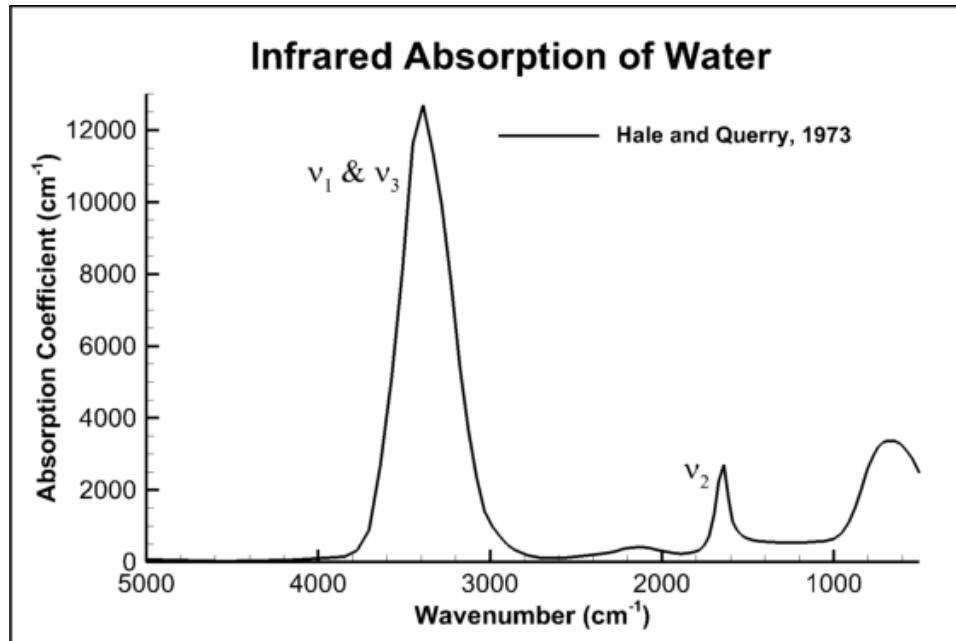
Figure 1.3: The infrared absorption spectrum of room temperature liquid water. This data is from Hale and Querry (1973).

1.2 Low Pressure Ice

The seemingly simple water molecule exhibits amazingly complex properties in its interactions. A well-known example is that water becomes less dense as temperature drops. Supercooled water at ambient pressure is less dense than water at 0°C and of course, the naturally occurring form of ice, I_h, is less dense than liquid water. There are at least 15 forms of ice including 12 crystalline and 3 amorphous. The resulting phase diagram for water and ice is complex and poorly understood to this day (Soper (2002)). The phase diagram even includes a well known fuzzy region called 'no man's land' between about 150K and 180K and at pressures $> 1MPa$ (see Figure 1.4) (Loerting et al. (2011)). This area is a region in which the homogeneous nucleation rate, the rate at which very pure water almost absent of crystallization inducing impurities changes phase, increases dramatically so that supercooled water has a very small lifetime (Debenedetti (2003)). In the low pressures and temperatures of cryogenic vacuum there are three forms of ice that are prevalent. These are cubic ice,
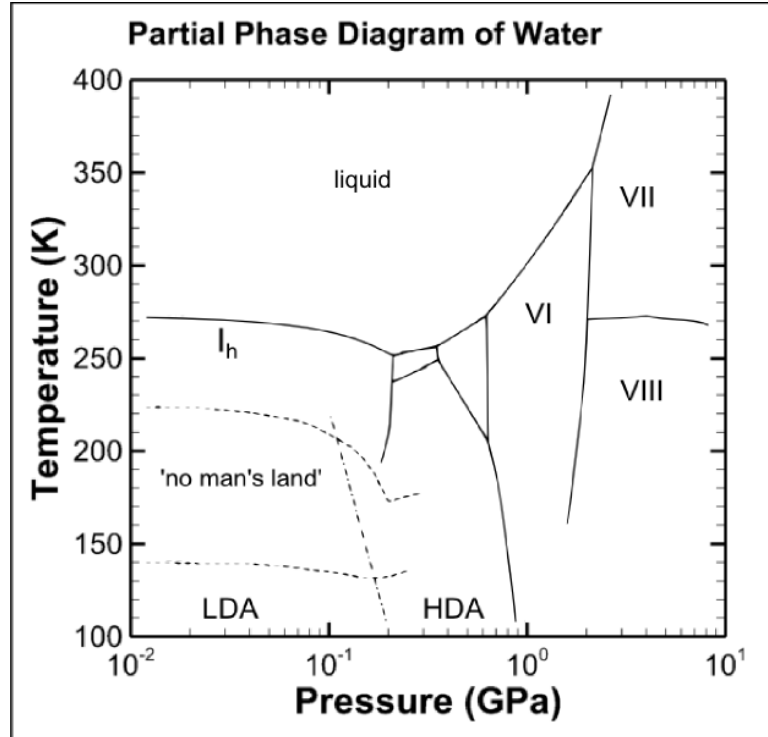
Figure 1.4: A partial phase diagram for water and ice. The roman numerals refer to various crystalline forms of ice. Data extracted from (Soper (2008)).

I_c, low density amorphous, LDA, and high density amorphous, HDA. The transitions between these forms, as with much concerning the forms of water and ice, are still the subject of some debate (for example, see (Drobyshev et al. (2007a,b); Jenniskens and Blake (1994))), however when vapor deposited in low pressure they typically form according to Table 1.2 (Loerting and Giovambattista (2006)).

Table 1.2: The ices that form in cryovacuum with their nominal densities and temperature ranges. The glass transition temperature, T_g, is 136K.

Form	Density $\left(\frac{g}{cm^3}\right)$	Temperature Range (K)
I_h	0.92	> 160
I_c	0.93	136 - 160
LDA	0.94	15 - 136
HDA	1.17	< 15

1.3 Optical Properties

As one of the most important and common molecules, the optical properties of water and ice have been measured in detail from the ultra-violet to the millimeter range and beyond (e.g. see Warren (1984)). While the majority of measurements for ice are for I_h near 0°C, the abundance of ice in the solar system has driven many studies of the optical constants of ice at lower temperatures including LDA and HDA (Prockter (2005)). In the visible wavelengths ice shows negligible absorption as attested to by the clarity of ice cubes when free of air bubbles. The infrared spectrum is much richer containing the fundamental vibrations of the molecule (see Figure 1.2) along with lattice vibrations and librations at wavelengths greater than $10\mu m$. Crystalline ice is *slightly* birefringent, however the birefringence is small enough to be ignored in most cases. Hexagonal and cubic ice display virtually identical optical spectra. In the visible region the refractive index of bulk hexagonal and cubic is almost constant at $n \approx 1.32$, while thin films of amorphous ice are closer to $n \approx 1.28$ (Hobbs (1974); Seiber et al. (1971)). The complex index of refraction is given by $\tilde{n} = n + ik$, where the real part n is simply called the refractive index and the imaginary part, k, is the extinction coefficient. The real and imaginary parts of the refractive index of various phases of low pressure ice are shown in Figure 1.5. Figure 1.6 shows the spectra for some other common gases.

1.4 Physical Properties

Vapor deposited ice forms through physisorption. Physisorbed molecules, as opposed to chemisorbed, are held by Van der Waals forces arising from, in water's case, the permanent electric dipole of the molecule. The dipole contributes to the strength of hydrogen bonds and each water molecule can form up to four hydrogen bonds. Chemisorption and physisorption are distinguished by the strength of the bond holding the molecules together (see Figure 1.7). This is called the energy (or
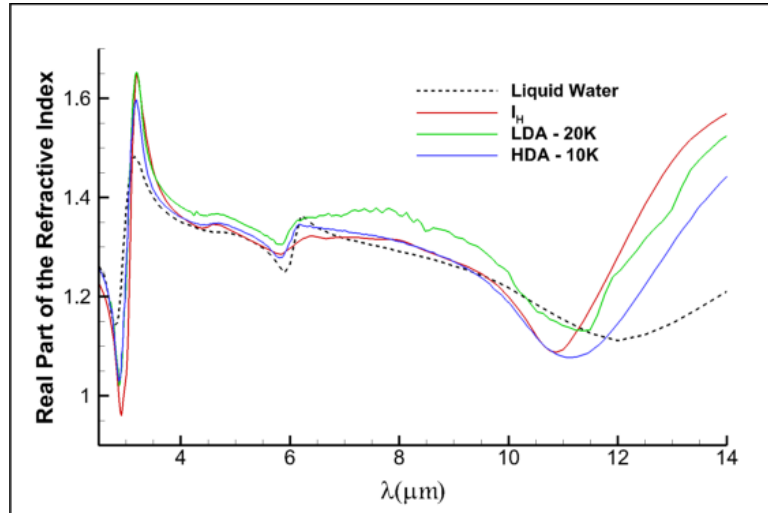
(a)
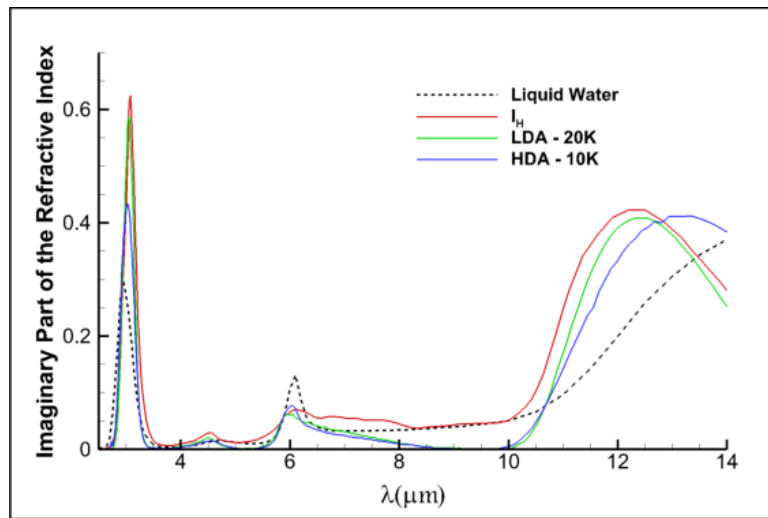
(b)

Figure 1.5: The real (a) and imaginary (b) parts of the infrared refractive index of liquid water, bulk hexagonal, and thin films of low density amorphous and high density amorphous ice (Hale and Querry (1973); Warren (1984); Hudgins et al. (1993); Roux et al. (1979)).

13
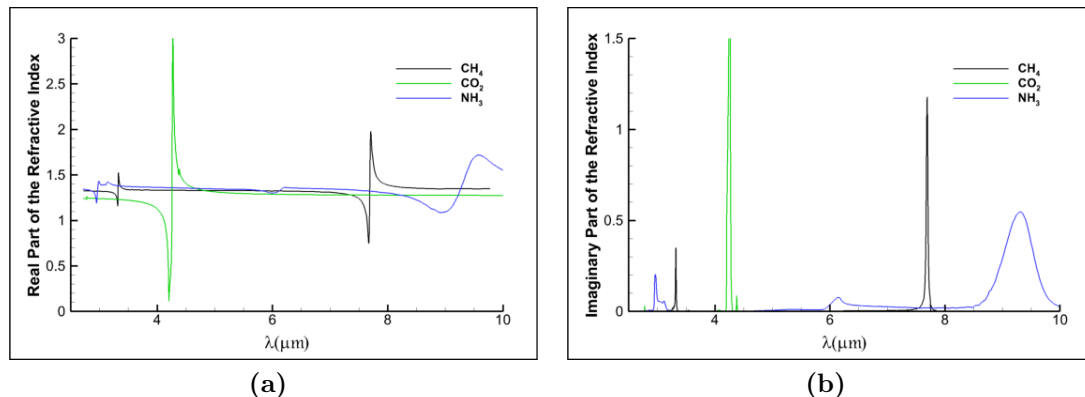
Figure 1.6: The real (a) and imaginary (b) parts of the infrared refractive index of 20K thin films of methane, carbon dioxide, and ammonia (Hudgins et al. (1993); Roux et al. (1979)).

heat) of adsorption, E_A. Physisorption is typically noted as having energies of adsorption less than $.25eV$ while greater energies of adsorption are typically attributed to chemisorption. The energy of adsorption for water ice is about $.45eV$. This particularly strong physisorption is due to the strength and number of the hydrogen bonds that the water molecule can create (Ohring (2001); Sack and Baragiola (1993)).
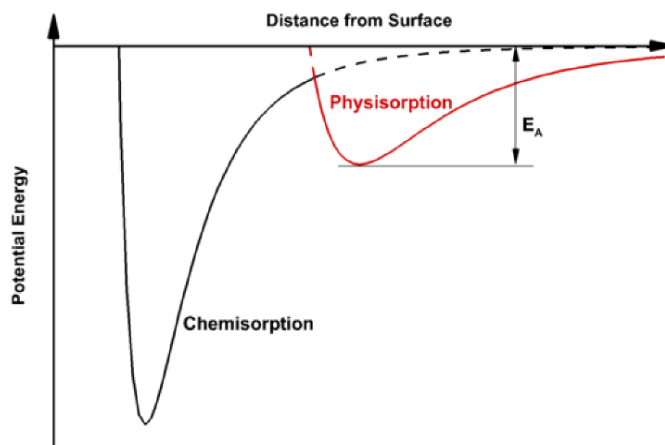
Figure 1.7: Schematic showing the interaction potentials of physisorption and chemisorption. The energy of adsorption, E_A, is the depth of the potential well.

14

Once molecules are on a surface they can diffuse both on the surface and into the bulk. Bulk diffusion is necessary for relaxation of ice into crystallized structures. As such, the glass transition temperature, T_g, is a good demarcation of the temperatures where bulk diffusion is negligible or appreciable. For water ice T_g is about 136K and marks where amorphous ice transitions into cubic ice. Diffusion is described by an Arrhenius expression as

$$D_B = D_0^B e^{-\frac{E_B}{k_B T}},$$ (1.3)

where D_B is the diffusion coefficient, E_B is the activation energy (or activation barrier) for bulk diffusion and k_B is Boltzmann's constant. For water molecules in ice the value of the preexponential, D_0^B, is about $10^8 \frac{cm^2}{s}$ and $E_B \approx 0.7eV$ (Brown and George (1996)). To quantify this, consider the time required for diffusion to occur over some distance d:

$$t = \frac{d^2}{2D_B}.$$ (1.4)

For crystalline ice the distance between bilayers serves as a good characteristic length and is about 3.7Å for I_h and I_c. Equation 1.4 is shown for this distance in Figure 1.8. Surface layer diffusion of water molecules on ice on the other hand has been measured as appreciable at temperatures well below T_g. The Arrhenius parameters for surface diffusion are less well known than bulk, but have been measured to be considerably lower with an activation energy in the range $E_S \approx .15 - .4eV$ and preexponential on the order of $D_0^S \approx 10^{-11} \frac{cm^2}{s}$. A consequence of the faster surface diffusion at low temperatures is that the morphology of the surface layer of an ice film may be different than that in the bulk and any chemical reactions occur preferentially on the surface of the ice (Jung et al. (2004); Nie et al. (2009); Park et al. (2010)).

The negligible bulk diffusion at low temperatures allows the simple growth model of ballistic deposition, 'hit and stick', to be useful in explaining certain features of
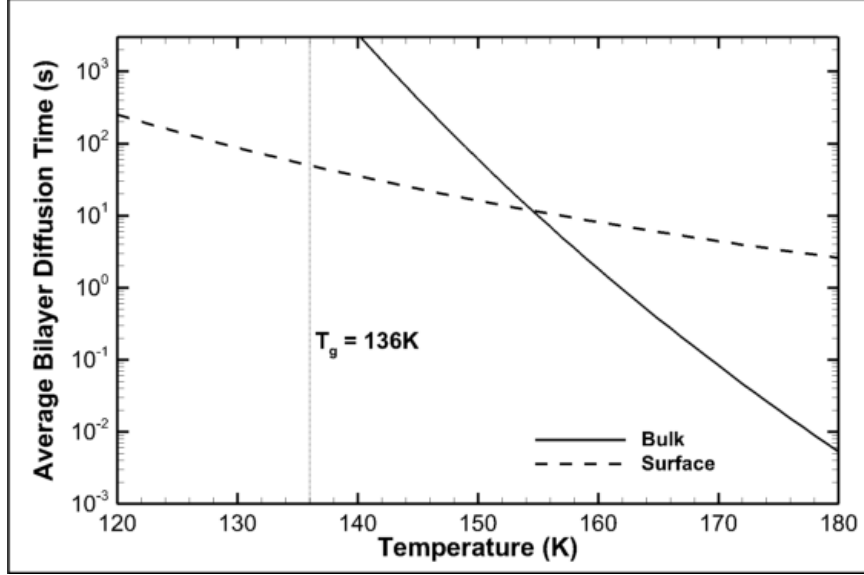
Figure 1.8: Representative time scale for bulk and surface self-diffusion of water ice as a function of temperature. Bulk diffusion is essentially frozen at temperatures less than 136K.

thin films of ice. For example, the density of an ice film grown in the lab can change depending on the geometry of the molecular source. This dependence is seen in ballistic deposition as the number and size of voids in the film (the porosity) depends on the source configuration (see Figure 1.9). Collimated molecular beams allow a measure of control over the porosity of the film by changing the angle of incidence. In general, the greater the angle of incidence the greater the porosity will be in the film (Kimmel et al. (2001)). Specifically, the porosity of a film is given by

$$p = 1 - \frac{\rho_a}{\rho_i},$$

(1.5)

where ρ_a and ρ_i are the densities of a porous film and the intrinsic density (pore free) of the same substance respectively. The refractive index of a non-absorbing film, in turn, is related to the porosity of a film through the Lorentz-Lorenz relation (Born

and Wolf (1964)):

$$p = 1 - \frac{n_a^2 - 1}{n_a^2 + 2} \cdot \frac{n_i^2 + 2}{n_i^2 - 1},$$ (1.6)

where n_a and n_i are the respective porous and intrinsic refractive indices. This allows the refractive index to be found as a function of density as

$$n_a^2 = \frac{2K\rho_a + 1}{1 - K\rho_a},$$ (1.7)

$$K = \frac{n_i^2 - 1}{\rho_i (n_i^2 + 2)},$$

where the value K is constant. For amorphous water ice the nominal density of 0.94 g/cm^3 (as measured by flotation in liquid oxygen (Ghormley and Hochanadel (1971)) is often used for ρ_i and the refractive index $n_i \approx 1.28$ in the visible region. Example data of the porosity dependent density and refractive index for thin films of amorphous ice is shown in Figure 1.10 as a function of molecular beam deposition angle, but the porosity in a film is not only dependent on the geometry, it can also be dependent on the film growth rate due to the difference in surface and bulk diffusion rates. Greater growth rates lead to more porous films as they allow less time for surface diffusion to occur as the surface layer will more quickly be buried under

(a) (b) (c)
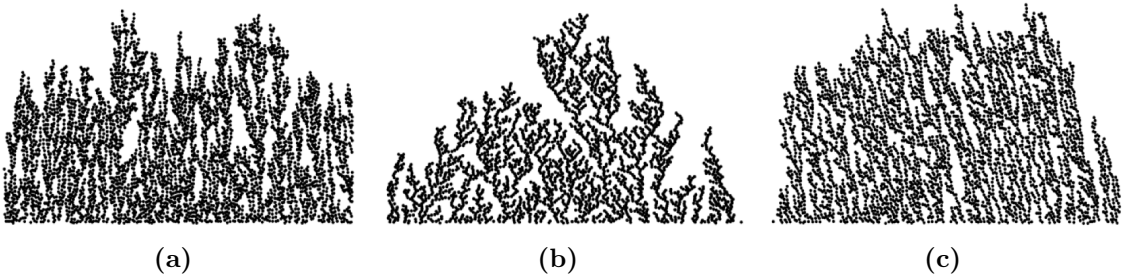
Figure 1.9: Computed examples of ballistic deposition from (a) the background (random), (b) a point source, and (c) a collimated beam at an angle to the deposition plate. Note the difference in porosity dependent on the source configuration.

another layer (incorporated into the bulk) and diffusion in that layer will stop. There are several examples of this type of measurement in the literature with some being shown in Figure 1.11. The porosity dependence of the density and refractive index leads to a fairly wide range of values reported at different temperatures depending on the experimental setup.
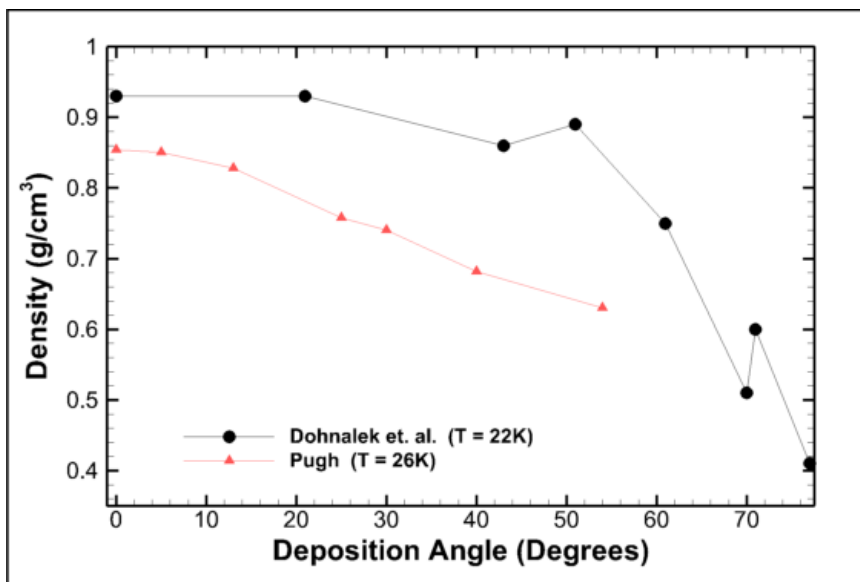
Figure 1.10: Density of LDA films vs molecular beam deposition angle (Dohnálek et al. (2003); Pugh (2003)).

Generally speaking the Lorentz-Lorenz relationship (Equation 1.6) does not typically apply to molecules with permanent dipoles such as water (Guenther (1990)). The relationship was derived assuming all dipoles were parallel and this is not generally the case. In hexagonal ice, for example, the dipoles are arranged equally in opposite directions so that there is no net polarization. However, as deposition temperature decreases and diffusion becomes limited the relaxation into a lower a potential configuration does not take place as rapidly. The result is that ice at low temperatures displays ferroelectric tendencies (spontaneous alignment of the dipoles). This is a current subject and a definitive theory has not emerged, however the most prominent current belief is that the substrate can interact with the first few monolayers of water molecules to partially align the dipoles. From there the electric

18
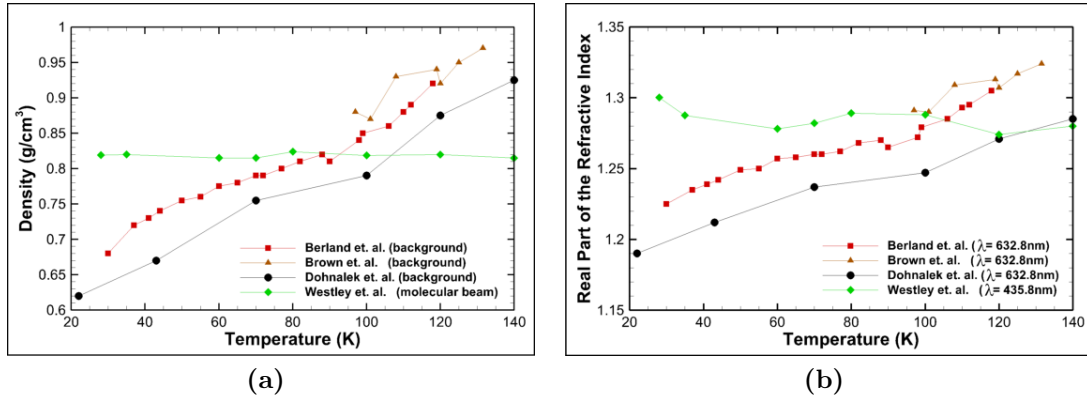
Figure 1.11: The density (a) and refractive index (b) of thin films of water ice as a function of temperature. Different experimental conditions can lead to a significant range of reported values at a given temperature (Berland et al. (1995); Brown et al. (1996); Dohnálek et al. (2003); Westley et al. (1998)).

field produced by the first few monolayers acts to align incoming molecules which cannot then relax into a lower potential configuration once in the bulk. Due to the large dipole moment of water molecules, even a small percentage of alignment can lead to large potentials across the film (see Figure 1.12). Annealing the films after deposition serves to decrease the film potential and the effect diminishes and then disappears at temperatures above the crystallization temperature (Iedema et al. (1998); Su et al. (1998); Wang et al. (2005); Bramwell (1999)).

1.5 Adsorption and Desorption

1.5.1 Thermal Desorption

For non-dissociative desorption (such that the molecules desorb as a whole rather than breaking up into, e.g., $H + OH$) the energy of adsorption E_A is equivalent to the energy of desorption (typically denoted E_{des}). Thermal desorption follows Arrhenius behavior such that

$$-\dot{N}^S = k_d(N^S)^m e^{-\frac{E_A}{k_B T}}, \tag{1.8}$$

19
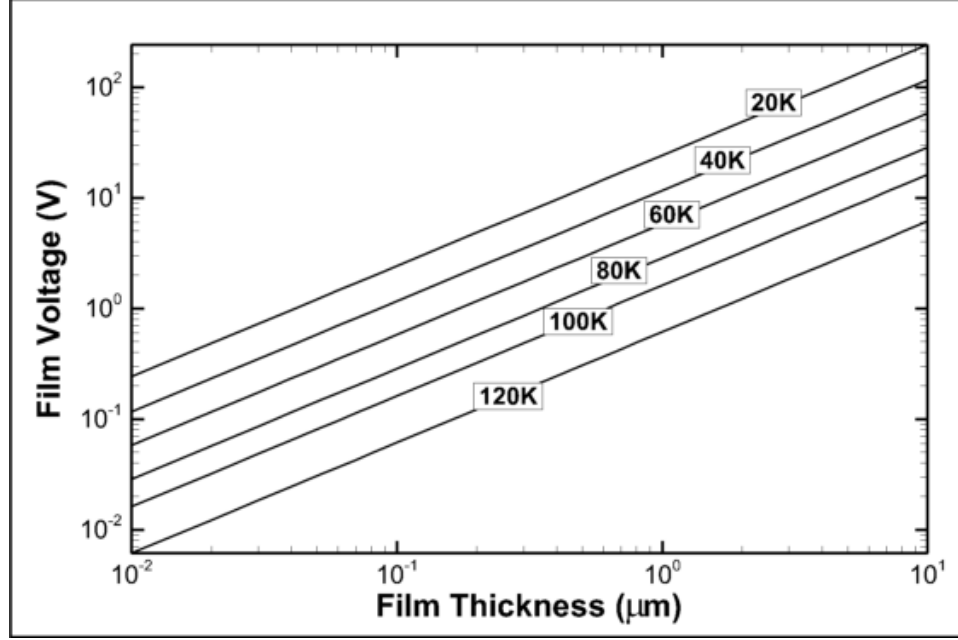
Figure 1.12: Display of the ferroelectric effect in thin films of LDA. The temperature dependence is due to a larger percentage of dipole alignment at lower temperatures. The alignment was estimated to vary from 0.4% at 20K to 0.01% at 120K. Films were grown with normal incidence molecular beams on a platinum substrate (Iedema et al. (1998); Wang et al. (2005)).

where N^S is the number of molecules per unit area $(\frac{\#}{cm^2})$ adsorbed on the surface, and m is the order of the reaction. Equation 1.8 is known as the Polanyi-Wigner equation. In temperature programmed desorption (TPD) experiments the temperature is set to a linear ramp such that

$$T(t) = T_0 + \beta t, \quad \text{and} \tag{1.9}$$

$$\frac{dT}{dt} = \beta.$$

Hence the change in desorption rate with temperature becomes

$$-\frac{dN^S}{dT} = -\frac{dN^S}{dt}\frac{dt}{dT} = \frac{k_d(N^S)^m}{\beta}e^{-\frac{E_A}{k_B T}}. \tag{1.10}$$

20

The order determines the dependence of the desorption curve on the coverage. For zero order kinetics the desorption curve is independent of the coverage and the desorption rate grows exponentially with temperature until all of the molecules are desorbed. Hence the leading edge of the desorption curve will be the same for all initial coverages and the peak will move to higher temperatures with increasing coverage. In contrast, in first order desorption the peak stays at the same temperature while the leading edge is dependent on the coverage. The reaction order for water ice films can be dependent on the substrate in special cases where particularly thin films are grown on hydrophilic materials (Smith et al. (1996)), but typically ice films follow zero order desorption kinetics with $k_d \approx 10^{30}$ $(cm^{-2}s^{-1})$ (Fraser et al. (2001); Haynes et al. (1992)). Of course the temperature range in which the desorption will occur is dependent on the pressure as in Figure 4. Some example TPD curves are shown in Figure 1.13.
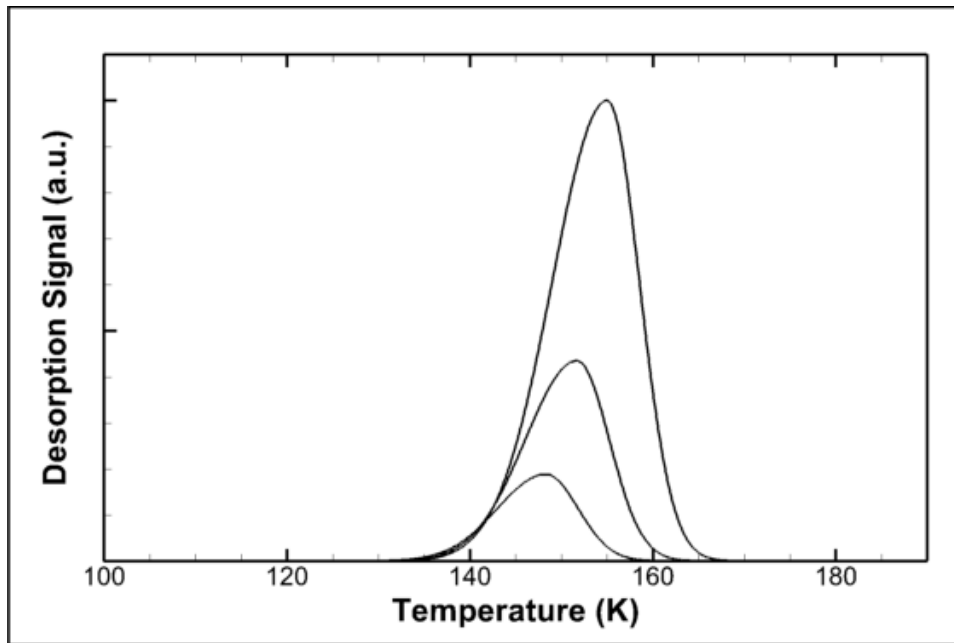
Figure 1.13: Example thermal desorption curves for thin films of water ice. The curves shown are for films grown in UHV ($\approx 10^{-11}$ Torr) with thicknesses of about 15, 30 and 75nm (in order of increasing magnitude). The similar leading edges and the movement of the peak with different initial coverages implies zero-order kinetics. Data extracted from Fraser et al. (2001).

1.5.2 Photodesorption

Photodesorption of ices is a rich subject of considerable interest to the astrophysical community as an explanation of the magnitude and constituents of gas clouds. In the UV, the desorption yield at constant fluence shows a fairly linear dependence on the temperature of the ice with the yield increasing with increasing temperature. The dependence on temperature goes deeper than that however, as the form of the dependence on fluence changes with temperature. At lower temperatures dissociative photodesorption dominates with products such as OH, HO_2, or H_2O_2 being readily produced. At warmer temperatures there is a combination of dissociative and non-dissociative desorption (Öberg et al. (2009); Westley et al. (1995)). In the infrared, fairly recently developed tunable sources such as optical parametric oscillators (OPO) and free electron lasers (FEL) have allowed the desorption of water ice to be studied across the $3\mu m$ absorption band. The desorption yield closely follows the absorption of ice (as seen in Figure 1.14) which indicates resonant desorption takes place. The dependence of the desorption yield on fluence appears to be linear above a certain threshold. Below the threshold little to no desorption occurs. The threshold fluence is a current subject of study and there does not appear to be a consensus value although most reports are on the order of 100 ($mJ\,cm^{-2}$) (e.g. see (Focsa et al. (2006, 2003); Krasnopoler and George (1998); Livingston et al. (2000); Bubb et al. (2010); Dreisewerd et al. (1995)). When pulsed lasers are used, the reported desorption depth per pulse is usually close to the optical penetration depth, $\lambda/4\pi k$, which is about $0.3\mu m$ at the peak of the absorption band.
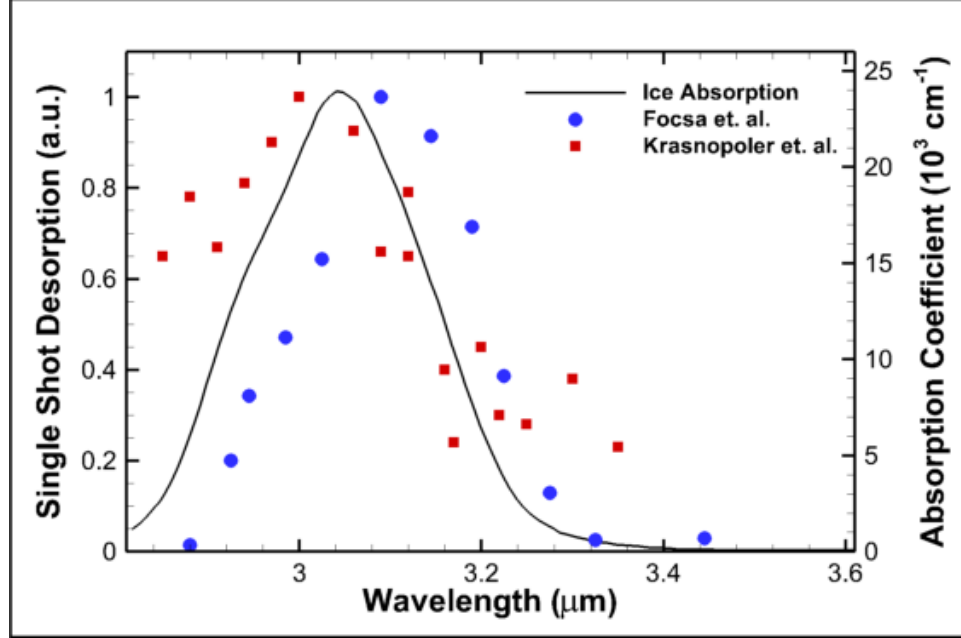
Figure 1.14: Example of infrared photodesorption of water ice. Krasnopoler (Krasnopoler and George (1998)) used a FEL with a pulse length on the order of a microsecond to desorb 110K ice. Focsa (Focsa et al. (2003)) used an Nd:YAG pumped OPO with a nanosecond pulse length on 100K ice. The ice absorption shown is for 100K (Hudgins et al. (1993)).

1.5.3   Sticking and Condensation Coefficients

If some flux density $(\frac{\#}{cm^2 s})$ of molecules is incident on a surface the molecules can either be reflected or adsorbed depending upon the sticking coefficient σ, i.e.

$$q_{ads} = \sigma q_{arr}, \quad \text{and} \tag{1.11}$$

$$q_{ref} = (1 - \sigma)q_{arr},$$

where q_{arr} is the flux density incident on the surface, q_{ads} is the percentage that stays on the surface and q_{ref} is the amount that is reflected. The sticking coefficient for water molecules on a cold surface is effectively independent of temperature as it is near unity for any temperature below the freezing point (Brown et al. (1996); Haynes et al. (1992)). The condensation coefficient is related to the sticking coefficient, but

Approved for public release; distribution is unlimited.

also accounts for desorption

$$\sigma_c = \frac{q_{ads} - q_{des}}{q_{arr}}. \tag{1.12}$$

At low temperatures, where desorption is negligible, the sticking coefficient and the condensation coefficient become identical. The growth rate of a film, given some incident flux density, is dependent on the condensation coefficient. For example for growth from the background the incident flux density is given by kinetic theory as

$$q_{arr} = \frac{n\langle v \rangle}{4} = \frac{P}{\sqrt{2\pi m k_B T}}, \tag{1.13}$$

where $\langle v \rangle$ is the average velocity of molecules in the gas, P and T are the pressure and temperature of the gas, and m is the molecular mass. The growth rate, η, of a film for this case is

$$\eta = \frac{\sigma_c m P}{\rho \sqrt{2\pi m k_B T}}, \tag{1.14}$$

where ρ is the density, g/cm^3, of the film. Given the zero-order desorption kinetics of ice, the condensation coefficient can be found as

$$\sigma_c = 1 - \frac{k_d \sqrt{2\pi m k_B T_g}}{P} e^{-\frac{E_A}{k_B T_s}}, \tag{1.15}$$

for deposition from the background where the sticking coefficient has been set to one and T_g and T_s are the gas and surface temperatures respectively. This is shown in Figure 1.15.

24
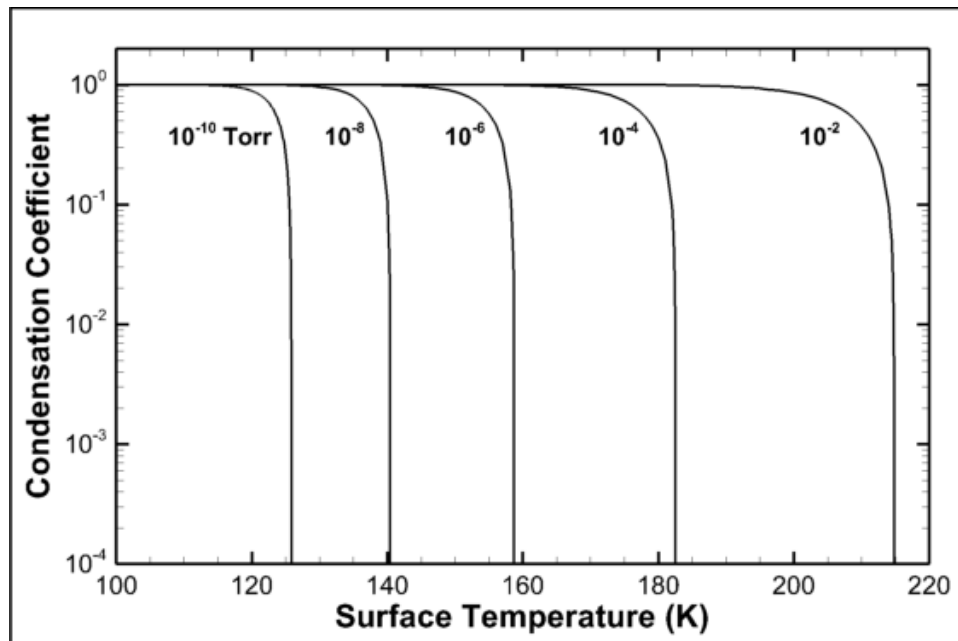
Figure 1.15: Condensation coefficient for water ice at various partial pressures of H_2O. This calculation assumes the gas temperature is a constant 298K.

Chapter 2

Calculation of Free Molecular Flux Distributions in General 3D Environments

One of the primary abilities needed for the space chambers, concerning contaminant ice films, is the ability to accurately predict where a given leak or outgassing object will deposit films. A method that can predict the growth rates throughout the chamber of contamination from any given source (or sources) is needed. The method must be easily adaptable to different geometries as the configurations in the chambers change and different sensors are tested. To this end, a program that applies the method of angular coefficients to calculate flux density distributions has been written as an add-on package for the 3D modeling program Blender[*].

The method of angular coefficients to calculate flux density distributions in free-molecular flow conditions is well known. For purely external flows, where no reflection feedback occurs, calculation of the angular coefficients is the only step required. For internal flows the angular coefficients must be calculated and the system must be iterated until a steady-state is achieved.

---

[*] Version 2.58a r38019, www.blender.org

2.1 Method of Angular Coefficients

This derivation follows the method found in Saksaganskii (1988). There are two conditions assumed:

- the flow is free molecular such that the mean free path of the molecules is greater than the dimensions of the system, and

- emission and reflection of molecules occurs according to the cosine law (i.e., diffusely).

Consider an infinitesimal area, dA_i, that has some flux density $q_{i_{lvg}}$ leaving from it. The cosine law states

$$dP = \frac{\mathbf{s} \cdot \mathbf{n}_i}{\pi s} d\Omega, \tag{2.1}$$

where dP is the probability that emission and/or reflection from dA_i will occur within solid angle $d\Omega$ about the radial vector $\mathbf{s}$, and $\mathbf{n}_i$ is the normal vector of dA_i (see Figure 2.1). The surface area of a sphere that subtends $d\Omega$ is given by $dA_s = s^2 d\Omega$, and the flux $(\#/s)$ arriving on that surface is

$$d\nu_s = \frac{q_{i_{lvg}} \mathbf{s} \cdot \mathbf{n}_i}{\pi s^3} dA_i dA_s, \tag{2.2}$$

where $q_{i_{lvg}} dA_i$ is the magnitude of the flux leaving dA_i. The flux arriving on some other surface area dA_j, at the same location as dA_s, is found by projecting the area on the sphere through $dA_s = -\hat{\mathbf{s}} \cdot d\mathbf{A}_j$, such that

$$d\nu_j = -\frac{q_{i_{lvg}} (\mathbf{s} \cdot \mathbf{n}_i)(\mathbf{s} \cdot \mathbf{n}_j)}{\pi s^4} dA_i dA_j. \tag{2.3}$$

The flux density on dA_j due to dA_i is given by $q_j = \frac{d\nu_j}{dA_j}$ and is

$$q_j = -\frac{q_{i_{lvg}} (\mathbf{s} \cdot \mathbf{n}_i)(\mathbf{s} \cdot \mathbf{n}_j)}{\pi s^4} dA_i, \tag{2.4}$$

27

and, hence, the total flux density arriving at dA_j due to the flux density leaving the entire area A_i is

$$q_j = -\frac{1}{\pi} \iint \frac{q_{i_{lvg}} \left(\mathbf{s} \cdot \mathbf{n}_i \right) \left(\mathbf{s} \cdot \mathbf{n}_j \right)}{s^4} dA_i, \qquad (2.5)$$

where $q_{i_{lvg}}$ can vary over A_i (Ohring (2001)).
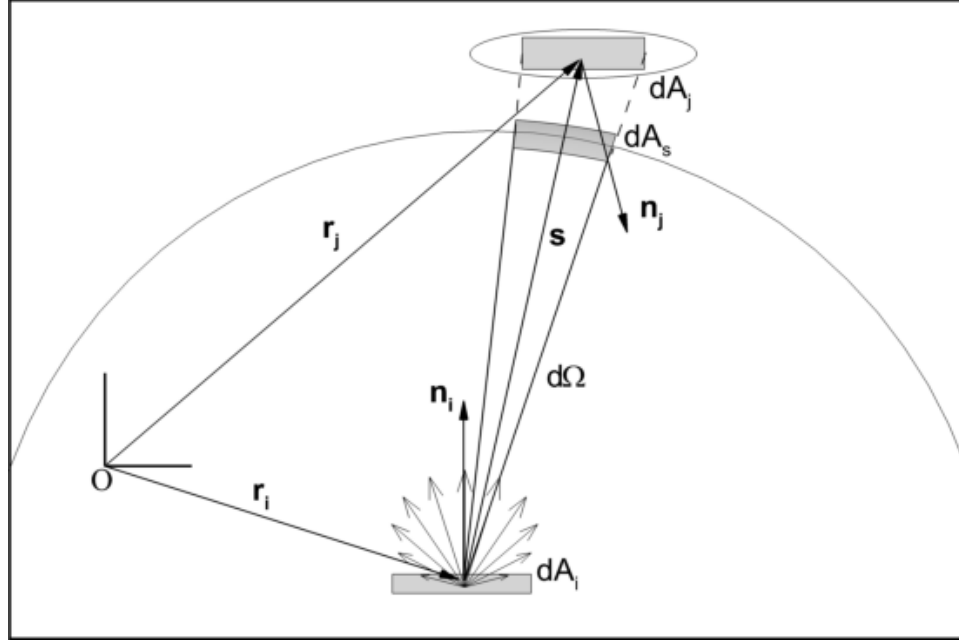
Figure 2.1: Geometry used to describe flux density distributions arising from diffuse scattering.

The flux density arriving at a point can either be adsorbed or reflected according to the sticking coefficient, σ (see Equation 1.11). The value $1 - \sigma$ is sometimes called the interaction or reflection parameter. The total amount of flux that leaves from a point is the sum of the reflected flux and whatever flux originates there, i.e.,

$$q_{lvg} = q_0 + (1 - \sigma) q_{arr}, \qquad (2.6)$$

where q_0 is the flux density originating from the point (outgassing). Using equation 2.5 in 2.6 gives the flux density leaving from the point at $\mathbf{r}_j$ in terms of the flux

density leaving A_i (Saksaganskii (1988)):

$$q_{j_{lvg}} = q_{j_0} + \frac{\sigma_j - 1}{\pi} \iint \frac{q_{i_{lvg}} (\mathbf{s} \cdot \mathbf{n}_i) (\mathbf{s} \cdot \mathbf{n}_j)}{s^4} dA_i. \qquad (2.7)$$

Upon inspection of equation 2.7 it is evident that the flux density leaving the area A_i will increase the amount of flux density leaving the area A_j (provided σ_j is not 1). Since the analysis can be carried out identically for points on A_i, the reverse is also true. The flux density leaving A_j will increase the flux density leaving A_i. Hence, to find accurate flux distributions the system must be iterated until a steady-state is achieved (see Figure 2.2), i.e.

$$q_{j_{lvg_{n+1}}} = q_{j_0} + \frac{\sigma_j - 1}{\pi} \iint \frac{q_{i_{lvg_n}} (\mathbf{s} \cdot \mathbf{n}_i) (\mathbf{s} \cdot \mathbf{n}_j)}{s^4} dA_i, \qquad (2.8)$$

where the subscript n is the iteration index.

(a) Initial Outgassing   **(b)** Iteration 1   **(c)** Return Flux

(d) Iteration 2   **(e)** Return Flux   **(f)** Iteration 3
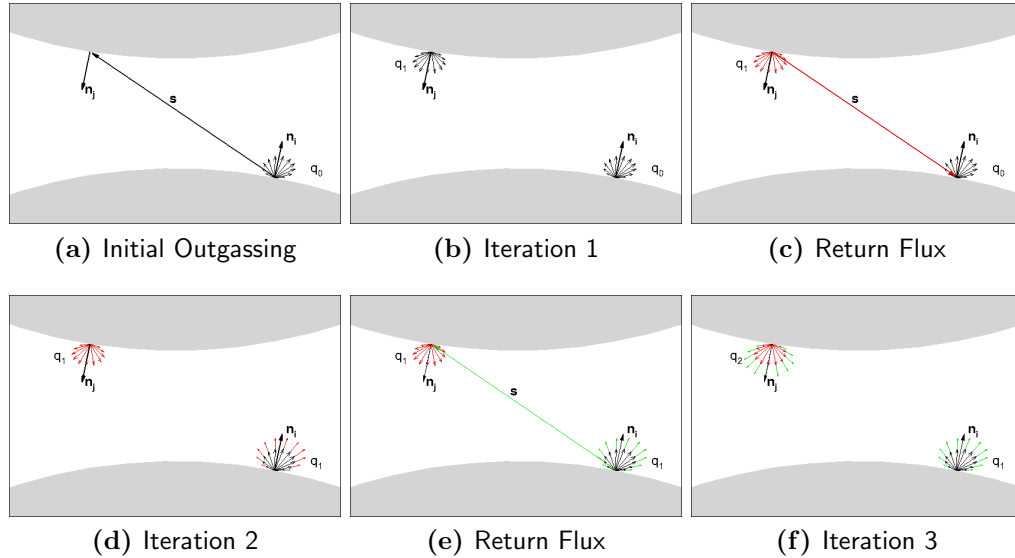
Figure 2.2: Illustration of the iteration sequence in the method of angular coefficients.

2.2   Integration into Blender

Blender is a free, open-source, 3D modeling software package (Hess (2010)). Blender is primarily used to create detailed images and animations for games, movies, or digital art. The primary benefit of Blender for numerical computations is that it comes with a built-in Python distribution. A user can access and manipulate object data (location, rotation, vertices, edges, faces, materials, textures, etc.) through Python code in addition to the user interface. The built-in Python distribution can be upgraded with packages such as NumPy and SciPy (Jones et al. (2001)) with a little work, although for purely geometrical manipulations this is not necessary. The built-in distribution contains Blender's own means of working with vectors and matrices along with several useful utility functions. Additionally, Blender provides tools for creating script user interfaces that are placed into Blender's user interface.

Mesh type objects in Blender are defined by vertices, edges, and faces. Vertices are the endpoints of edges and edges define the boundaries of faces. After the geometry is set in Blender, the program that has been developed, titled FMFlux, takes the faces of objects and calculates the points and weights necessary to use a 2D Gaussian integration routine to integrate over the faces following standard procedures (e.g. see (Landau et al. (2007))). Although there are many sophisticated numerical integration routines available, it is more practical in this application to use a custom routine so that the integration points and weights can be precalculated. The number of integration points to use (per face and per dimension) is a user option, although, since flux distributions are generally smooth functions, three point Gaussian quadrature (per dimension) is typically sufficient for external flows. Enclosed geometries may require more. The faces of objects in Blender are typically limited to being either triangles or quadrangles. For triangles, the procedure to assign the integration points is to arbitrarily pick a side as the base, then find the slope of the other two sides with respect to the chosen side. The location of the integration points along the base are calculated and the height of the triangle at each of those locations (perpendicular to

Approved for public release; distribution is unlimited.

the base) is found. Using that, the local coordinates of the integration points within the triangle are found. Once the location of the integration points is found, they are assigned the proper weight and the area of the triangle is found numerically by summing the weights. That area is compared to the analytic area of the triangle to find the error. The procedure is repeated twice more using the other sides of the triangle as the base. The distribution of integration points that gives the least error in the area of the triangle is the one chosen to be used in calculating flux distributions. General quadrangles are divided into two triangles and each triangle undergoes the same procedure. This method results in n^2 points being assigned to triangle faces and $2n^2$ points being assigned to general quadrangle faces, where n is the number of integration points per dimension being used. Rectangles are handled as special cases and only n^2 points are assigned to them (see Figure 2.3).
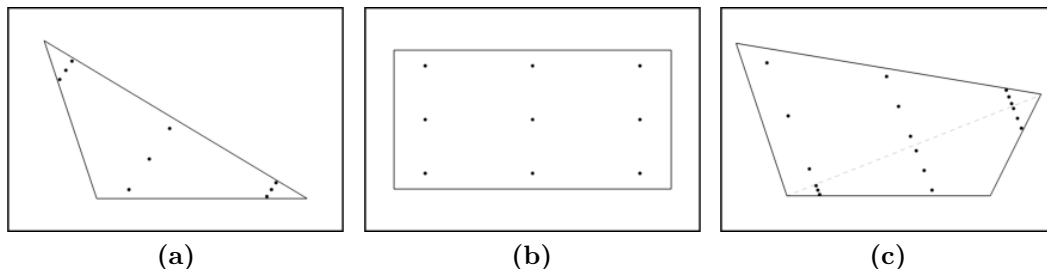
Figure 2.3: Example of the distribution of integration points on (a) triangle faces, (b) rectangle faces, and (c) general quadrangle faces using 3 point per dimension Gaussian quadrature.

After all of the integration points are distributed across the geometry, FMFlux allows users to set the surface properties (outgassing rate and sticking coefficient) by simply selecting a face, group of faces, or whole object and assigning the properties accordingly. This ease of problem setup is one of the biggest advantages of developing the code inside Blender rather than developing it externally and importing a mesh.

31

Let N be the total number of integration points assigned to all faces on all surfaces in any given scene and define F_{ij} as

$$F_{ij} \equiv \frac{\omega_j \left(\sigma_i - 1\right)}{\pi s_{ij}^4} \left(\mathbf{s}_{ij} \cdot \mathbf{n}_i\right) \left(\mathbf{s}_{ij} \cdot \mathbf{n}_j\right), \tag{2.9}$$

where ω_j is the weight assigned to the jth point. Then, in matrix form, Equation 2.8 becomes (Ossipov (1997))

$$\begin{bmatrix} q_{1_{lvg_{n+1}}} \\ q_{2_{lvg_{n+1}}} \\ q_{3_{lvg_{n+1}}} \\ \vdots \\ q_{N_{lvg_{n+1}}} \end{bmatrix} = \begin{bmatrix} 0 & F_{12} & F_{13} & \dots & F_{1N} \\ F_{21} & 0 & F_{23} & \dots & F_{2N} \\ F_{31} & F_{32} & 0 & \dots & F_{3N} \\ \vdots & \vdots & \vdots & \ddots & \vdots \\ F_{N1} & F_{N2} & F_{N3} & \dots & 0 \end{bmatrix} \begin{bmatrix} q_{1_{lvg_n}} \\ q_{2_{lvg_n}} \\ q_{3_{lvg_n}} \\ \vdots \\ q_{N_{lvg_n}} \end{bmatrix} + \begin{bmatrix} q_{1_0} \\ q_{2_0} \\ q_{3_0} \\ \vdots \\ q_{N_0} \end{bmatrix}. \tag{2.10}$$

Equation 2.10 is iterated until $q_{i_{lvg_{n+1}}} - q_{i_{lvg_n}} < \epsilon$ for all i, where ϵ is some arbitrarily small, positive, number.

One problem in developing this sort of program for general 3D situations is that the flux from some point cannot arrive at another point if the line of sight between them is blocked. For this type of application to be truly general with regards to geometry, it must have the ability to determine whether there is a clear line of sight between two points. This is another advantage in developing inside of a 3D modeling program like Blender. Blender provides ray casting functions attached to each mesh type object. Using ray casting, development of a dependable line of sight routine is straight forward. In a nutshell, each object inside Blender can perform a ray cast from any point to any other point. The ray cast determines whether a line between those two points passes through the object that performed the ray cast. So to check for a clear line of sight, every object in the scene performs a ray cast from every assigned integration point to every other integration point. As each point is assigned its own row in the $N \times N$ matrix in Equation 2.10, if the line of sight from that point to a second point is blocked, a zero is substituted into the row for the second point.

2.3 Test Cases

2.3.1 Point Source

Consider first the axisymmetric case of a single point source on some surface with normal n_1 diffusely emitting. A second surface lies parallel to the first surface a distance z away (see Figure 2.4). In this case the flux density is given analytically by

$$q_{1\to2} = \nu_{1_{lvg}} \frac{z^2}{\pi \left(z^2 + r^2\right)^2},$$

(2.11)

where r is the distance from the axis (Ohring (2001)). Note that this is a *directional* point source (Figure 2.4b) and is different than a point source that emits in all directions (Figure 2.4a). For a *free* point source, i.e. not on a surface, the probability distribution is given by

$$dP = \frac{d\Omega}{4\pi},$$

(2.12)

rather than Equation 2.1 (Holland and Steckelmacher (1952)). This leads to

$$q_{1\to2} = \nu_{1_{lvg}} \frac{z}{4\pi \left(z^2 + r^2\right)^{\frac{3}{2}}}.$$

(2.13)

Assuming no reflection from the second surface ($\sigma_2 = 1$) means that no iteration is necessary and the arriving flux density on the second surface is given by Equation 2.11. FMFlux allows the vertices of objects to be labeled as (directional) point sources so that pinhole leaks can be simulated. The normal vector assigned to the point source is the normalized sum of the normals of every face that shares the vertex. The results of the axisymmetric point source case agree well with the analytical solution and are displayed in Figure 2.5.

33

(a)   (b)
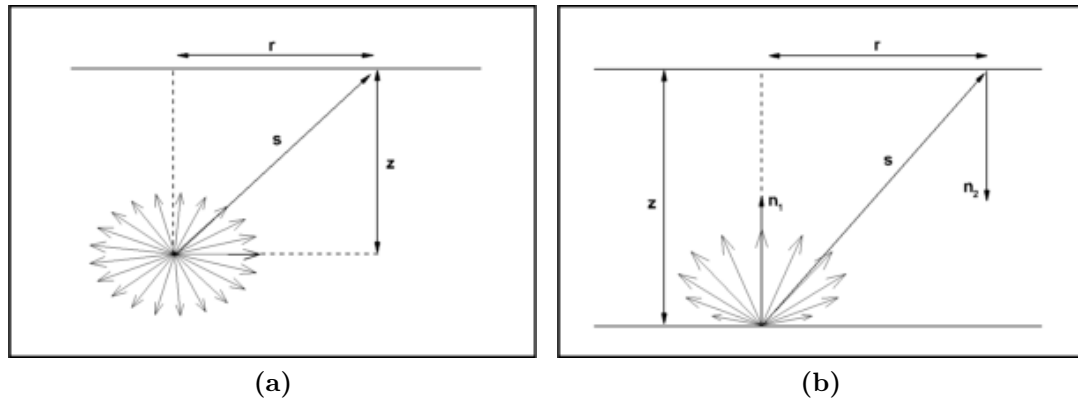
Figure 2.4: (a) a free point source, and (b) a directional point source.

(a)   (b)
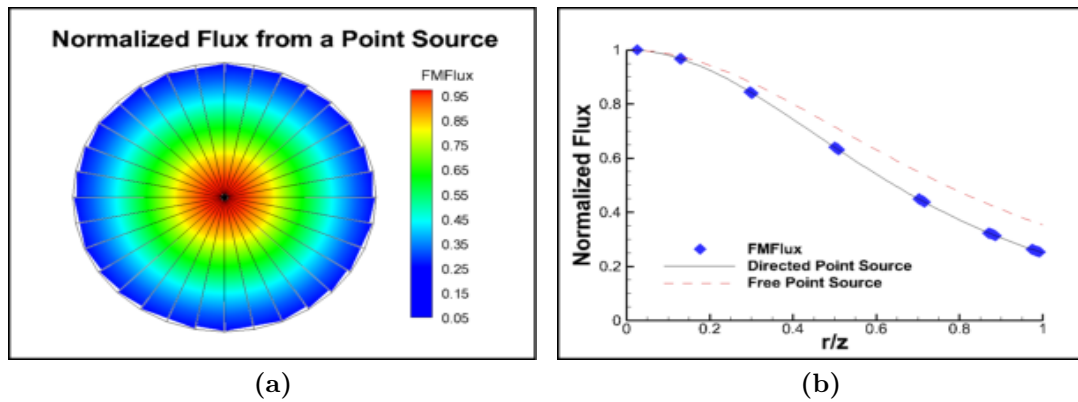
Figure 2.5: Results for an axisymmetric point source. (a) shows the full (normalized) results from FMFlux while (b) compares a cross section of the results to the analytical result, Equation 2.11, and shows the analytical result for a free point source, Equation 2.13 for comparison. The normalized flux is given here by $q_{1\rightarrow2}\left(\frac{\pi z^2}{\nu_{1_{lvg}}}\right)$ for the directional point source and by $q_{1\rightarrow2}\left(\frac{4\pi z^2}{\nu_{1_{lvg}}}\right)$ for the free point source.

2.3.2 Parallel Planes

Next, consider the same situation as Figure 2.4b, except instead of a single point source allow the entire first surface to outgas uniformly and limit it's extent to a radius R perpendicular to z. The flux at the center point of the receiving plane is easily calculated as

$$\frac{q_{center}}{q_{1_{lvg}}} = \frac{1}{\pi} \int_0^{2\pi} \int_0^R \frac{z^2}{r^2 + z^2} r dr d\theta = 1 - \frac{1}{\frac{R^2}{z^2} + 1}, \tag{2.14}$$

so, for $Z = R$, the normalized flux value there is 0.5. Rather than trying to solve for the rest of the receiving plane directly, a simulation of the situation was performed in the 2D/Axisymmetric DSMC code DS2V (Bird (2005)). The results from DS2V and FMFlux show excellent agreement and are displayed in Figure 2.6.

(a) (b)
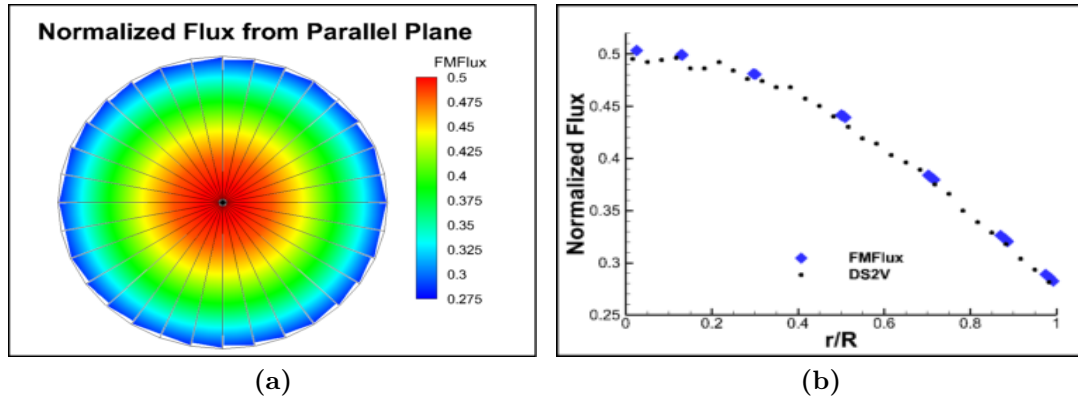
Figure 2.6: Results for the axisymmetric case of two parallel planes with $Z = R$. (a) shows the full results from FMFlux while (b) compares a cross section of the results to results from DS2V.

2.3.3 Open Cylinder

A good example of an axisymmetric situation that requires iteration of Equation 2.8 is an open cylinder that outgasses internally. For this case, let the length of the cylinder be Z, the radius R, and set the ratio $Z/R = 2$. For simplicity let the

initial outgassing distribution be uniform. The leaving flux distribution after selected iterations are shown in Figure 2.7. The steady-state results from FMFlux and DS2V again shown excellent agreement and are shown in Figure 2.8.

| (a) | (b) | (c) |
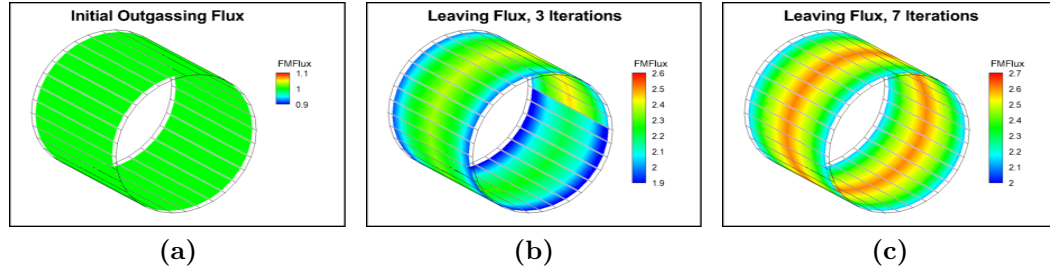
Figure 2.7: Results from FMFlux while iterating Equation 2.10. (a) is the initial, uniform, distribution. (b) is after 3 iterations, and (c) is after 7 iterations. As Equation 2.10 is iterated, the $n+1$ value is substituted for the n value as each point is calculated. This leads to the clear demarcation of the first face done (blue and green), and the last face (green, yellow, and orange) seen in (b).

| (a) | (b) |
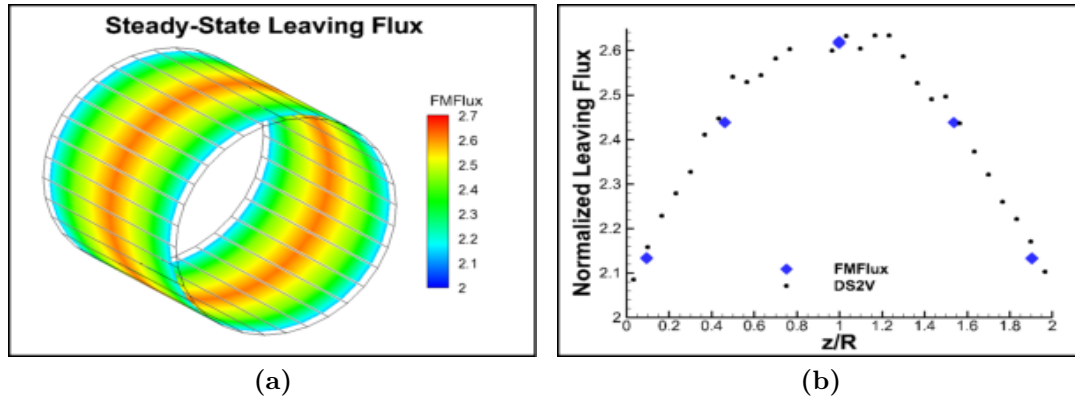
Figure 2.8: Results for the axisymmetric case of a cylinder with $Z/R = 2$ outgassing internally with an intially uniform distribution. (a) shows the full results from FMFlux while (b) compares a cross section of the results to results from DS2V.

2.3.4   Coaxial Cylinders

To test the line-of-sight algorithm, a second, smaller, cylinder was inserted coaxially into the cylinder described above with $R_2 = R/4$. The smaller cylinder was made to

be completely adsorbing ($\sigma = 1$). The results from this case are shown in Figure 2.9. As can be seen, the leaving flux from the outer cylinder is slightly underestimated in this case due to some error in FMFlux in calculating the visible areas of partially blocked faces. This is discussed in detail in Appendix B.

| (a) | (b) |
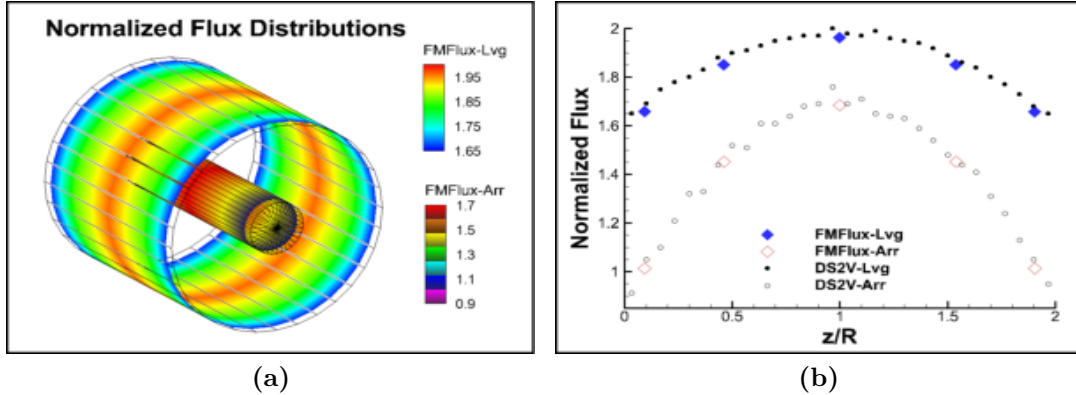
Figure 2.9: Results for the axisymmetric case of two coaxial cylinders, testing the line-of-sight routine. The outer cylinder outgasses internally with $\sigma = 0$, while the inner cylinder is completely adsorbing, $\sigma = 1$. (a) shows the full results from FMFlux while (b) compares a cross section of the results to results from DS2V. In both (a) and (b), the leaving flux is plotted for the outer cylinder and the arriving flux is plotted for the inner cylinder.

2.3.5 Enclosed Cylinder

The cylinder is also a good case to test one of the drawbacks of the method of angular coefficients. Define a ratio of enclosure, α, as the enclosed area over the open area such that for the cylinder in Figures 2.7 and 2.8 α is given by

$$\alpha = \frac{2\pi R Z}{2\pi R^2} = \frac{Z}{R} = 2. \tag{2.15}$$

If α is increased by capping the ends of the cylinder to some extent, then the method will require more iterations and more time to reach steady state. A few points to demonstrate this are displayed in Figure 2.10. In reality, if the cylinder were completely enclosed, the pressure inside would build and the outgassing would

decrease. However, this feature of pressure dependent outgassing is not included in FMFlux, so a steady state will never be reached for completely enclosed geometries.

(a) $\alpha = 7$ (b) $\alpha = 50$ (c) $\alpha = 95$

(d)
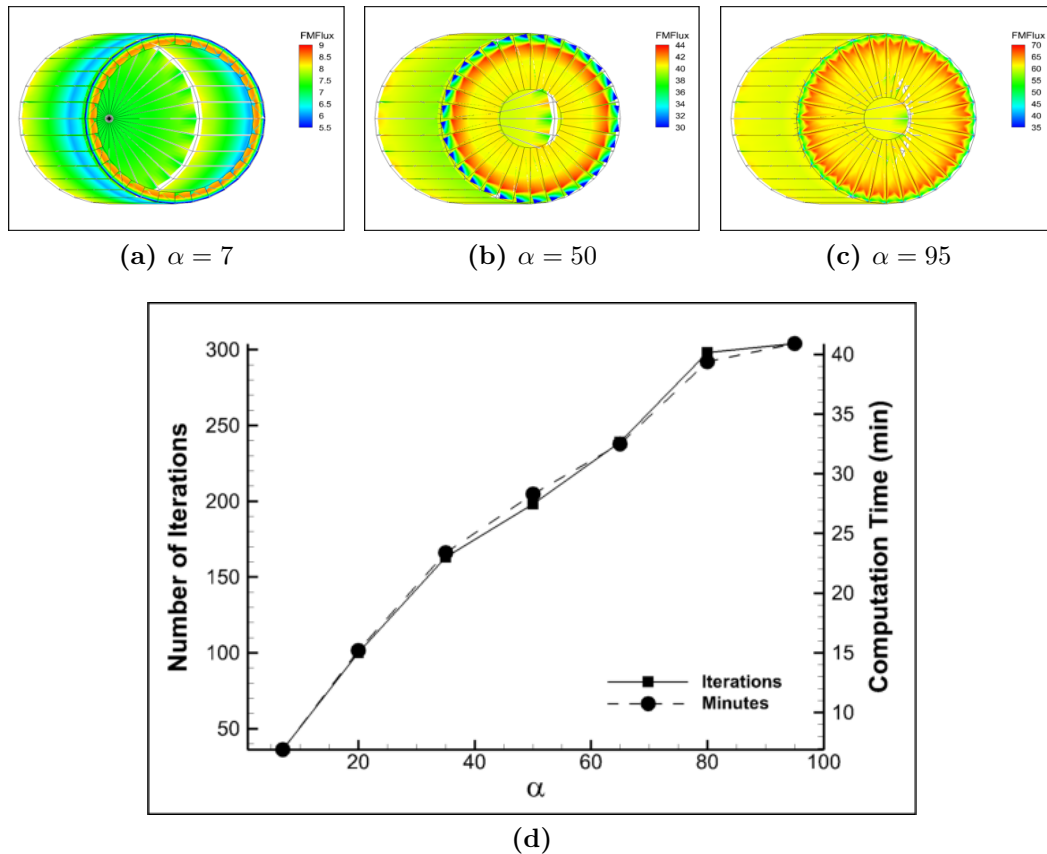
Figure 2.10: Display of the number of iterations required to reach steady state versus the amount of enclosure for a cylinder. The results shown are for $\epsilon = 10^{-4}$ using 5 nodes per face per dimension. Each case shown has the same number of faces. The time points were taken on a standard desktop pc.

2.3.6   Strip Source

A three dimensional situation that has an analytical solution is given by Holland and Steckelmacher (1952). This case consists of a strip source, a long, skinny plane of length L and width much smaller than L, depositing onto a parallel plane a distance h away (see Figure 2.11). The expression given for the thickness of a film being grown

Approved for public release; distribution is unlimited.

on the receiving plane, Equation 18 in that paper, is

$$d = \frac{mh^2}{2\pi\rho La^3} \left(\frac{aL\left(a^2 - x^2 + \frac{L^2}{4}\right)}{(a^2 + x^2)^2 + \frac{L^2}{2}(a^2 - x^2) + \frac{L^4}{16}} + \tan^{-1}\left(\frac{aL}{a^2 + x^2 - \frac{L^2}{4}}\right) \right), \quad (2.16)$$

where ρ is the density of the film being deposited, m is the total mass deposited, and $a^2 = h^2 + y^2$. Normalizing Equation 2.16 to the thickness at the origin ($x = y = 0$) gives the thickness profile of the film grown. The results from FMFlux are compared to this analytical expression in Figure 2.12 showing excellent agreement.
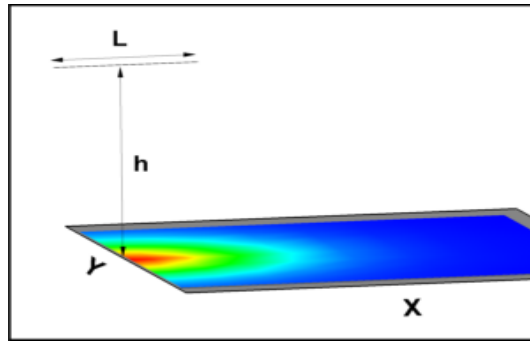
Figure 2.11: A strip source depositing onto a parallel receiving plane.

(a) (b)
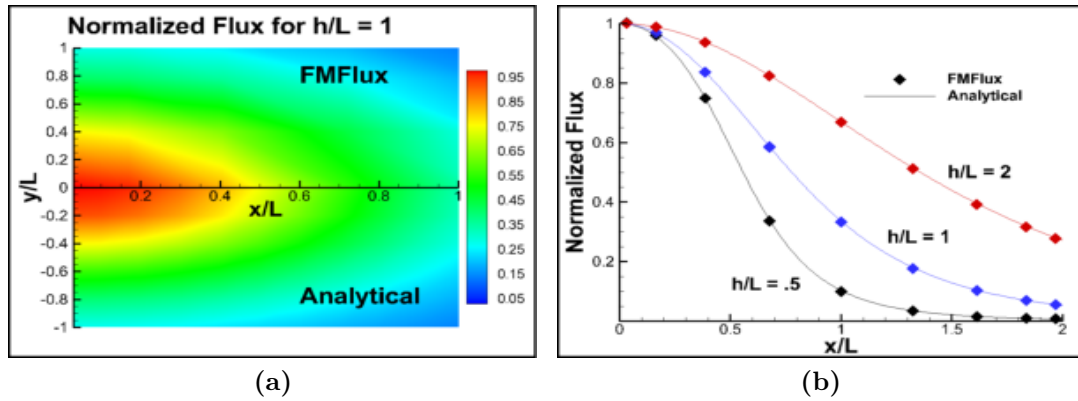
Figure 2.12: Results for the 3D case of a strip source, these values are normalized to the value at the origin. The source has $\sigma = 0$, while the receiving plane has $\sigma = 1$. (a) compares the full results from FMFlux (top) to Equation 2.16 (bottom) for $h/L = 1$. (b) shows the results along the x-axis for a few different values of h/L.

39

2.4 Flux Distributions in the 10V Space Chamber

To demonstrate the applicability of FMFlux to the space chambers, a simple model of the 10V chamber was made in Blender. The model is intentionally low-polygon to keep computation times down, but is approximately to scale. The model consists of four main components, the outer walls, the SUT antechamber, the cryoliner, and a fictitious projection plane that was placed in the chamber. Rather than attempting to model all of the chamber components (spectral sources, optics, drives, etc.) whose exact locations, dimensions, and orientations in the chamber are not available, the projection plane is placed in the center of the chamber to give an idea of the levels of flux along the axis of the chamber (see Figure 2.13). The primary suspects of normal amounts of residual gas in the 10V chamber are outgassing from the room temperature external walls and outgassing from the SUT itself. The actual magnitude of outgassing from the chamber walls and, especially, the sensor under test are quantities that must be experimentally determined, which is an ability that is currently being developed for the 10V chamber. For this demonstration three cases have been considered. The first case is uniform outgassing from the chamber walls only. The second case considers outgassing from the walls and a test sensor (modeled as a simple cylinder) where the outgassing for both is at the same rate. In the third case, the outgassing rate of the SUT is set to be an order of magnitude greater than that of the chamber walls. The results from the first case are shown in Figures 2.14 and 2.15. The results from the second case are shown in Figures 2.16 and 2.17, and the third case results are shown in Figures 2.18 and 2.19. The figures with dimensions shown are normalized to the overall length and radius of the external walls L and R.

40
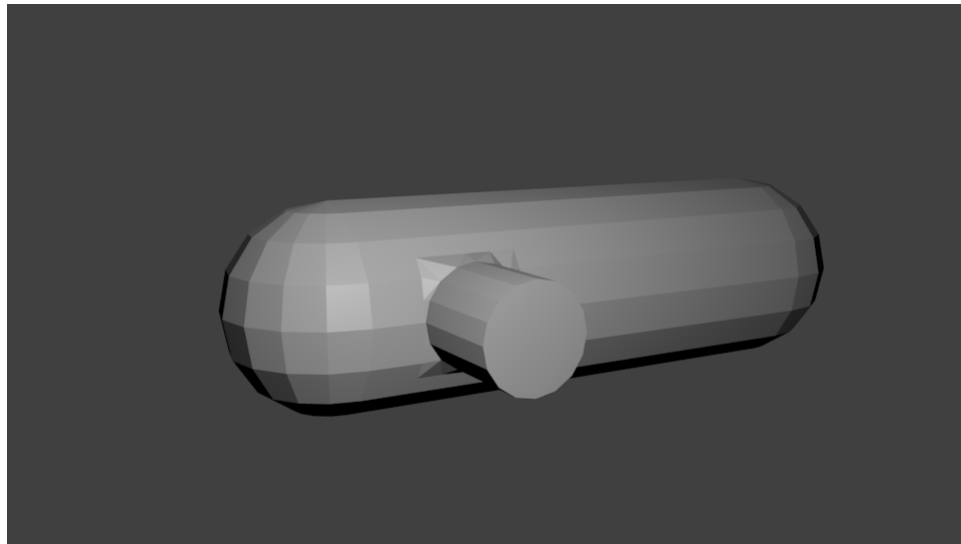
(a)
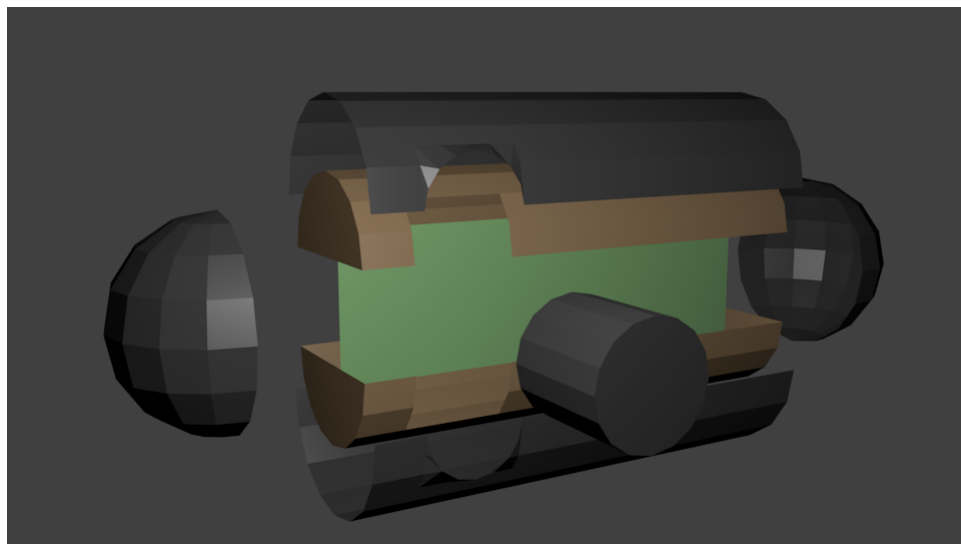
(b)

Figure 2.13: Rendered images of the 10V model in Blender. (a) is the external walls and the SUT antechamber, (b) is an exploded view where the colors have been changed for clarity. The external walls and SUT antechamber are black, the cryoliner is brown, and the projection plane is green.
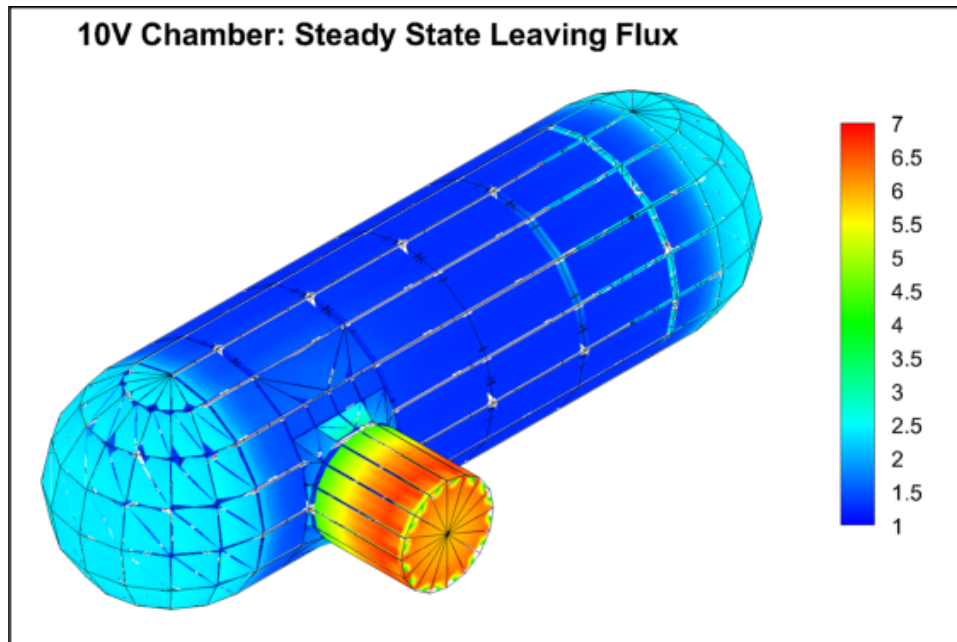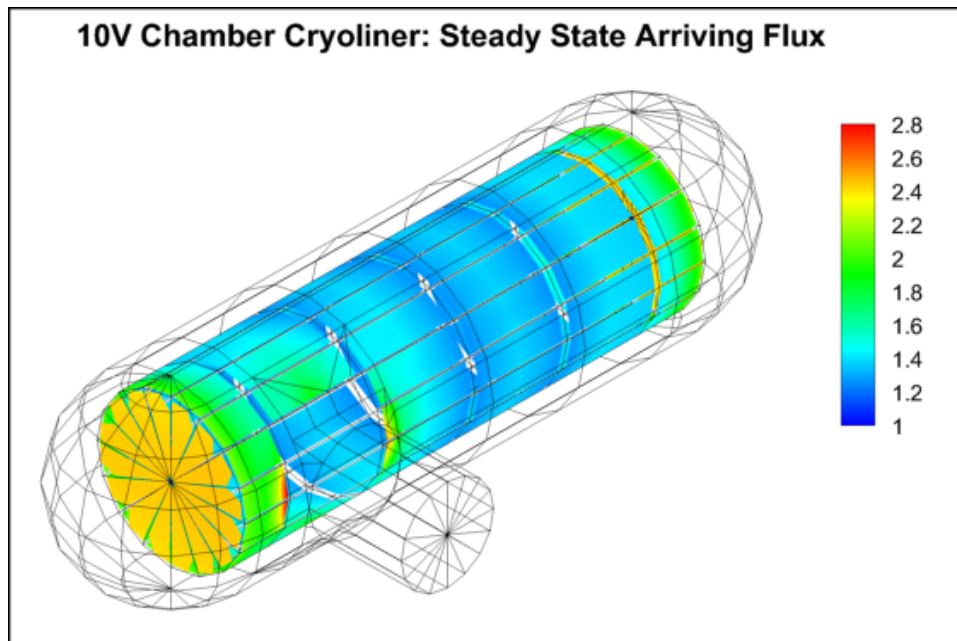
Figure 2.14: Results from FMFlux for the 10V model assuming uniform outgassing from the chamber walls. (a) shows the leaving flux from the external walls and SUT antechamber and (b) shows the arriving flux on the cryoliner.
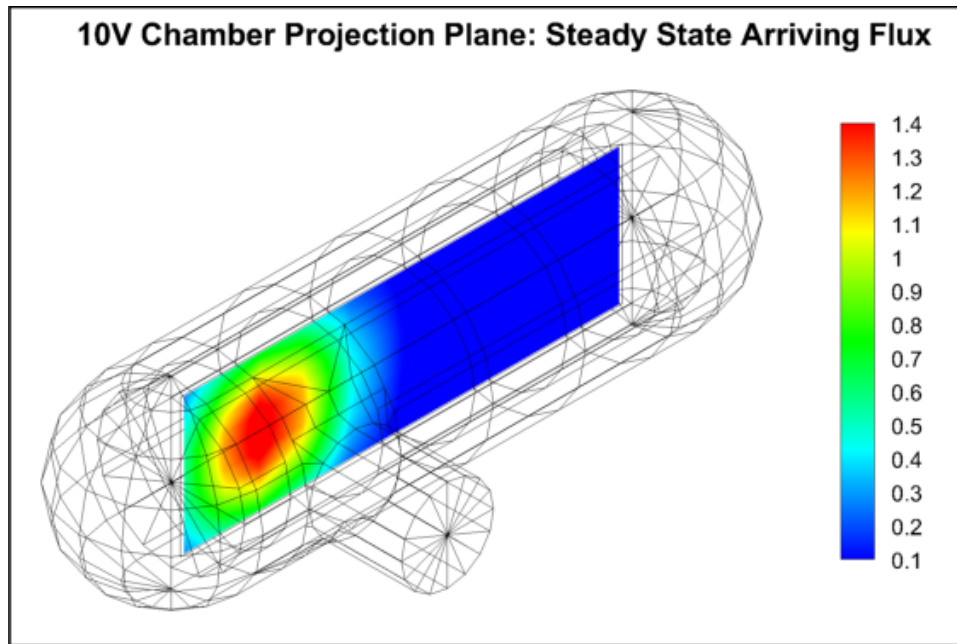
(a)
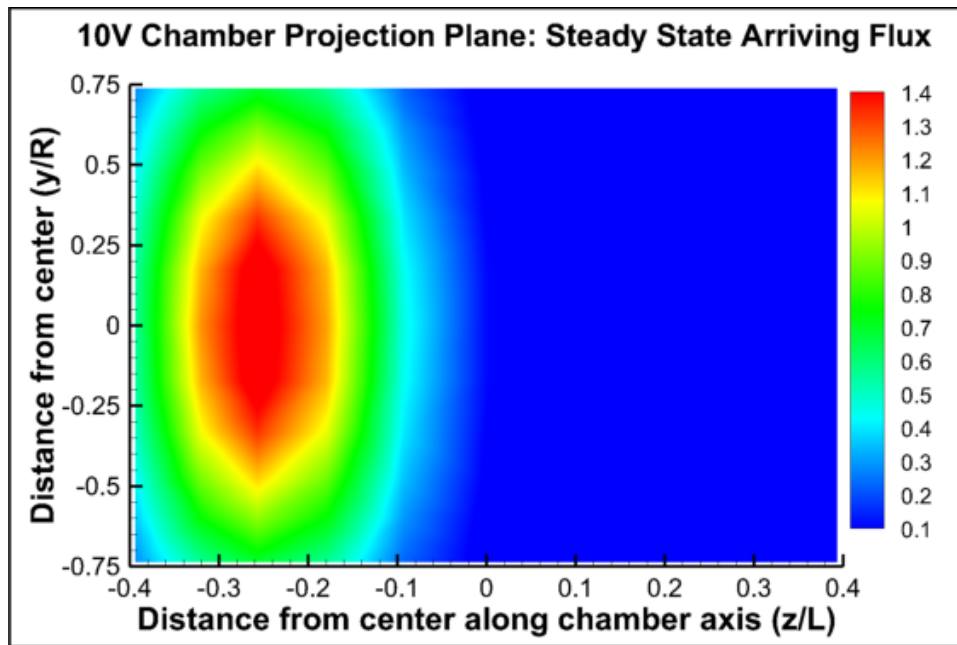
(b)

Figure 2.15: The arriving flux on the projection plane for the 10V model assuming uniform outgassing from the chamber walls.
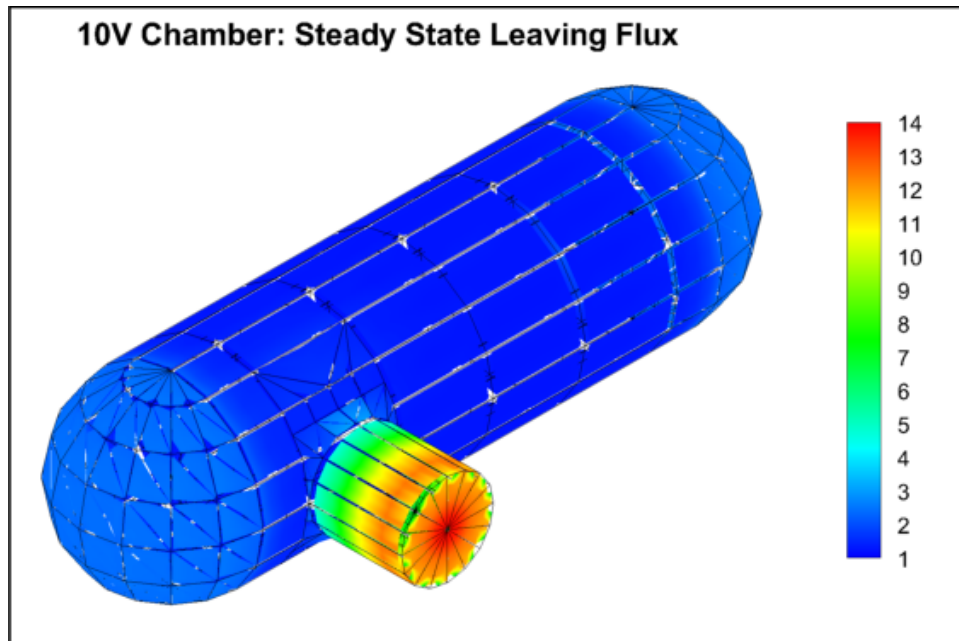
(a)
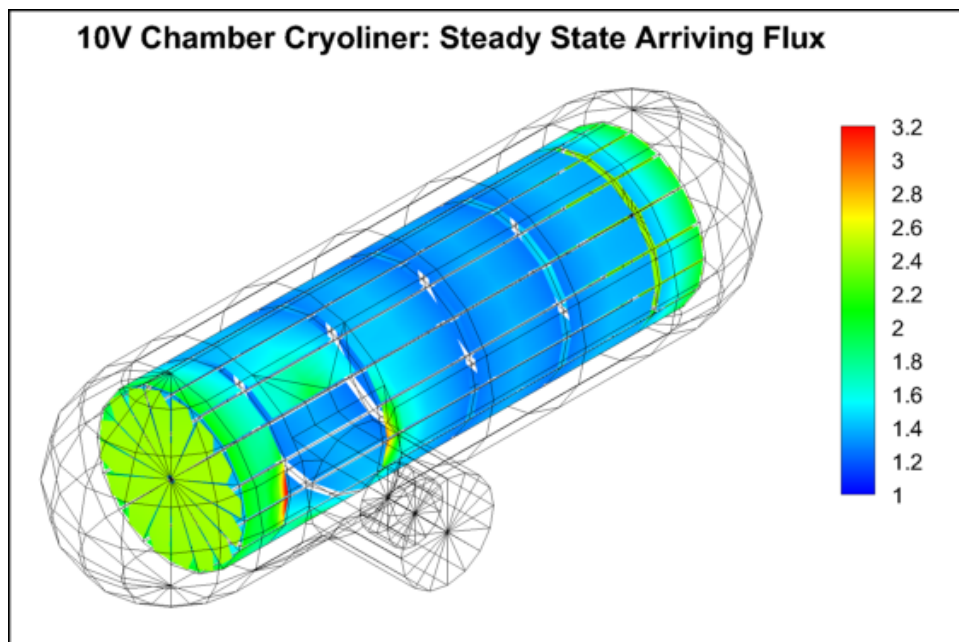
(b)

Figure 2.16: Results from FMFlux for the 10V model assuming uniform outgassing from the chamber walls and a sensor outgassing at the same rate. (a) shows the leaving flux from the external walls and SUT antechamber and (b) shows the arriving flux on the cryoliner.
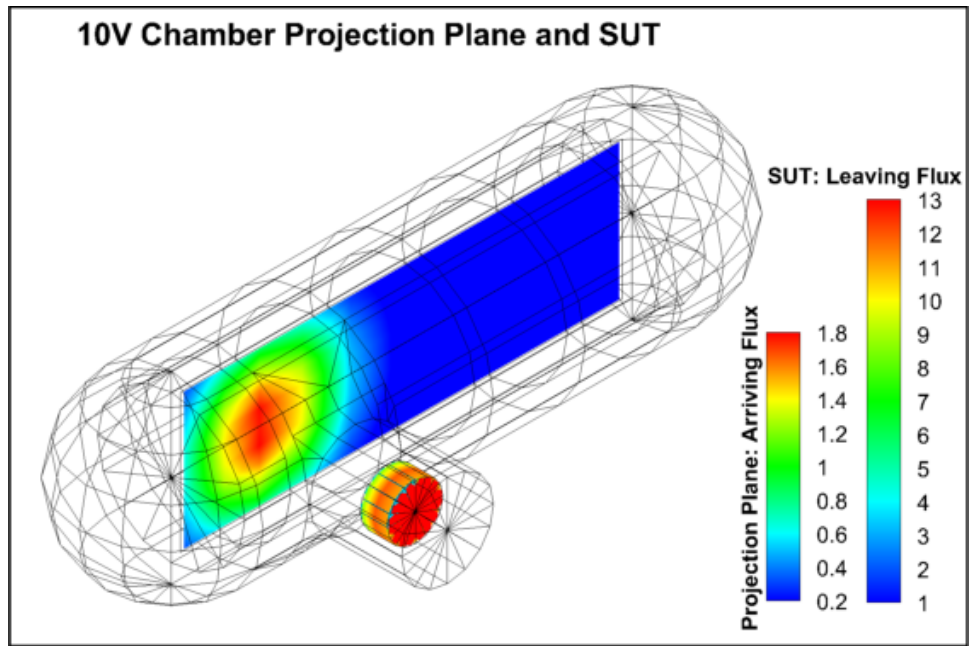
(a)
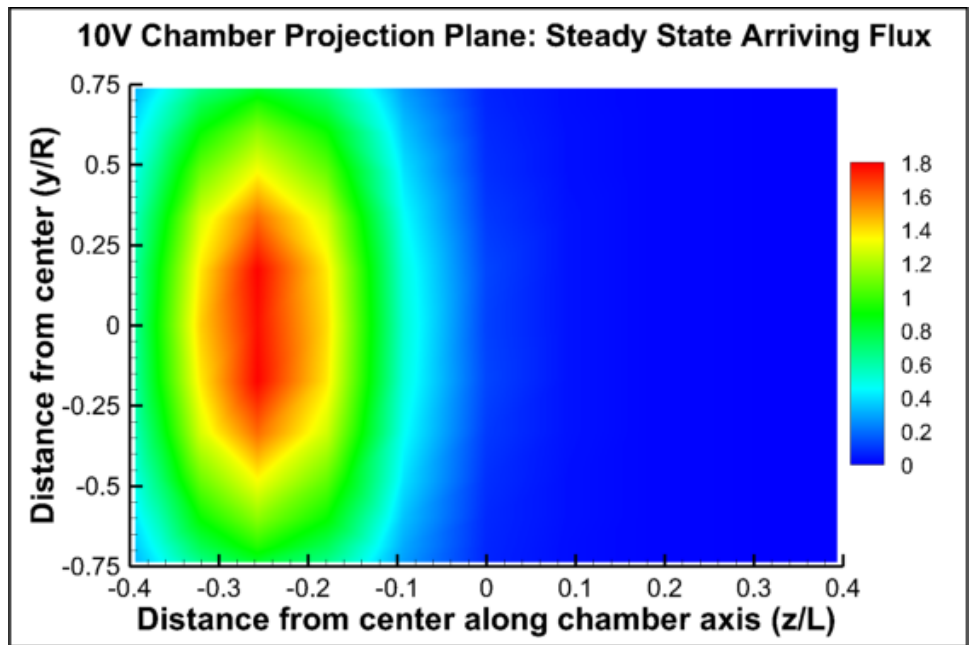
(b)

Figure 2.17: Results from FMFlux for the sensor-under-test and projection plane. (a) shows the leaving flux for the SUT and the arriving flux on the projection plane.
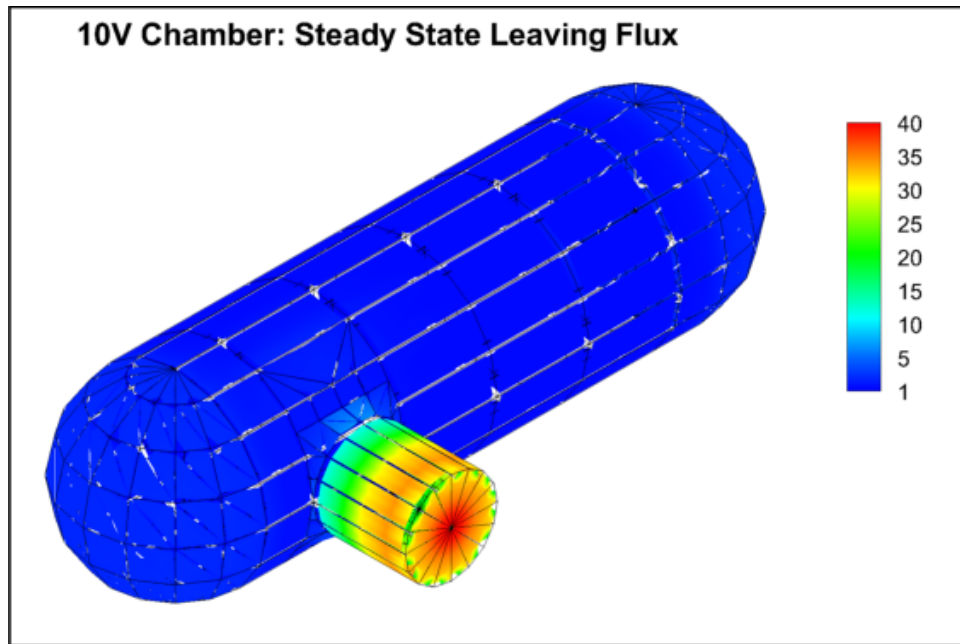
(a)
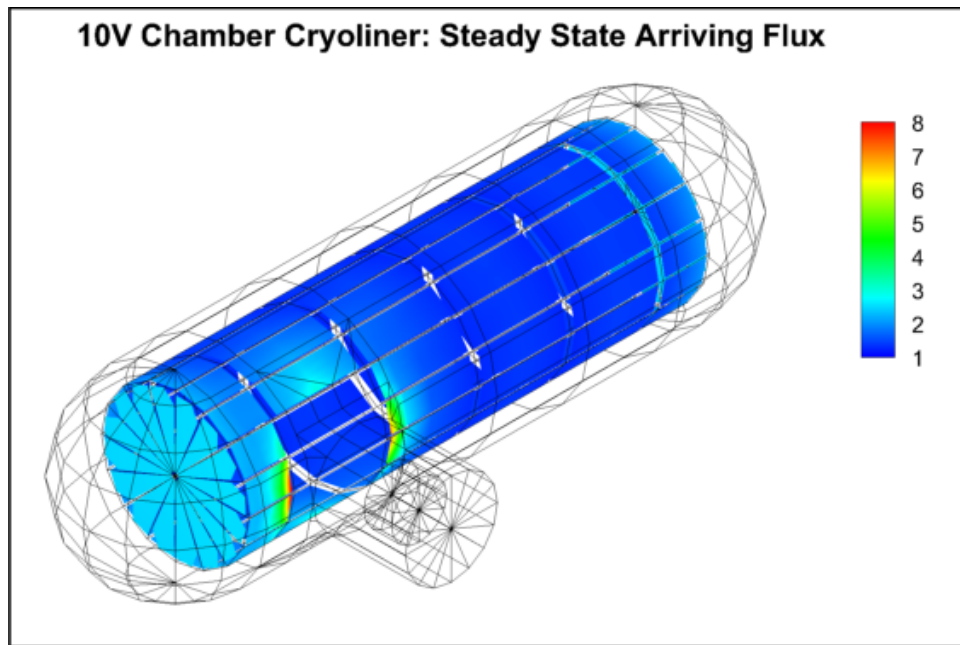
(b)

Figure 2.18: Results from FMFlux for the 10V model with uniform outgassing from the walls and the SUT outgassing at 10 times the rate of the walls.
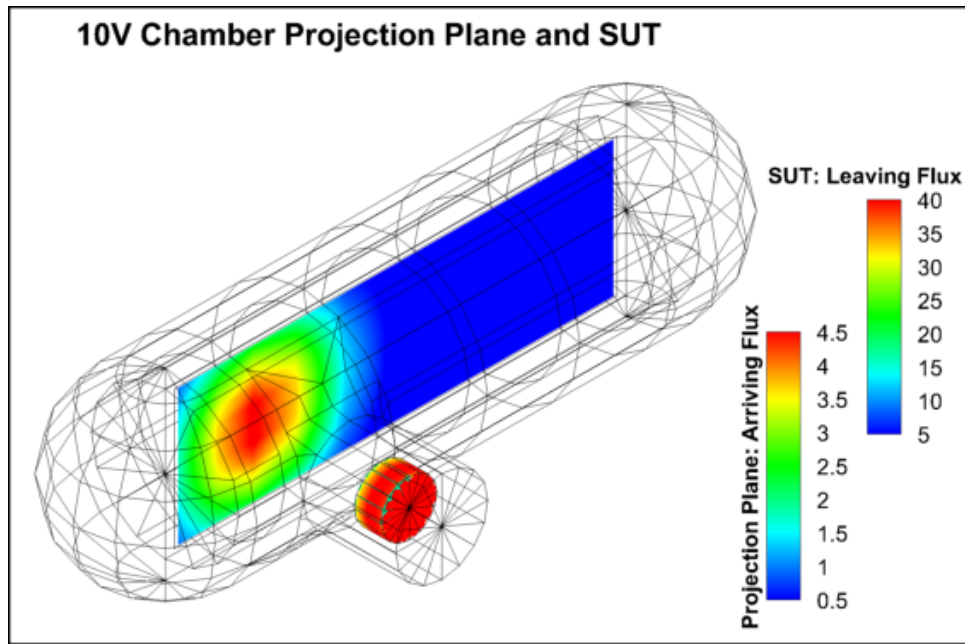
(a)
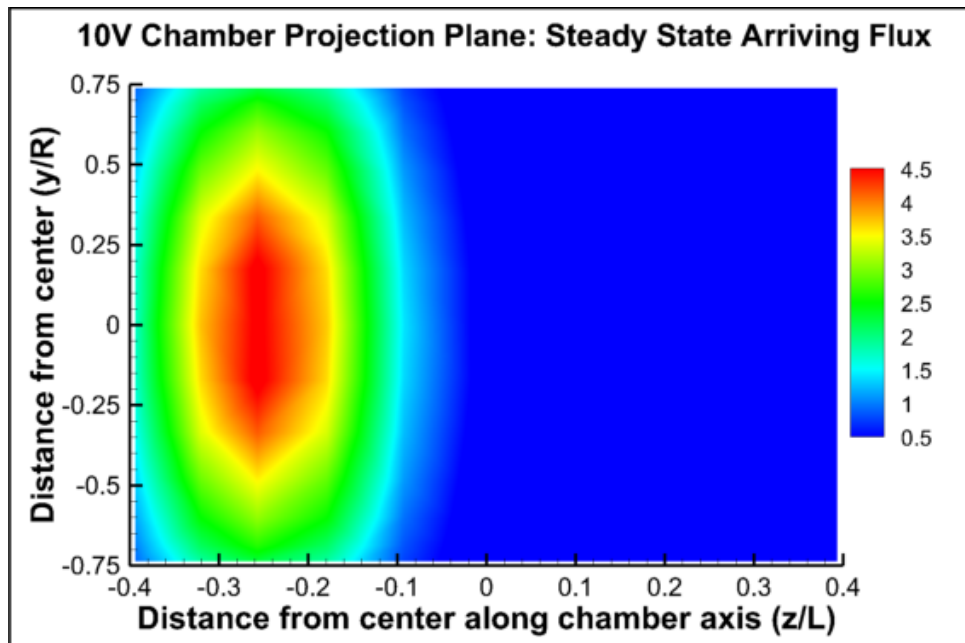
(b)

Figure 2.19: Results from FMFlux for the projection plane of the 10V model with uniform outgassing from the walls and the SUT outgassing at 10 times the rate of the walls.

47

Growth rates of a film can be found by dividing the arriving flux density by the density of the film. Using a ballpark literature value of $10^{-11}(\frac{g}{cm^2 s})$ (Blears et al. (1960)) for the magnitude of outgassing of water from room temperature aluminum, the growth rates on the projection plane from the three cases is given in Figure 2.20 where the nominal density of LDA (0.94 g/cm^3) has been used.

(a)

(b)

(c)
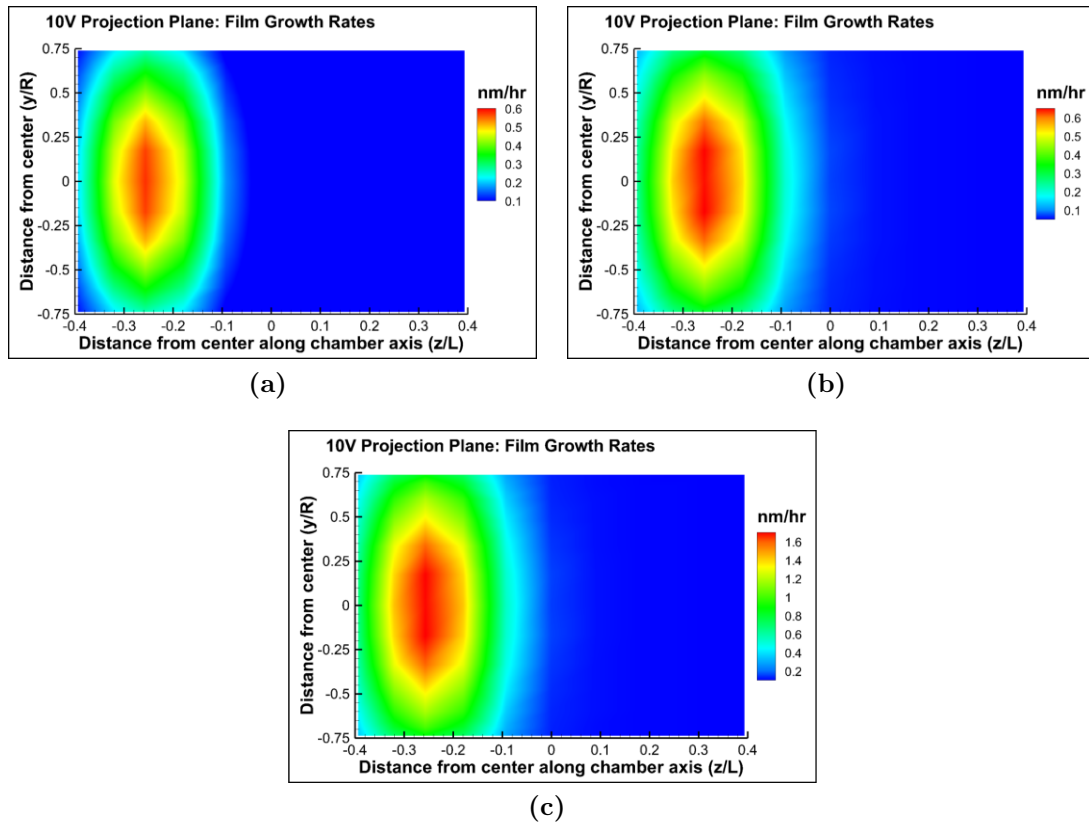
Figure 2.20: Growth rates on the projection plane for (a) only outgassing from the walls, (b) outgassing from the walls and sensor at the same rate, and (c) outgassing from the walls and sensor with the sensor outgassing at $10\times$ the rate of the walls. The outgassing rate for the walls is set to $10^{-11}\frac{g}{cm^2 s}$ and a film density of 0.94 g/cm^3 was used.

Chapter 3

Characterization of Optical Components with Contaminant Films

From an optical standpoint, cryodeposited contaminant films can be treated as any other thin film provided little radiation is lost to scattering (Wood and Smith (1978)). The methods of thin film analysis are well known and a good description is given in most optical text books (e.g. Born and Wolf (1964)). The complex refractive index is a function of temperature as well as wavelength. In wavelength regions where absorption is negligible, fitting models such as Sellmeier's or Cauchy's equations can be used to adequately describe the temperature and wavelength dependence (e.g. see Hawkins (1998)). In regions of resonance, where absorption is large, no such fitting models can be used. Rather, the refractive index and extinction coefficients are simply tabulated in these regions. Each thin film deposited on a substrate is described by a

transfer matrix as

$$M_j = \begin{pmatrix} \cos \delta_j & \frac{i}{p_j} \sin \delta_j \\ ip_j \sin \delta_j & \cos \delta_j \end{pmatrix}, \tag{3.1}$$

$$\delta_j = \frac{2\pi n_j d_j}{\lambda} \cos \theta_j,$$

$$p_j = \sqrt{\frac{\epsilon_j}{\mu_j}} \cos \theta_j, \quad \text{for } s \text{ polarization}$$

$$p_j = \sqrt{\frac{\mu_j}{\epsilon_j}} \cos \theta_j, \quad \text{for } p \text{ polarization}$$

where ϵ_j and μ_j are the dielectric constant and magnetic permeability of the jth film respectively (Born and Wolf (1964)). The characteristic matrix of a stack of films is then given by the matrix product from the outermost film to the innermost, i.e., if there are N films on a substrate the characteristic matrix is given by

$$M_{tot} = \prod_{j=0}^{N} M_j, \tag{3.2}$$

where M_0 is the matrix for the outermost film and M_N is the innermost film. The reflection and transmission coefficients are then

$$r = \frac{(m_{11} + m_{12}p_{sub}) p_{inc} - (m_{21} + m_{22}p_{sub})}{(m_{11} + m_{12}p_{sub}) p_{inc} + (m_{21} + m_{22}p_{sub})}, \tag{3.3}$$

$$t = \frac{2p_{inc}}{(m_{11} + m_{12}p_{sub}) p_{inc} + (m_{21} + m_{22}p_{sub})}, \tag{3.4}$$

where the $m'_{ij}s$ are the elements of M_{tot}, and p_{inc} and p_{sub} refer to the incident material (usually vacuum or air) and the substrate material respectively. The reflection and

transmission are found through

$$R = |r|^2, \quad \text{and} \quad T = \frac{p_{sub}}{p_{inc}} |t|^2, \tag{3.5}$$

and absorption is given by $A = 1 - R - T$.

Unfortunately, many of the optics in the space chambers are commercially manufactured and the prescriptions for them are proprietary. However, there are two components whose prescriptions were custom ordered, (and hence known), whose spectra can be calculated. The two components are beam combiners (called BC1 and BC7). There is also a BC5 that has an identical prescription to BC1. Additionally, common elements such as uncoated mirrors and windows can be calculated. A program utilizing the matrix method for thin film analysis was written for previous work (Labello (2007)). This program was used along with the open-source software OpenFilters (Larouche and Martinu (2008)) to calculate the spectra of a gold mirror (Figure 3.1), germanium window (Figure 3.3), and the two known components (Figures 3.5 and 3.6) with various amounts of contamination. The optical constants were obtained from the references noted in Section 1.3. For comparison the gold mirror and germanium window are also shown with one micron films of other common gases in Figures 3.2 and 3.4.
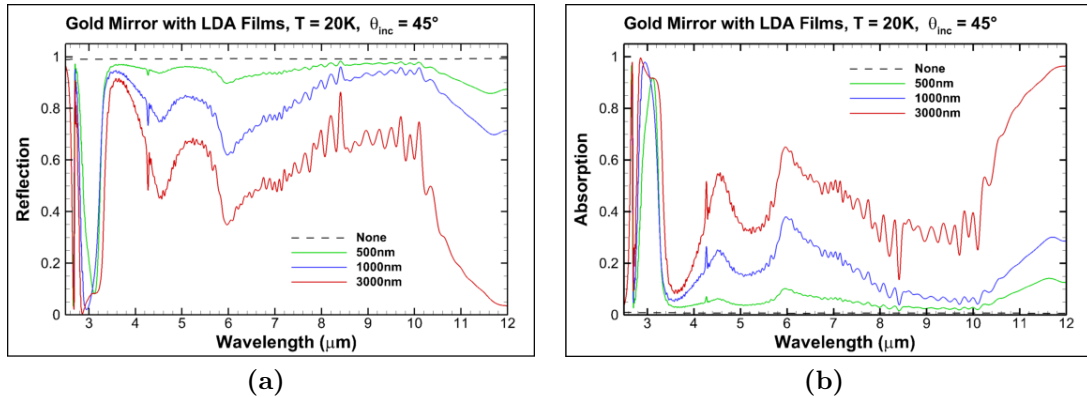
Figure 3.1: Reflection (a) and absorption (b) of a gold mirror with various amounts of LDA ice on it.

Approved for public release; distribution is unlimited.
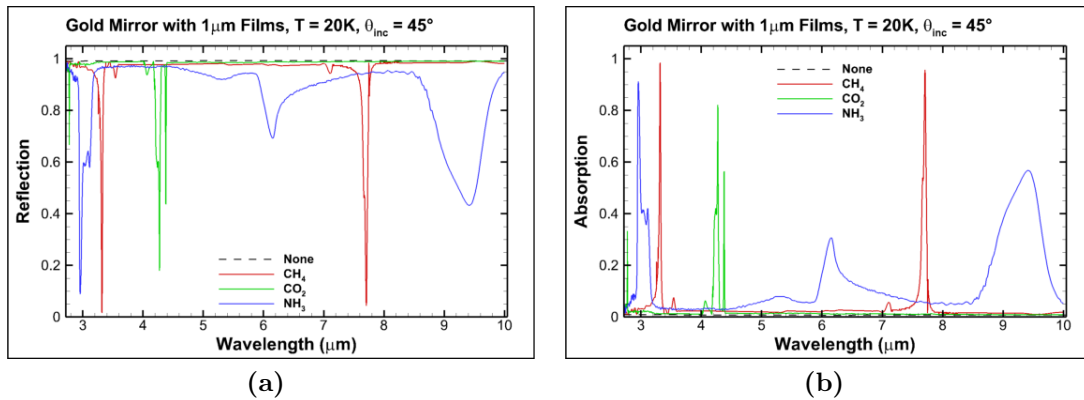
Figure 3.2: Reflection (a) and absorption (b) of a gold mirror with one micron films of methane, carbon dioxide, and ammonia ice on it.
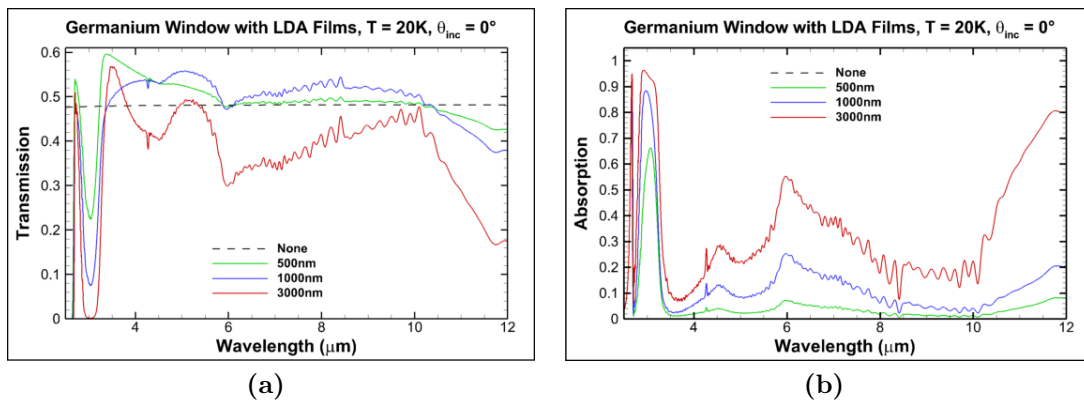
Figure 3.3: Transmission (a) and absorption (b) of a germanium window with various amounts of LDA ice on it.
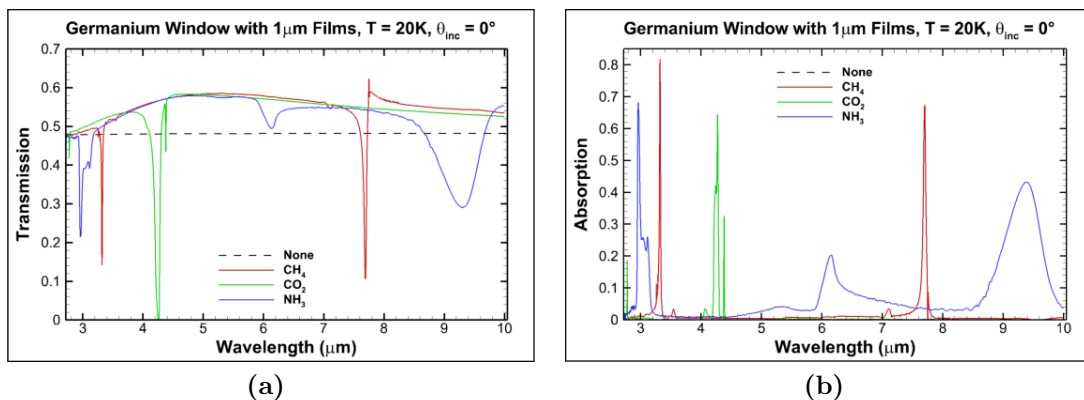
Figure 3.4: Transmission (a) and absorption (b) of a germanium window with one micron films of methane, carbon dioxide, and ammonia ice on it.
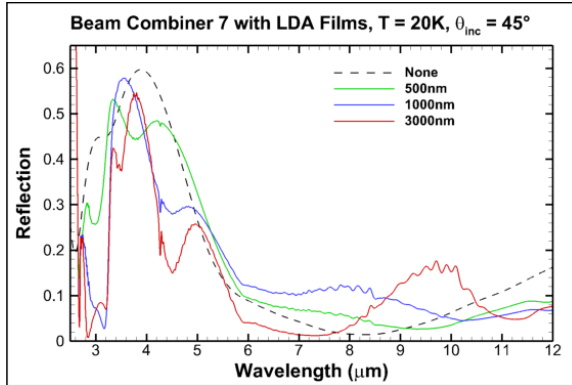
(a)
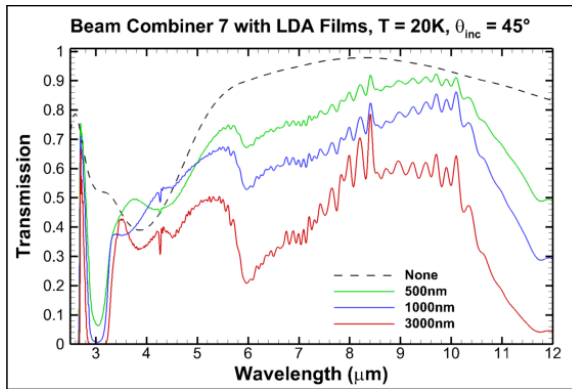
(b)
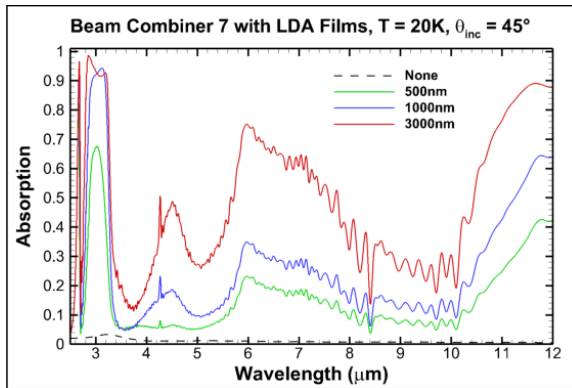
(c)

Figure 3.5: Reflection (a), transmission (b), and absorption (c) of BC7 with various amounts of LDA ice on it. The film thicknesses listed are per side.
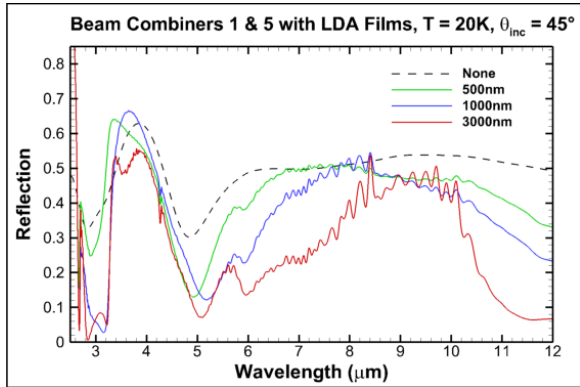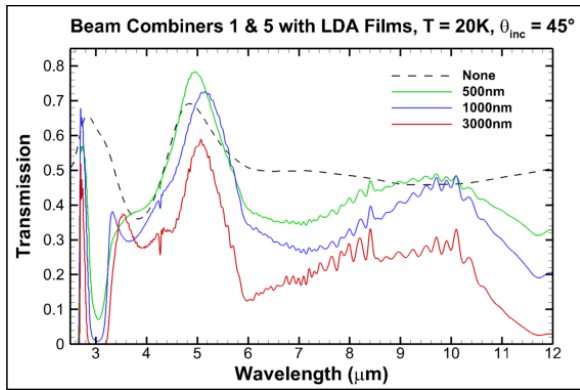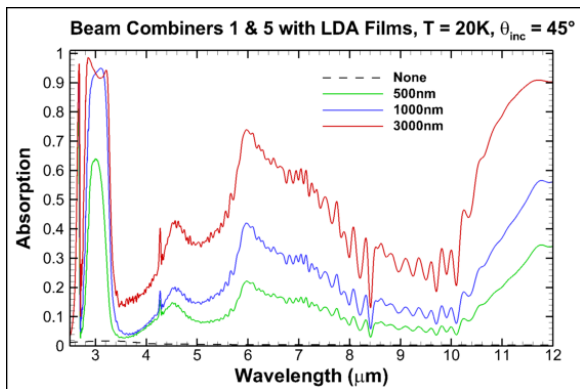
Figure 3.6: Reflection (a), transmission (b), and absorption (c) of BC1 and BC5 (they have identical prescriptions) with various amounts of LDA ice. The film thicknesses listed are per side.

Approved for public release; distribution is unlimited.

There is a throughput model of the 10V chamber that contains the measured optical spectra of the components in the chamber. The model begins with the irradiance of a source in the chamber and then multiplies the transmission or reflection spectrum of each component along the radiation's path to a detector. The end result of the model is the integrated throughput over certain wavelength bands. The model uses optical spectra of components that were measured at room temperature. These spectra can be adjusted to reflect shifts due to temperature or contamination (see (Labello (2007))). The result of adjusting the model to reflect beam combiners that are contaminated with water ice films is shown in Figure 3.7

(a)   (b)
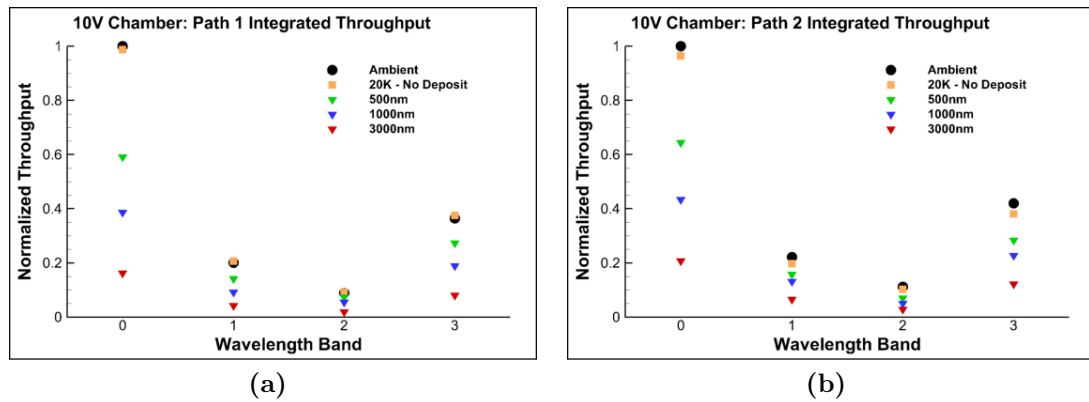
Figure 3.7: The effect of beam combiners contaminated with LDA films on the throughput of 10V. Wavelength band 0 is the total wavelength region integrated. The other bands are sub-bands within band 0. Path 1 (a) and Path 2 (b) are similar paths with the only difference being the transmission (path 1) or reflection (path 2) of BC1.

Chapter 4

Setup of an Experiment to Detect and Study Thin Films of Ice

One of the challenges that needs to be overcome in order to grow ice films in a controlled fashion under cryovacuum conditions is introducing pure water vapor into the vacuum chamber. A convenient method is to use a desiccant. A desiccant is a material that absorbs, or adsorbs, water molecules from the atmosphere. Upon heating or de-pressurization of the desiccant, the water molecules are released. In chambers where most surfaces are at room temperature and there is only a cold finger for deposition, background deposition can be used by simply allowing the vapor into the chamber. In cryogenic vacuum chambers with large cold surface areas the vapor must be directed toward the deposition substrate. This can be accomplished with a capillary array, which produces a molecular beam, or an effusion (or Knudsen) cell which produces a cosine distribution provided the flow is free molecular in the cell. An experiment to detect and study thin films of ice is being developed at AEDC and UTSI. There have been two tests of this experiment to date in the cryogenic ultra high vacuum chamber (UHV chamber) at AEDC. The main purpose of this work is to develop a system capable of detecting and measuring contaminant films in the space chambers. Simultaneously it offers the opportunity to measure the optical and

physical properties of these films. The setup of the initial test was chosen to be as simple as possible. A desiccant was placed inside an effusion cell and the effusion cell was directed toward a mirror and a quartz crystal microbalance (QCM). A QCM is a small microbalance that measures the mass deposition rate per unit area ($g\,cm^{-2}\,s^{-1}$). Briefly, a voltage is put across a quartz crystal that excites a vibration in the lattice that oscillates at a specific frequency (common QCM's operate at 6MHz) similar to the way a quartz wristwatch operates. The crystal is physically attached through a spring to a deposition surface of known area and mass. When a mass is deposited on the deposition surface the frequency of the crystal oscillation changes in a known manner, hence, allowing a measurement of the mass deposited. Growing a film on a mirror allows optical techniques to be used to measure the thickness growth rate of the film. By growing a film simultaneously on the mirror and QCM, the mass and thickness of the film are both known and, hence, the density of the film can be determined as $\rho = \frac{m q_{arr}}{\eta}$, where m is the molecular mass, q_{arr} is the deposition flux density ($cm^{-2}\,s^{-1}$) and η is the thickness growth rate.

4.1 First Test

The setup of the initial test of the experiment is shown in Figure 4.1. The effusion cell is a critical component of the experiment and was custom made to give a cosine distribution under free molecular flow (see Appendix C). The desiccant chosen for this test was calcium sulfate dihydrate ($CaSO_4 - 2H_2O$) more commonly known as gypsum which came in a powder form. The two water molecules per gypsum molecule allows for a good amount of water to be stored in a relatively small sample (20% water by mass) and the water can be released by heating. The temperature of the effusion cell was controlled with the use of thin film Minco heaters wrapped around it and a cryogenic linear temperature sensor (CLTS) connected to a Lakeshore 340 temperature controller. The mirror and QCM were individually temperature controlled in a similar fashion. The effusion cell was also connected to a baratron

through copper tubing so that the water vapor pressure could be monitored. Although not shown in the figure, a motorized shutter was placed in front of the effusion cell to start and stop deposition. Photographs taken during setup for the test are shown in Figure 4.2.
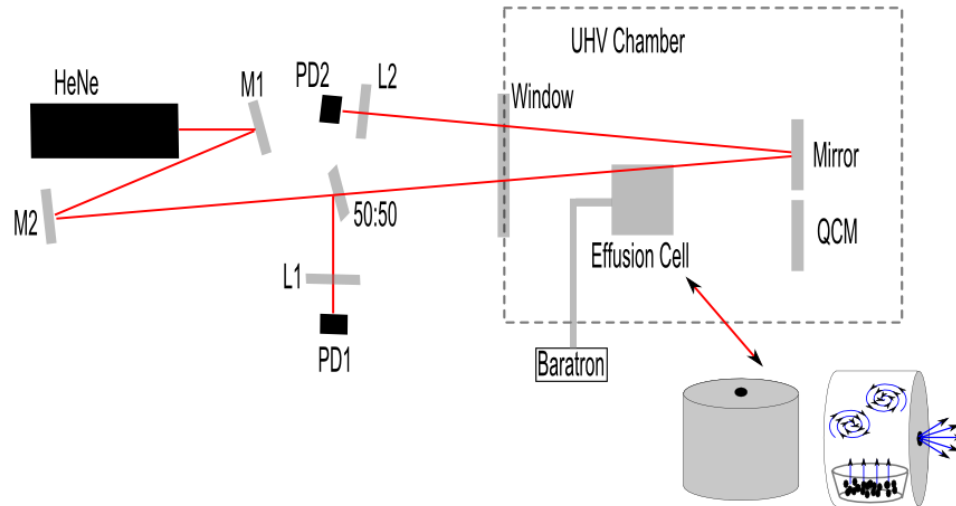
Figure 4.1: Schematic of the experimental setup for the initial test of the cryodeposit experiment.
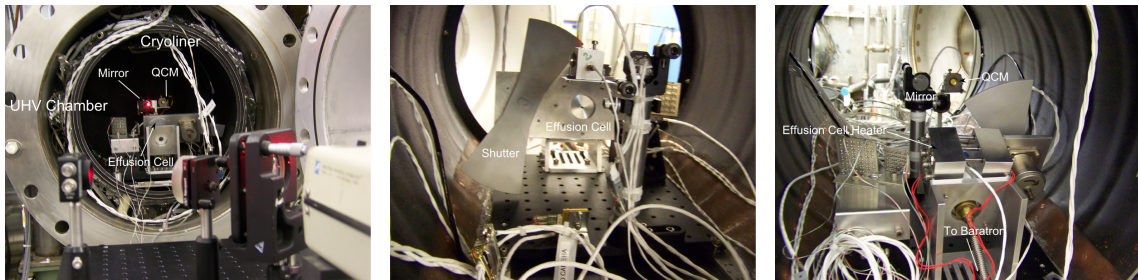
Figure 4.2: Images taken during setup for the initial test of the cryodeposit experiment.

Some data from the initial test is shown in Figure 4.3. There were clearly some problems. To begin the test, the effusion cell was heated to 373K. The pressure in the effusion cell was expected grow smoothly as the water was released from the desiccant. Rather, the baratron shows several pressure spikes. This is indicative of pockets of gas trapped within the desiccant being suddenly released. Upon opening the shutter (red arrow in the figure) the QCM shows a linear response which was expected for

constant deposition. The interferometer however displayed a sudden drop in signal and no obvious interference fringes were produced as deposition commenced. Upon examining the mirror, it was evident that the desiccant powder had escaped the effusion cell and was contaminating the mirror and QCM (see Figure 4.4). This was later confirmed by a SEM of the mirror after the test (Figure 4.5).
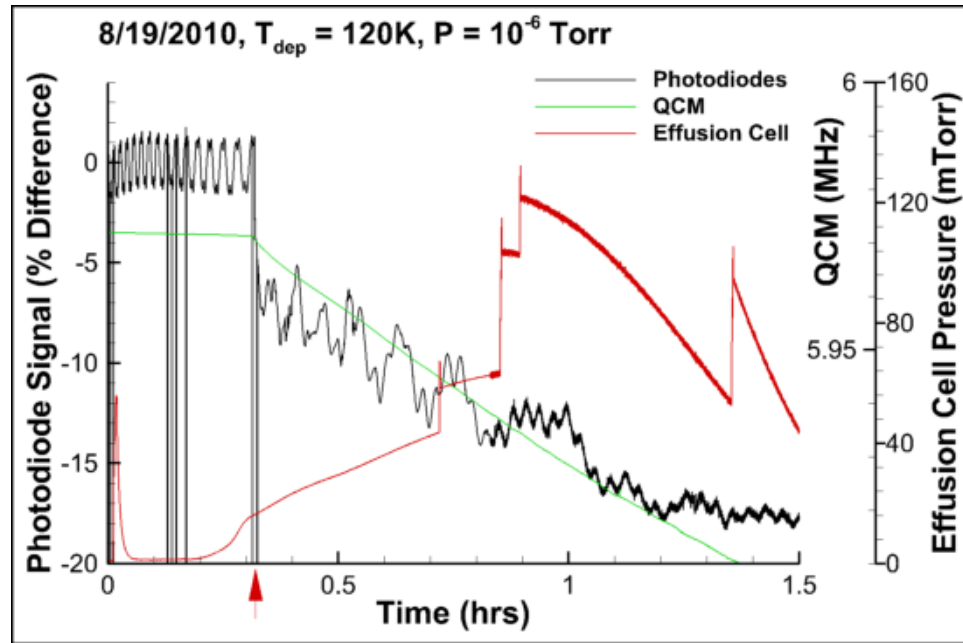
Figure 4.3: Data from the initial test of the cryodeposit experiment showing the photodiode readings, QCM frequency, and effusion cell pressure. The red arrow on the x-axis marks the opening of the shutter.

Although the desiccant was the biggest problem in the first test, there were others. Notably, the mirror and QCM temperature was measured to be 120K even though the UHV cryoliner temperature was under 20K. While 120K is sufficiently cold to grow amorphous ice films, it is not near the operating temperatures of the space chambers which is the desired temperature range to study the films. Also, one of the features desired to be studied in this experiment is the fracture of ice films. As amorphous ice films grow on a substrate stress builds in the films. Once the film becomes too thick, it fractures (Bahr (2001); Baragiola (2003); Pugh (2003); Westley et al. (1998); Wood and Smith (1978)). A film fracturing can damage the surface of an optical

59

(a)　　　　　　　　(b)　　　　　　　　(c)
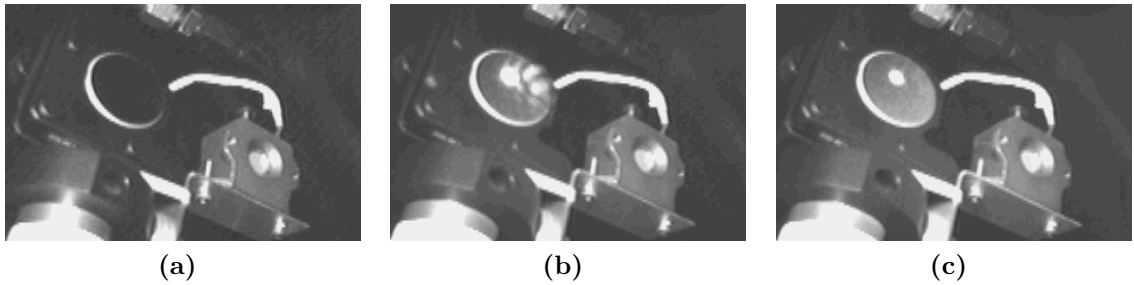
Figure 4.4: Images taken of the mirror and QCM during the first test. The image in (a) was taken shortly before the shutter was opened and deposition began. The laser was on at this time, but blocked from entering the chamber. The images in (b) and (c) were taken directly after opening the shutter and one hour after deposition began respectively. Note the appearance of powder on the mirror and disappearance of extraneous reflections as deposition continued.
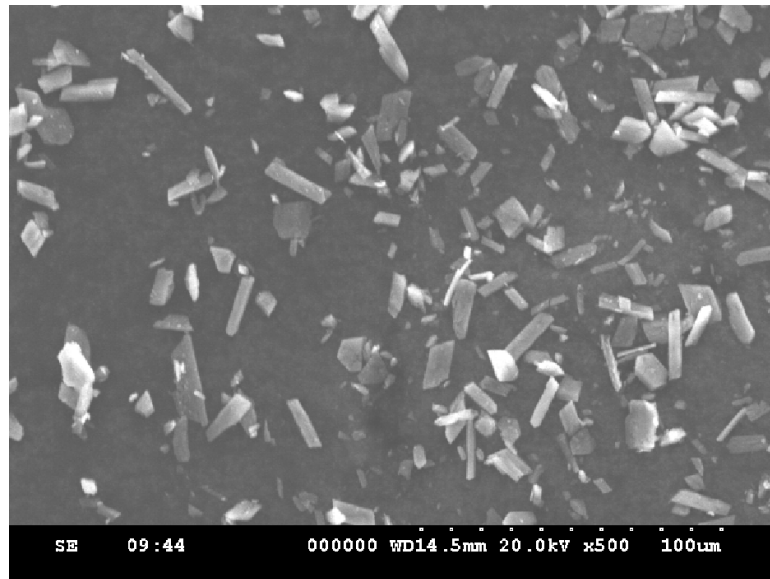
Figure 4.5: SEM of the mirror taken after the initial test. The SEM confirmed that the powder on the mirror was the calcium sulfate desiccant.

component and scatter radiation. There is very little quantitative information in the literature on this subject, but it is known that the critical thickness for fracture depends significantly on the temperature of the film. Figure 4.6 shows one of the very few quantitative measurements of the critical thickness for fracture in amorphous ice films. As can be seen by extrapolating the curve, getting to the critical thickness for fracture at 120K would require extremely thick films. Whereas at 20K there appears to be a minimum in the curve where the critical thickness for fracture is only 2-3μm. Note that the minimum seems to correlate to the phase change temperature where HDA forms instead of LDA.
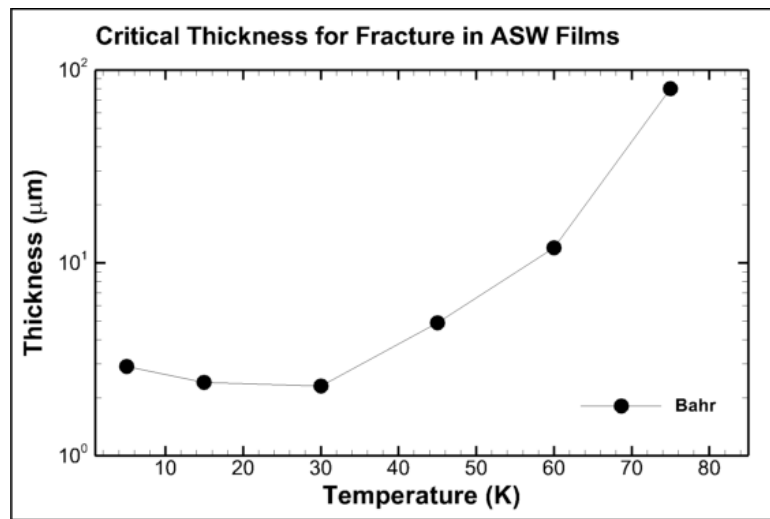
Figure 4.6: The critical thickness for fracture in amorphous solid water films. Data extracted from (Bahr (2001)).

4.2 Second Test

After the learning experience of the first test, several changes were made before the second test. A new type of granule form desiccant was chosen called zeolites. Zeolites are molecular sieves that trap molecules inside pores. These are often used in domestic and industrial applications for filtering or drying. Kitty litter is a common example of a zeolite. Selective filtering is achieved by choosing a zeolite with the correct pore

Approved for public release; distribution is unlimited.

size as the zeolites will only trap molecules whose diameter is less than the pore size (see Figure 4.7). Potassium and sodium anhydrate (KA and NaA) were the zeolites selected for further study as they have pore sizes just a bit larger than the diameter of the water molecule. A series of total mass loss experiments were conducted at UTSI to determine if these zeolites would be suitable for producing water vapor. The studies showed that almost 18% of the mass of the zeolites could eventually be released under vacuum without any heating applied and a residual gas analyzer (RGA) on the chamber showed that the great majority of the mass released was pure water along with trace amounts of other gases (Figure 4.8) (Rogers (2011)). Cobalt chloride ($CoCl_2-6H_2O$) was also studied due to it's exemplary water adsorption (over 40% water by weight). However, it displayed the same problem as calcium sulfate in escaping it's container in the vacuum chamber. Also, it is a rather hazardous material that requires special safety precautions. Images of the zeolites and cobalt chloride can be seen in Figure 4.9.
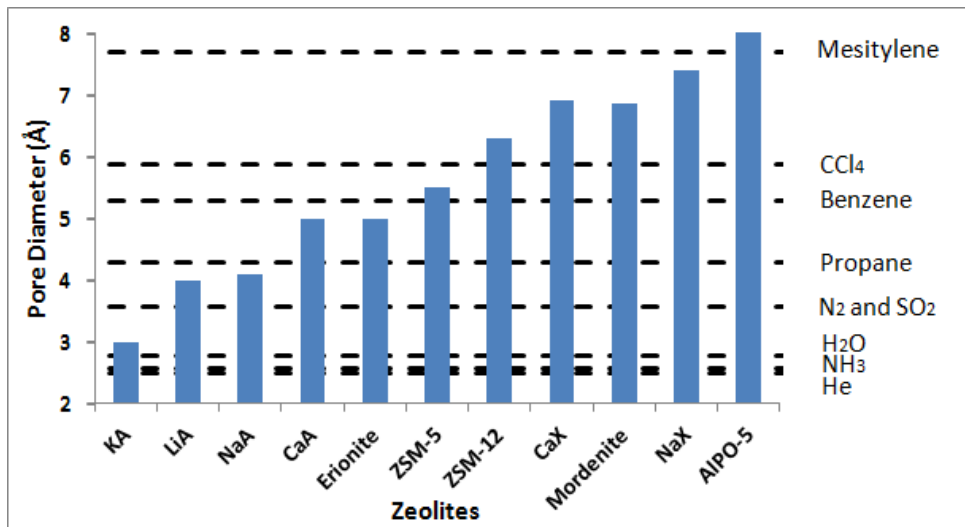
Figure 4.7: Common zeolites and their pore size with the kinetic diameter of some common molecules (Hagen (2006)).

In addition to changing the desiccant to the zeolites, an assembly to contain the zeolites outside of the main UHV chamber was also constructed. Moving the zeolites outside of the effusion cell further reduced the chance of any contamination

Approved for public release; distribution is unlimited.

(a)   (b)
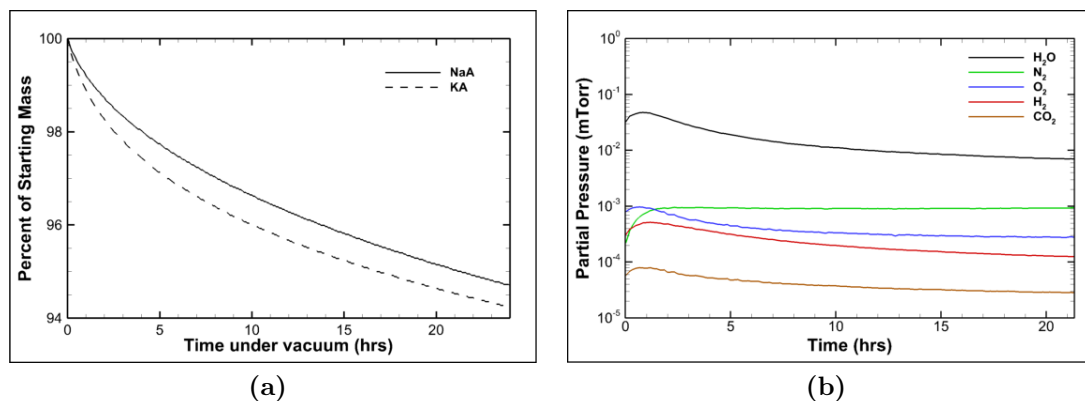
Figure 4.8: Example results from the total mass loss measurements made on the zeolites (a), and (b) the RGA readings (Rogers (2011)).

(a)   (b)
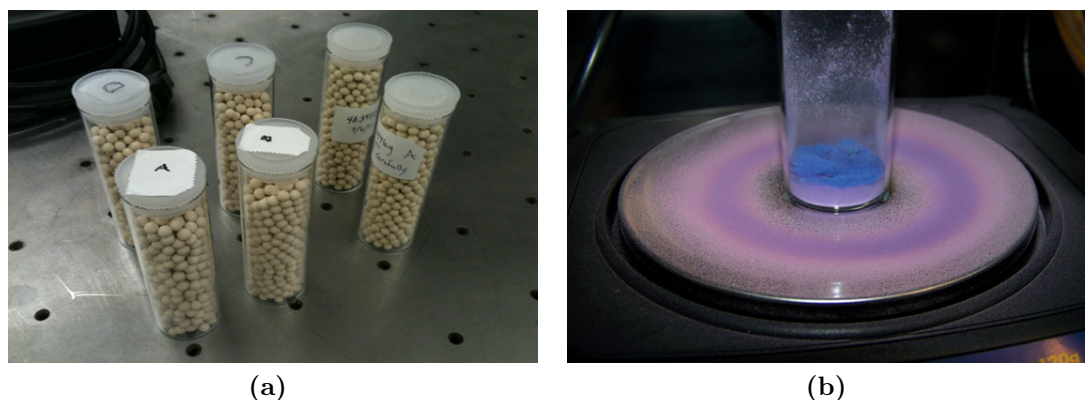
Figure 4.9: Images of (a) the KA and NaA zeolites and (b) cobalt chloride (Rogers (2011)). The cobalt chloride turns from purple to blue when it is dehydrated. Some of the cobalt chloride escaped the container and can be seen in the dish. This is the main reason the zeolites were selected over it for the second test.

63

getting onto the mirror and QCM. Also, the move allowed for the zeolite sample to be replenished during testing so that multiple data runs could be taken without having to warm or open the UHV chamber. The zeolite assembly was plumbed into the UHV chamber and to the effusion cell with large diameter (0.75") tubing to maximize the conductance of the feedthrough. The feedthrough was outfitted with heaters to make sure it did not get cold enough to freeze the water vapor before it could arrive in the effusion cell. The zeolite assembly was outfitted with a convectron gauge to measure pressure, and strip heaters were kept on hand to heat it in case faster growth rates were desired during the test. The zeolite assembly is shown in Figure 4.10.
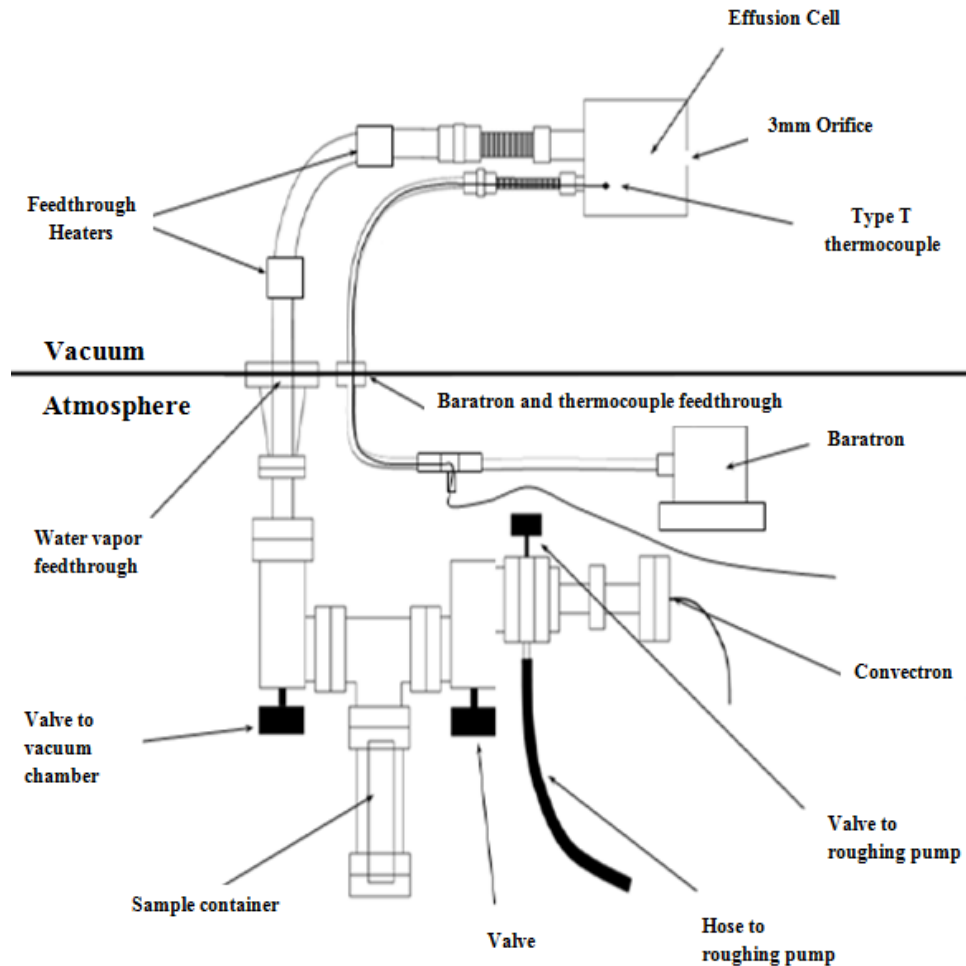
Figure 4.10: Schematic of the zeolite assembly for the second test of the cryodeposit experiment (reproduced with permission (Rogers (2011))).

To attempt to get the mirror and QCM to lower temperatures, a new solid aluminum mount was designed and built that accommodated both the mirror and QCM. Consolidating the two elements onto a single mount allowed them to be temperature controlled as a single unit rather than individually. The mount was outfitted with resistive heaters and temperature sensors. Additionally a large percentage of surface area on the mount was dedicated to cold straps (straps made of thermally conductive materials such as copper or aluminum) that could be attached to the mount on one side and directly to the cold bench or a GHe line on the other. Also, one of the suspected causes of the mirror and QCM staying so warm in the first test was radiation from the effusion cell. To address this, a radiation shield was made that could be mounted on the bench between the effusion cell and the mirror and QCM. Another significant change for the second test was the addition of two lenses into the optical system. These two lenses (one to expand the beam and one to focus it) allowed the laser to be focused on the mirror. No attempt to focus the laser on the mirror was made for the first test. The changes resulted in the experimental setup shown in Figures 4.11 and 4.12. Images of the setup are shown in Figure 4.13.
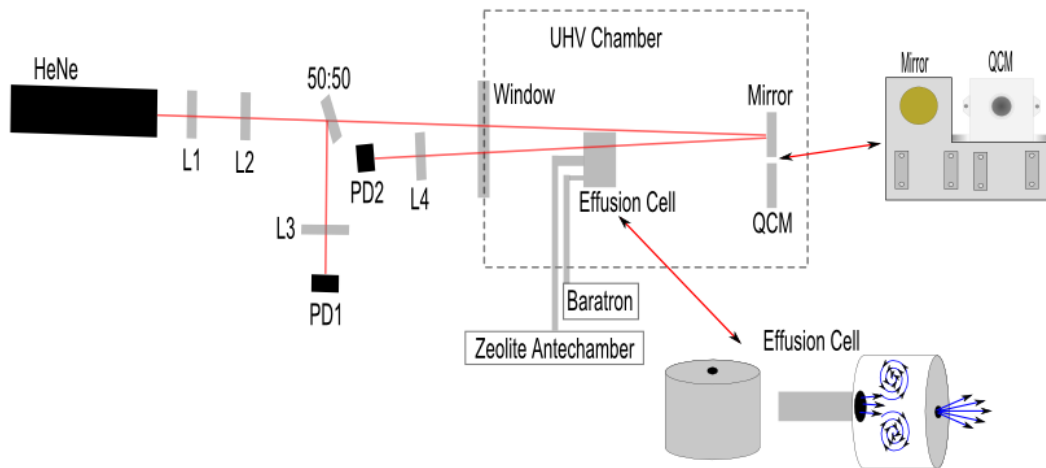
Figure 4.11: Schematic of the experimental setup for the second test of the cryodeposit experiment.

The new mount, radiation shield, and cold strap allowed the mirror and QCM to reach a temperature of 65K for the second test. While this is still not as low as the
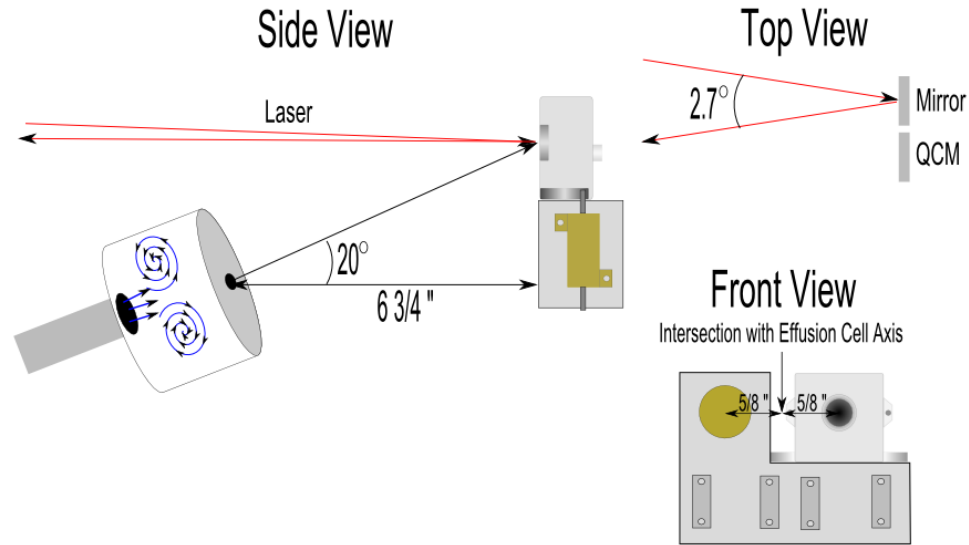
Figure 4.12: Details of the experimental setup for the second test.

$\approx 20K$ desired, it is significantly better than the first test. To begin the test, the zeolite antechamber was valved off from the main chamber and a hydrated zeolite sample was inserted. The antechamber was then pumped on by a roughing pump to evacuate the air. Once the roughing pump was disconnected, the antechamber pressure was monitored by a convectron gauge and was seen to rise and stabilize as the zeolite sample outgassed. Once the pressure had stabilized in the zeolite antechamber, the valve from the antechamber to the main chamber was opened. With the valve open, the pressure in the effusion cell was seen to rise quickly. Once the pressure had peaked in the effusion cell, the shutter in front of the effusion cell was opened to allow deposition to begin. Data from the first hour of the second test are shown in Figure 4.14. As can be seen in the figure, the second test was clearly more successful than the first test. The QCM showed the expected linear response and the photodiodes displayed clear interference fringes as deposition commenced. As the test continued, the zeolite sample eventually became dehydrated and deposition slowed down. As deposition slowed, the interference fringes spread out accordingly (see Figure 4.15).

Around 10 hours after deposition began, the QCM exhibited a very sudden increase in frequency. The sudden increase was followed by a short period of apparent
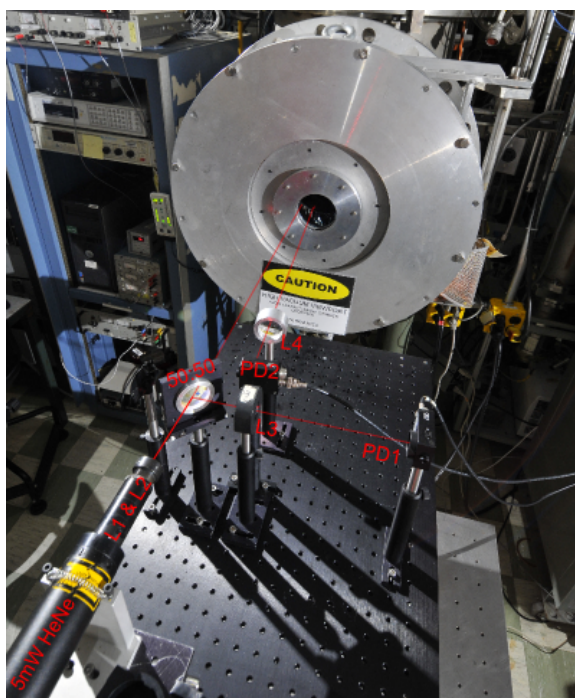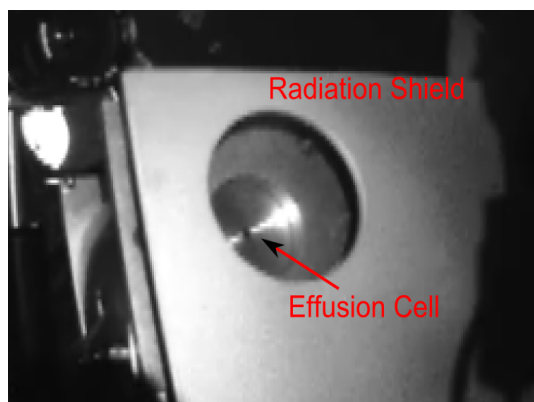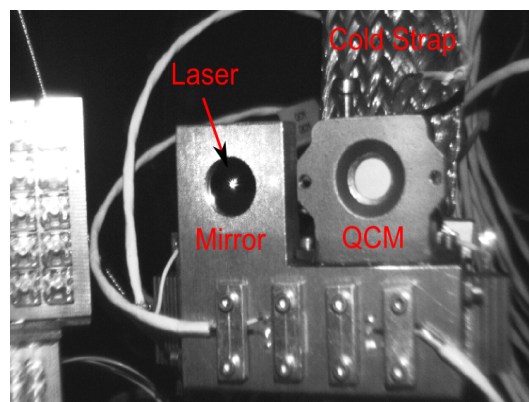
Figure 4.13: Images of the experimental setup for the second test of the cryodeposit experiment. The image in (a) shows the interferometer setup outside of the UHV chamber. The zeolite antechamber is located beneath the UHV chamber. Images (b) and (c) show the effusion cell with the radiation shield and the mirror and QCM setup respectively.
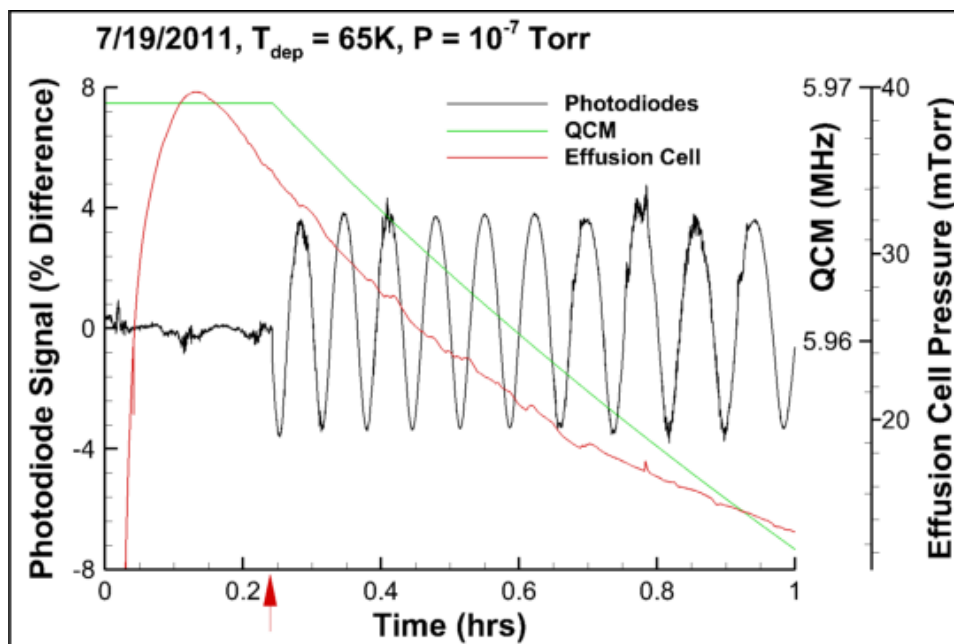
Figure 4.14: Data from the second test of the cryodeposit experiment. The red arrow on the x-axis marks the opening of the shutter.
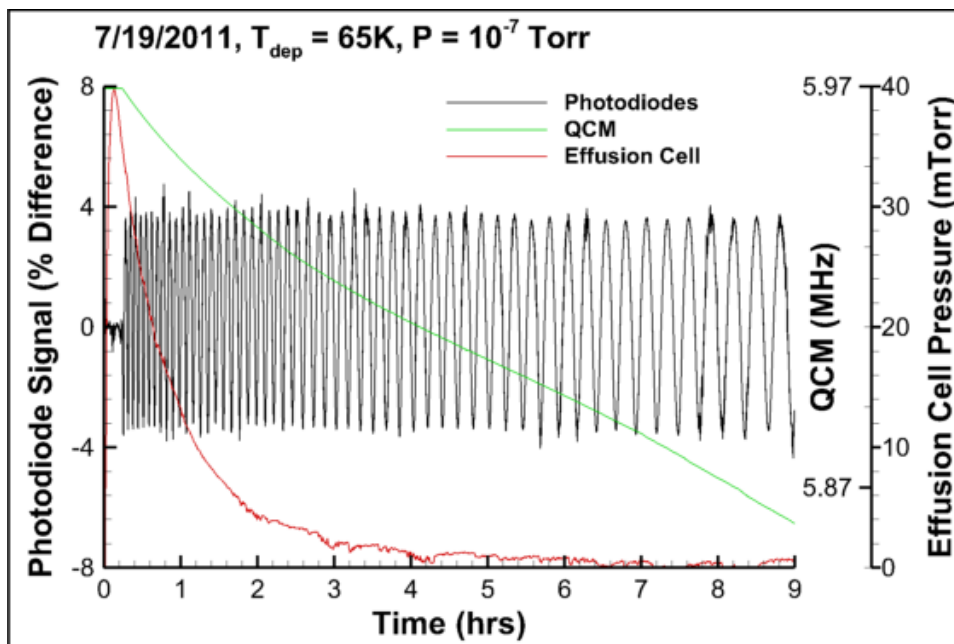
Figure 4.15: Data from several hours of the second test. The interference fringes spread out as the zeolite sample became dehydrated indicating a slower growth rate of the film.

deposition (decrease in frequency) and then another sudden increase. This event is displayed in Figure 4.16. Shortly after the second sudden increase the QCM failed. QCM's are known to fail once too much mass is on the deposition surface. This was expected to happen eventually. QCM failure is marked by a constant reading (flat line). The behavior of the QCM before failure is consistent with the film fracturing. As the film fractures, it delaminates from the surface of the QCM and causes sudden jumps in the frequency reading (Westley et al. (1998); Pugh (2003)). The behavior of the reflectance from a fractured film was unknown going into the test although it was expected that a fractured film would scatter light and cause a sudden drop in the photodiode reading. As can be seen in Figure 4.16, nothing so dramatic happened although there does appear to be a small anomaly in the minima of the fringes near the fracture point (Figure 4.17). The fracture event occurred overnight. Shown in Figure 4.18 are images of the QCM and mirror taken before leaving for the night and early the next morning. There were no obvious signs of film fracture present.
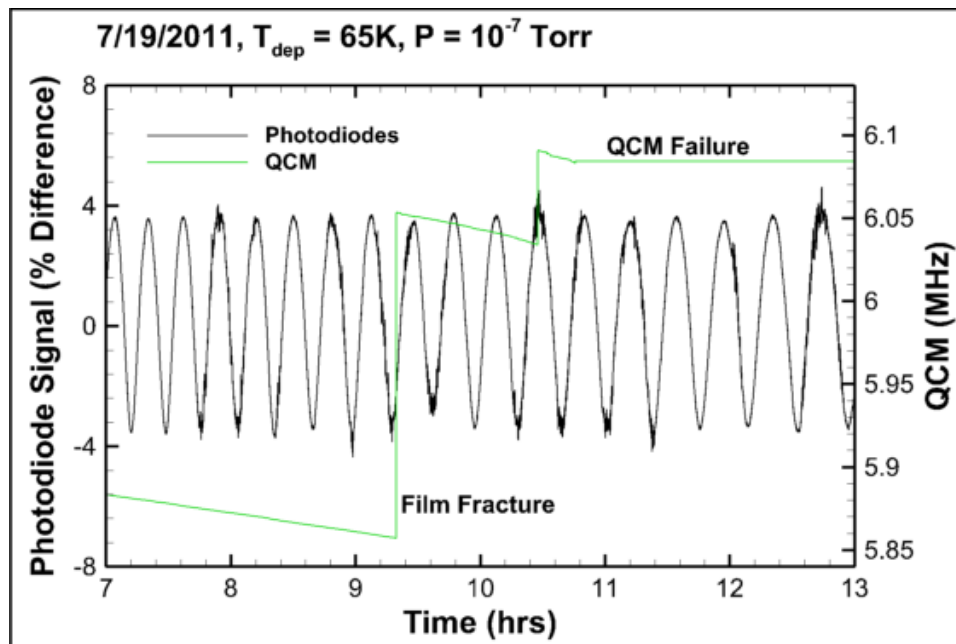
Figure 4.16: Display of the suspected film fracture during the second test of the cryodeposit experiment. The QCM failed approximately 90 minutes after the fracture event.

69
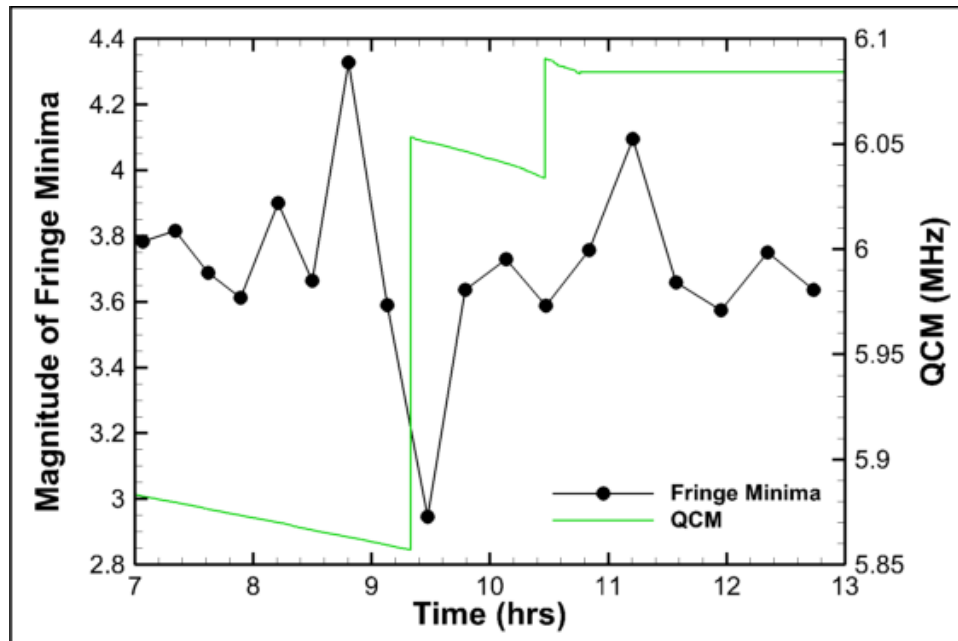
Figure 4.17: Display of the anomaly in the photodiode readings at the time of the suspected film fracture.

(a)

(b)
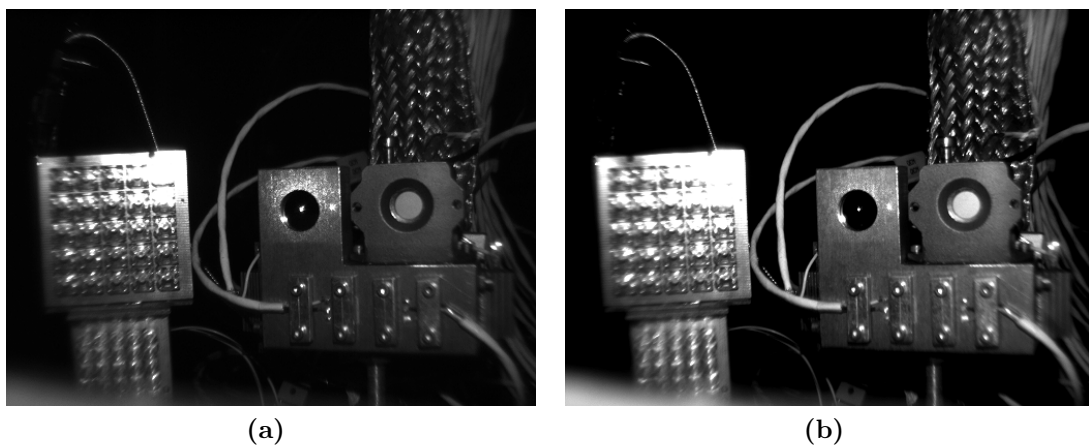
Figure 4.18: Images of the mirror a few hours before (a) and after (b) the suspected film fracture. There was no obvious evidence of the ice film fracturing.

Three more zeolite samples were used during the remainder of the test. The setup of the zeolite antechamber worked well in allowing the zeolite samples to be switched in and out without disrupting the UHV chamber. At the conclusion of the test the ice film was approximately $100\mu m$ thick. The QCM and mirror were warmed in increments to room temperature over a period of four hours and the behavior of the film upon warming was monitored. At the beginning of the warmup the ice film was still very clear and nearly invisible. As temperatures approached 180K the laser spot was seen to grow due to scattering. Soon thereafter the ice film became quite visible and the scattering became intense. Images taken during the warmup can be seen in Figure 4.19.

4.2.1 Initial Data Analysis

The mass density (g/cm^2) of the film on the QCM is determined from the frequency response through the equation (Smith (2007))

$$m_d = \left(\frac{N_q \rho_q}{\pi Z f} \right) \tan^{-1} \left[Z \tan \left(\frac{\pi (f_q - f)}{f} \right) \right], \qquad (4.1)$$

where

- $N_q = 1.668 \cdot 10^5 \, Hz \, cm$ is a constant for AT quartz crystal,

- $\rho_q = 2.648 \frac{g}{cm^3}$ is the density of quartz,

- f_q is the unloaded frequency,

- f is the loaded frequency (variable), and

- $Z \approx 4.8$ for LDA films is a unitless constant related to the shear modulus and density of quartz and the film being grown.

71
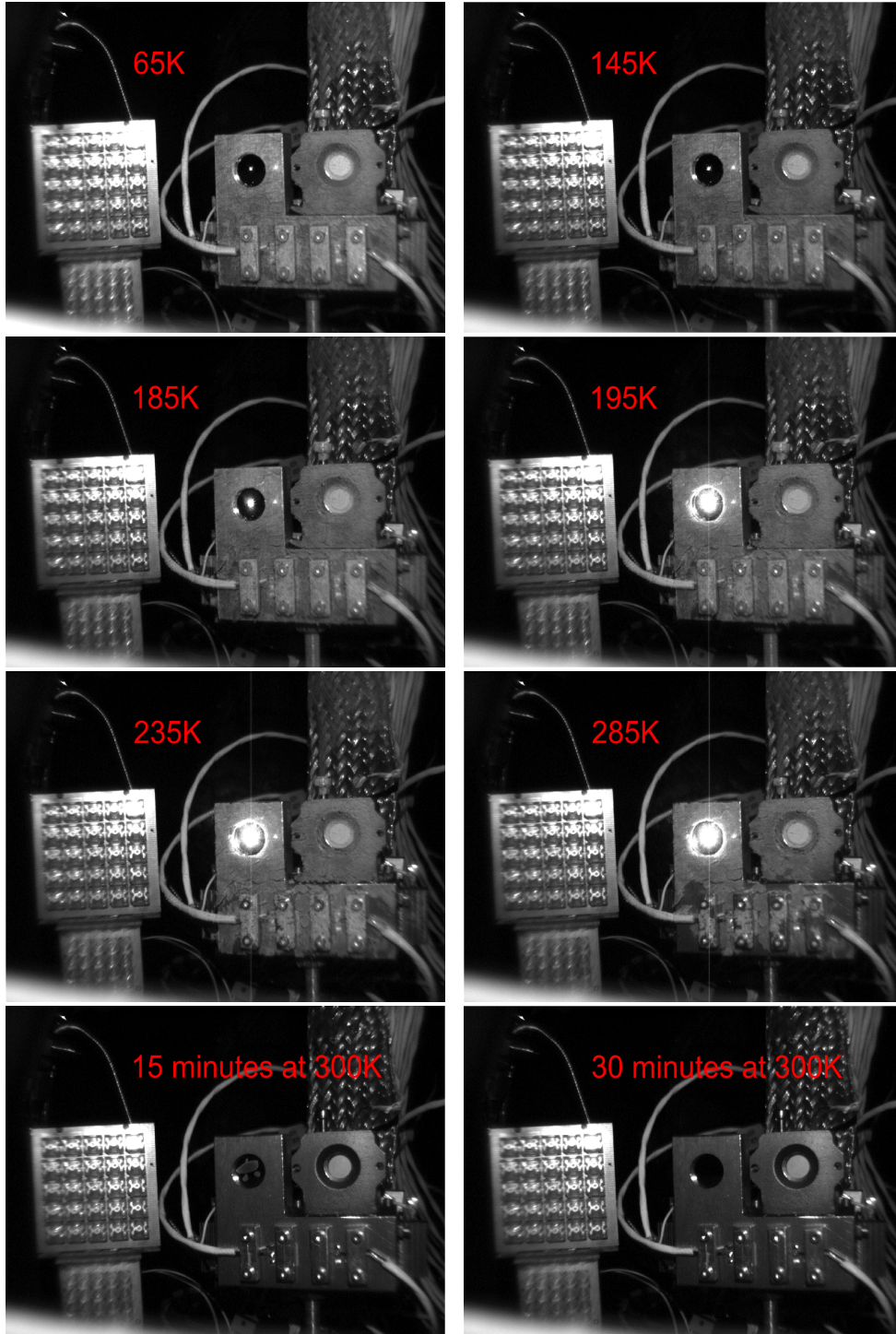
Figure 4.19: Sequence of images taken during the warmup of the mirror and QCM at the conclusion of the second test. The laser was turned off in the final two images. The temperatures listed were recorded by the sensors seen on the front of the mount below the mirror and QCM. The ice film was about $100\mu m$ at the beginning of the warmup.

If the density of the film is known, the thickness can be determined as

$$d = \frac{m_d}{\rho}. \tag{4.2}$$

If m_d is measured over time, the slope of the line is the depositing mass flux $\left(\frac{g}{cm^2 s}\right)$ and the thickness growth rate of the film is

$$\eta = \frac{\dot{m}_d}{\rho}. \tag{4.3}$$

For the optical data, the distance between interference maxima represents a thickness of

$$d_m = \frac{\lambda}{2n_2 \cos \theta_2}, \tag{4.4}$$

or, using Snell's law,

$$d_m = \frac{\lambda}{2\sqrt{n_2^2 - n_1^2 \sin^2 \theta_1}}, \tag{4.5}$$

where $\lambda = 632.8nm$, $n_1 = 1$, $n_2 \approx 1.28$, and $\theta_1 = 1.35°$ is the angle incidence on the ice film (see Figure 4.20). These values give $d_m = 247nm$. The mass as measured by the QCM is compared to the mass determined from the optical data in Figure 4.21.
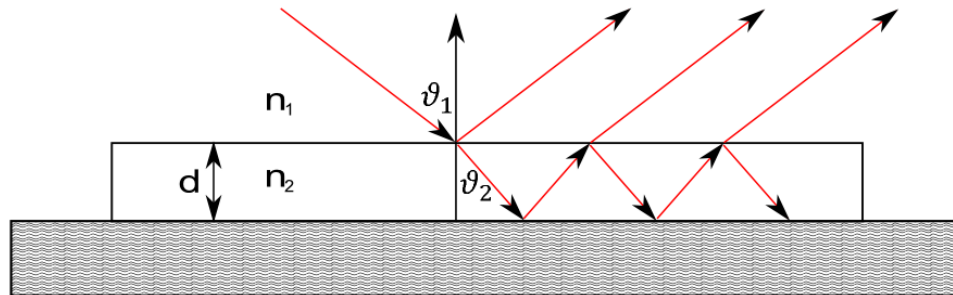
Figure 4.20: Diagram of interference from a thin film on a reflecting substrate.

Approved for public release; distribution is unlimited.
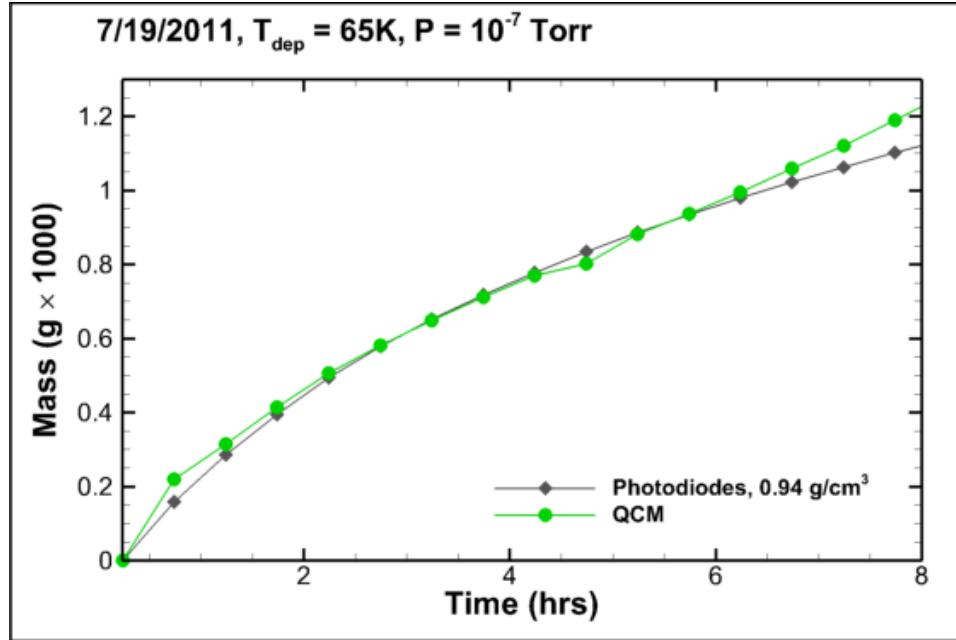
Figure 4.21: The measured mass deposited on the QCM and mirror. The mass on the mirror is determined by the measuring the thickness of the film and assuming a density for the film. The density here is assumed to be the nominal density of LDA (0.94 g/cm^3).

A more detailed analysis to yield the refractive index and density of the film will fit the measured reflectance to the analytical reflectance derived from Fresnel's equations

$$R = \left| \frac{r_2 + r_g e^{-2i\delta_2}}{1 + r_2 r_g e^{-2i\delta_2}} \right|^2, \qquad (4.6)$$

$$\delta_2 = \frac{2\pi n_2 d}{\lambda} \cos\theta_2,$$

where r_2 and r_g are the Fresnel coefficients of the vacuum-film and film-gold interfaces respectively. This analysis is currently ongoing and the results are expected to be published. Using the assumed density of 0.94 g/cm^3, the QCM shows a thickness of 15μm at the first sudden drop in frequency (Figure 4.16). This value agrees well with the data of (Bahr (2001)) and strengthens the evidence that the sudden jumps in the QCM reading were caused by film fracture (see Figure 4.22).

74
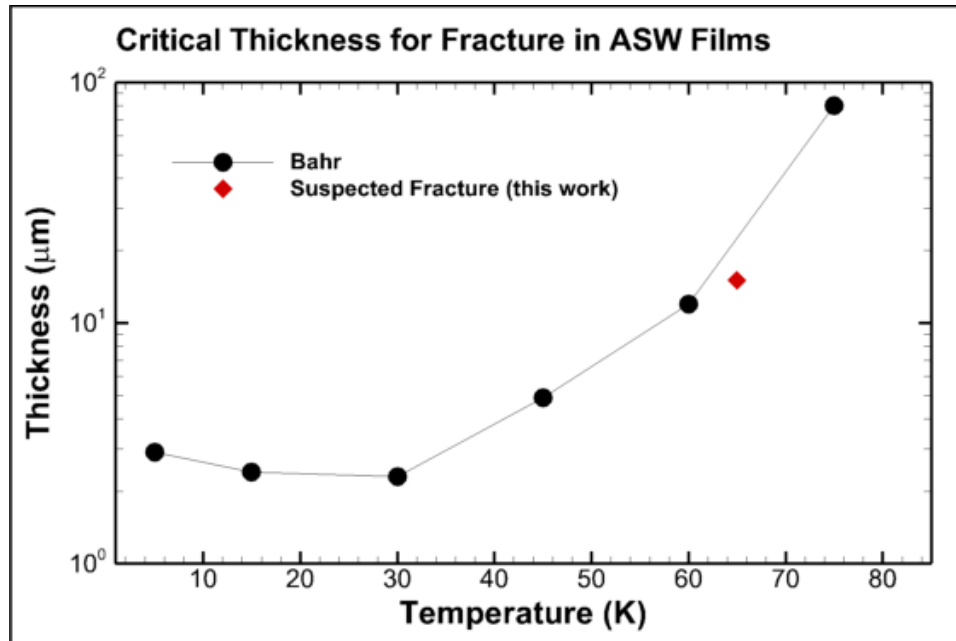
Figure 4.22: Comparison of the suspected fracture point to the data of (Bahr (2001)).

4.3 Future Work

The first test of the cryodeposit experiment provided good information that allowed for an improved second test. The second test was successful in growing and measuring thin ice films and proved that the setup developed for this experiment is capable of detecting and studying films and their fracture. Of course, there is always room for improvement. The temperature of the mirror and QCM needs to be brought down to lower temperatures to get into the operational region of the space chambers. This is especially needed in order to measure the critical thickness for fracture of the films as the fracture point drops significantly with temperature. After the second test, it is clear that active cooling will be needed in order to bring the temperature of the mirror and QCM further down. The mount was well thermally connected to the GHe lines and precautions against thermal radiation were taken in the second test and still the temperature stayed well above the desired range. Active cooling would require another redesign of the mount to allow the GHe to flow directly through it, effectively making the mirror and QCM mount a cold finger. Also, there was an RGA

installed on the UHV chamber for the second test, but its port location was behind the cryoliner such that all gases froze out before reaching the port. The result was that the RGA gave a null reading for the entirety of the test. The RGA operated normally at the conclusion of the second test when the chamber was warmed up to confirm that the null readings were a result of the port location and not instrument malfunction. For future tests, the RGA port should be plumbed into the cryoliner and as near the mirror and QCM as feasible. The HeNe laser at 632.8nm provided adequate ($\approx 8\%$) reflectance intensity modulation, however this could be much improved by using a shorter wavelength blue or green laser with expected modulation of greater than 20% (see Figure 4.23).
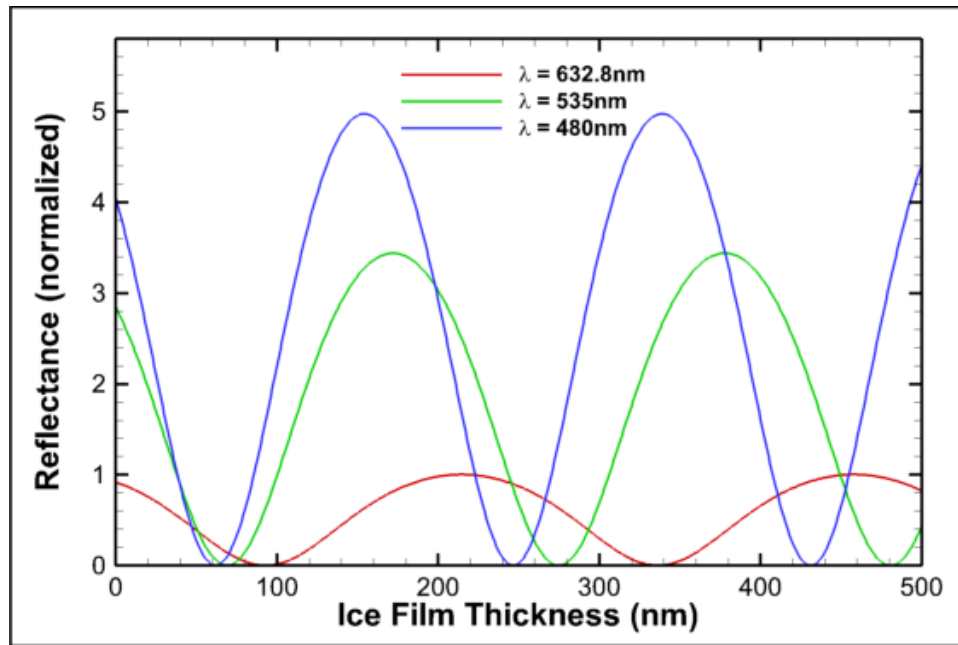
Figure 4.23: Expected fringes from an LDA film on gold at blue and green wavelengths normalized to the 632.8nm value.

With the current experimental arrangement, thought can go into the study of various methods of mitigation or prevention of cryodeposits along with basic scientific inquiry. One such experiment planned will modify the mirror and QCM mount by electrically isolating the mirror from the rest of the mount. This will be accomplished with the use of a tile of aluminum nitride. Aluminum nitride is a ceramic that exhibits

Approved for public release; distribution is unlimited.

excellent thermal conductivity and yet is also an excellent electrical insulator. With the mirror electrically isolated, a potential (alternating or constant) can be placed on the mirror and the effects on growth rate can be compared to the QCM which will be grounded.

Chapter 5

Conclusion

A study of cryodeposits may combine diverse areas of physics such as kinetic theory or mass transport equations with optical methods and surface science techniques, not to mention the computational techniques that are effectively a prerequisite for detailed analysis of any but the most ideal situations. Furthermore, although the motivation here was to study cryodeposits because they can cause problems in the space chambers at AEDC, thin films of ice at cold temperatures and low pressures are of considerable interest to the space and astrophysical communities due not only to contamination of satellites and scientific instruments in space (e.g. see Wood et al. (2003)), but also due to the prevalence of low pressure ices in the universe (Soper (2002)). The complexity exhibited by the water molecule in its interactions adds to the richness of the subject and the utility of results obtained through fundamental scientific curiosity.

This dissertation has discussed a method to calculate free molecular flux distributions (and, hence, film growth rates) in general three dimensional situations. Such a method was needed for the space chambers in order to predict where contamination will be problematic given any configuration of components in the chambers. This method was tested successfully for numerous cases and then applied to a basic model of the 10V chamber. Also discussed was a method to predict the effect of a given

Approved for public release; distribution is unlimited.

amount of contamination on some optical element. Although this was one of the simpler results to obtain, it may be the most crucial from a practical standpoint as prediction of when the cryodeposits will become problematic and must be removed can save time and money during operation of the space chambers. Of course the contamination of chamber optics must be monitored in order for the thickness to be known. To address this issue, an experiment to measure the thickness, and other properties, of contaminant films was setup. This experiment is still under development, but the second test of the experiment demonstrated clearly that the methodology is effective.

An ideal scenario for the space chambers would be to prevent cryodeposits from ever forming. There is no obvious method to attain this goal, but some ideas are discussed in Appendix D. Short of that, the best that can be done is mitigation and accounting. Mitigation is primarily achieved through discipline in following good vacuum practices. By routinely cleaning, leak checking, and having a knowledge of materials being put in the chamber and their outgassing properties, the sources of residual gas and cryodeposits can be minimized. The tool developed and described in Chapter 2 can be used to analyze hypothetical outgassing situations and should be able to help determine the best placement and design for baffles placed between contamination sources and sensitive surfaces. Also, although not done here, the distributions determined by that tool could be combined with the method of Chapter 3 to determine the overall impact of a hypothetical outgassing situation on the chamber throughput. This is an example of one avenue of future work. Combining the distributions calculated as in Chapter 2 with a method to integrate time dependent outgassing properties can give a thickness of contaminant films throughout the chamber over time. Then the method of Chapter 3 can be brought in to calculate the overall impact on the spectral characteristics of each component and of the chamber as a whole. The combination of the methods could give an accurate prediction of contaminant build-up and the spectral impact of those contaminants over time.

Bibliography

Bibliography

AVS: Science & Technology of Materials, Interfacing, and Processing (2011). AVS Technical Resources - Vapor Pressure Data. `http://www.avsbuyersguide.org/refguide/vapor.html`. 4

Bahr, D. (2001). *Chemical Physics of Frozen Gases: Sublimation, Morphology, and Radiation Effects*. PhD thesis, The University of Virginia. xii, 59, 61, 74, 75

Baragiola, R. (2003). *Water in Confining Geometries*, chapter 15. Springer-Verlag, Berlin. ISBN: 3540004114. 59

Benedict, W., Gailer, N., and Plyler, E. (1956). Rotation-vibration spectra of deuteriated water vapor. *J. Chem. Phys.*, 24:1139–65. 9

Berland, B., Brown, D., Tolbert, M., and George, S. (1995). Refractive index and density of vapor-deposited ice. *Geophysical Research Letters*, 22:3493. 19

Bird, G. A. (2005). The DS2V/3V program suite for DSMC calculations. *AIP Conference Proceedings*, 762(1):541–546. 35, 102

Blears, J., Greer, E. J., and Nightingale, J. (1960). Factors Determining the Ultimate Pressure in Large High-Vacuum Systems. In E. Thomas, editor, *Advances in Vacuum Science and Technology*, page 473. 48

Born, M. and Wolf, E. (1964). *The Principles of Optics*. Pergamon Press, Oxford, 2nd edition. 16, 49, 50

Approved for public release; distribution is unlimited.

Bramwell, S. (1999). Condensed-matter science: Ferroelectric ice. *Nature*, 397:212. 19

Brinker, C. (2008). Superhydrophobic coating. Technical report, Sandia National Laboratories. 113

Brown, D. and George, S. (1996). Surface and bulk diffusion of $H_2^{18}O$ on single-crystal $H_2^{16}O$ ice multilayers. *J. Phys. Chem.*, 100:15460. 15

Brown, D., George, S., Huang, C., Wong, E., Rider, K., Smith, R., and Kay, B. (1996). H_2O condensation coefficient and refractive index for vapor-deposited ice from molecular beam and optical interference measurements. *J. Phys. Chem.*, 100:4988. 19, 23

Bubb, D., Johnson, S., Collins, B., and Haglund, R. (2010). Thermal confinement and temperature-dependent absorption in resonant infrared ablation of frozen liquid targets. *J. Phys. Chem. C*, 114:5611 – 5616. 22

Cai, C. and Liu, D. (2008). Collisionless gas flows. I. Inside arbitrary enclosures. *Physics of Fluids*, 20:067105–1. 92

Cai, C. and Sun, Q. (2010). Exact Solutions to Collisionless External Gas Flow Problems. In *American Institute of Physics Conference Series*, volume 1233 of *American Institute of Physics Conference Series*, pages 1034–1039. 92

Cao, L., Jones, A., Sikka, V., Wu, J., and Gao, D. (2009). Anti-icing superhydrophobic coatings. *Langmuir*, 25:12444. 114

Cathcart, G. and Macrossan, M. (1995). Satellite protection and drag reduction using a purging gas flow. In Harvey, J. and Lord, G., editors, 19th *International Symposium*, volume 2 of *Rarefied Gas Dynamics*, pages 1380 – 1386. 110

Day, C. (2007). Basics and applications of cryopumps. Technical report, CERN. 3

Approved for public release; distribution is unlimited.

Debenedetti, P. (2003). Supercooled and glassy water. *J. Phys. Condens. Matter*, 15:R1669 – R1726. 10

Dohnálek, Z., Kimmel, G., Ayotte, P., Smith, R., and Kay, B. (2003). The deposition angle-dependent density of amorphous solid water films. *J. Chem. Phys.*, 118:364. 18, 19

Dreisewerd, K. (2003). The desorption process in MALDI. *Chem. Rev.*, 103:395 – 425. 111

Dreisewerd, K., Shurenberg, M., Karas, M., and Hillenkamp, F. (1995). Influence of the laser intensity and spot size on the desorption of molecules and ions in matrix-assisted laser desorption/ionization with a uniform beam profile. *International Journal of Mass Spectrometry and Ion Processes*, 141:127 – 148. 22

Drobyshev, A., Aldiyarov, A., Zhumagaliuly, D., Kurnosov, V., and Tokmoldin, N. (2007a). Thermal desorption and IR spectrometric investigation of polyamorphic and polymorphic transformations in cryovacuum condensates of water. *Low Temperature Physics*, 33:472. 11

Drobyshev, A., Aldiyarov, A., Zhumagaliuly, D., Kurnosov, V., and Tokmoldin, N. (2007b). Thermally stimulated transformations in cryovacuum water ices. *Low Temperature Physics*, 33:355. 11

Fletcher, N. (1970). *The Chemical Physics of Ice*. Cambridge Univ. Press, Cambridge. 8

Focsa, C., Chazallon, B., and Destombes, J. (2003). Resonant desorption of ice with a tunable $LiNbO_3$ optical parametric oscillator. *Surface Science*, 528:189–195. 22, 23

Focsa, C., Mihesan, C., Ziskind, M., Chazallon, B., Therssen, E., Desgroux, P., and Destombes, J. (2006). Wavelength-selective vibrationally excited photodesorption with tunable IR sources. *J. Phys.: Condens. Matter*, 18:S1357 – S1387. 22, 112

Fraser, H., Collings, M., McCoustra, M., and Williams, D. (2001). Thermal desorption of water-ice in the interstellar medium. *Mon. Not. R. Astron. Soc.*, 327:1156. 21

Ghormley, J. and Hochanadel, C. (1971). Amorphous ice: Density and reflectivity. *Science*, 171:62. 17

Grossman, L. (2011). Electric ice: A shock to the solar system. *New Scientist*, 2827. 7

Guenther, R. (1990). *Modern Optics*. John Wiley & Sons, New York. ISBN: 0471605387. 18

Hablanian, M. (1997). *High-Vacuum Technology*. Marcel Dekker Inc., New York, 2nd edition. ISBN: 0824798341. 110

Hagen, J. (2006). *Industrial Catalysis: A Practical Approach*. Wiley-VCH, Weinheim. ISBN: 352731140. 62

Hale, G. and Querry, M. (1973). Optical constants of water in the 200-nm to 200-μm wavelength region. *Applied Optics*, 12:555–563. 10, 13

Hawkins, G. H. (1998). *Spectral characterisation of infrared optical materials and filters [Electronic Version]*. PhD thesis, The University of Reading, Infrared Laboratory. 49

Haynes, D., Tro, N., and George, S. (1992). Condensation and evaporation of water on ice surfaces. *J. Phys. Chem.*, 96:8502. 21, 23

He, M., Wang, J., Li, H., Jin, X., Wang, J., Liu, B., and Song, Y. (2010). Super-hydrophobic film retards frost formation. *Soft Matter*, 6:2396–2399. 114

Hess, R. (2010). *Blender Foundations: The Essential Guide to Learning Blender 2.6*. Focal Press, Amsterdam. ISBN: 0240814304. 30

Hobbs, P. (1974). *Ice Physics*. Oxford Univ. Press, London. 9, 12, 112

Holland, L. and Steckelmacher, W. (1952). The distribution of thin films condensed on surfaces by the vacuum evaporation method. *Vacuum*, 2(4):346 – 364. 33, 38

Honig, R. and Hook, H. (1960). Vapor pressure data for some common gases. *RCA Review*, 21:360–368. 4

Hudgins, D., Sandford, S., Allamandola, L., and Tielens, A. (1993). Mid- and far-infrared spectroscopy of ices: Optical constants and integrated absorbances. *The Astrophysical Journal Supplement Series*, 86:713. 13, 14, 23

Iedema, M., Dresser, M., Doering, D., Rowland, J., Hess, W., Tsekouras, A., and Cowin, J. (1998). Ferroelectricity in water ice. *J. Phys. Chem. B*, 1998:9203. 19, 20

Jenniskens, P. and Blake, D. (1994). Structural transitions in amorphous water ice and astrophysical implications. *Science*, 265:753. 11

Jones, E., Oliphant, T., Peterson, P., et al. (2001). SciPy: Open source scientific tools for Python. `http://www.scipy.org/`. 30

Jung, K., Park, S., Kim, J., and Kang, H. (2004). Vertical diffusion of water molecules near the surface of ice. *J. Chem. Phys.*, 121:2758. 15

Kimmel, G., Dohnálek, Z., Stevenson, K., Smith, R., and Kay, B. (2001). Control of amorphous solid water morphology using molecular beams. II. Ballistic deposition simulations. *J. Chem. Phys.*, 114:5295. 16

Krasnopoler, A. and George, S. (1998). Infrared resonant desorption of H_2O from ice multilayers. *J. Phys. Chem. B*, 102:788–794. 22, 23, 112

Labello, J. (2007). Characterization of the temperature dependence of optical components in a cryo-vacuum chamber used for space sensor testing. Master's thesis, University of Tennessee Space Institute. 51, 55

Approved for public release; distribution is unlimited.

Landau, R., Paez, M., and Bordeianu, C. (2007). *Computational Physics*. Wiley-VCH, Weinheim, 2nd edition. ISBN: 3527406263. 30, 103

Larouche, S. and Martinu, L. (2008). OpenFilters: open-source software for the design, optimization, and synthesis of optical filters. *Applied Optics*, 47:C219. 51

Livingston, F., Smith, J., and George, S. (2000). Depth-profiling and diffusion measurements in ice films using infrared laser resonant desorption. *Anal. Chem.*, 72:5590 – 5599. 22

Loerting, T. and Giovambattista, N. (2006). Amorphous ices: Experiments and numerical simulations. *J. Phys.: Condens. Matter*, 18:R919. 11

Loerting, T., Winkel, K., Seidl, M., Bauer, M., Mitterdorfer, C., Handle, P., Salzmann, C., Mayer, E., Finney, J., and Bowron, D. (2011). How many amorphous ices are there? *Phys. Chem. Chem. Phys.*, 13:8783. 10

Lowry, H., Crider, D., Burns, J., Thompson, R., Goldsmith, II, G., and Sholes, W. (2006). Development of HWIL Testing Capabilities for Satellite Target Emulation at AEDC. In *The Advanced Maui Optical and Space Surveillance Technologies Conference*. 6

Lowry, H., Nicholson, R., Simpson, R., Mead, K., and Crider, D. (2004). Ground testing of space-based imaging sensors in AEDC's space chambers. In *24th AIAA Aerodynamic Measurement Technology and Ground Testing Conference Proceedings*. 3

Lowry, H., Nicholson, R., Simpson, R., Mead, K., Crider, D., and Breedan, M. (2005). Test and evaluation of sensor platforms in AEDC space sensor test chambers. In *U.S. Air Force T&E Days*. 3

Mishima, O. (1996). Relationship between melting and amorphization of ice. *Nature*, 384:546 – 549. 7

Nie, S., Bartlett, N., and Thürmer, K. (2009). Observation of surface self-diffusion on ice. *Physical Review Letters*, 102:136101. 15

Ohring, M. (2001). *Material Science of Thin Films: Deposition and Structure*, pages 106 – 113. Academic Press, New York, 2nd edition. ISBN: 0125249756. 14, 28, 33, 102

Ossipov, P. (1997). The angular coefficient method for calculating the stationary molecular gas flow for arbitrary reflection law. *Vacuum*, 48(5):409 – 412. 32

Park, S., Moon, E., and Kang, H. (2010). Some fundamental properties and reactions of ice surfaces at low temperatures. *Phys. Chem. Chem. Phys.*, 12:12000. 15

Prialnik, D., Benkhoff, J., and Podolak, M. (2004). *Comets II*, chapter 22, pages 359–387. University of Arizona Press, Tucson. 112

Prockter, L. (2005). Ice in the solar system. *John Hopkins APL Technical Digest*, 26:175. 12

Pugh, D. (2003). Characterization of nanoscale porosity and cracking in amorphous solid water thin films. Master's thesis, University of Virginia. 18, 59, 69

Rogers, J. (2011). Introduction of water vapor into an ultra high vacuum chamber at AEDC. Master's thesis, University of Tennessee. 62, 63, 64, 101

Roux, J., Wood, B., and Smith, A. (1979). IR optical properties of thin H_2O, NH_3, and CO_2 cryofilms. Technical report, Arnold Engineering Development Center. AEDC-TR-79-57. 13, 14

Sack, N. and Baragiola, R. (1993). Sublimation of vapor-deposited water ice below 170K, and its dependence on growth conditions. *Physical Review B*, 48:9973. 14

Sahu, G. and Thakur, K. (2006). Spatial distribution of copper vapour from a two-dimensional source using a strip electron beam at aspect ratio greater than 3. *Vacuum*, 81:77. 102

Approved for public release; distribution is unlimited.

Saksaganskii, G. (1988). *Molecular Flow in Complex Vacuum Systems.* Gordon and Breach, New York. ISBN: 2881246583. 27, 29

Seiber, B., Smith, A., Wood, B., and Müller, P. (1971). Refractive indices and densities of H_2O and CO_2 films condensed on cryogenic surfaces. *Applied Optics*, 10:2086. 12

Smith, A. (2007). *Thermal Analysis and Calorimetry: Recent Advances, Techniques, and Applications*, volume 5, chapter 5. Elsevier Science, Amsterdam. 71

Smith, R., Huang, C., Wong, E., and Kay, B. (1996). Desorption and crystallization kinetics in nanoscale thin films of amorphous water ice. *Surface Science*, 367:L13. 21

Soper, A. (2002). Water and ice. *Science*, 297:1288–1289. 10, 78

Soper, A. (2008). Structural transformations in amorphous ice and supercooled water and their relevance to the phase diagram of water. *Molecular Physics*, 106:2053 – 2076. 11

Su, X., Lianos, L., Shen, Y. R., and Somorjai, G. (1998). Surface-induced ferroelectric ice on Pt(111). *Phys. Rev. Lett.*, 80:1533. 19

Thakur, K. and Sahu, G. (2004). Spatial distribution for vapour flow and its validation for a two-dimensional source generated using strip electron beam. *Vacuum*, 75:283. 102

Tribble, A., Boyadjian, B., Davis, J., Haffner, J., and McCullough, E. (1996). Contamination Control Engineering Design Guidelines. Technical report, NASA. NASA Contractor Report 4740. 110

Umrath, W. (2007). Fundamentals of vacuum technology. Technical report, Oerlikon Leybold Vacuum. 2, 3

Öberg, K., Linnartz, H., Visser, R., and van Dishoeck, E. (2009). Photodesorption of ices II: H_2O and D_2O. *The Astrophysical Journal*, 693:1209. 22

Vinciquerra, J. (2009). Creating anti-icing surfaces. `http://ge.geglobalresearch.com/blog/creating-anti-icing-surfaces/`. 113

Wang, H., Bell, R., Iedema, M., Tsekouras, A., and Cowin, J. (2005). Sticky ice grains aid planet formation: Unusual properties of cryogenic water ice. *The Astrophysical Journal*, 620:1027. 19, 20

Warren, S. (1984). Optical constants of ice from the ultraviolet to the microwave. *Applied Optics*, 23:1206. 12, 13

Westley, M., Baragiola, R., Johnson, R., and Baratta, G. (1995). Ultraviolet photodesorption from water ice. *Planet. Space Sci.*, 43:1311. 22

Westley, M., Baratta, G., and Baragiola, R. (1998). Density and index of refraction of water ice films vapor deposited at low temperatures. *J. Chem. Phys.*, 108:3321 – 3326. 19, 59, 69

Wood, B. and Smith, A. (1978). Infrared reflectance and refractive index of condensed gas films on cryogenic mirrors. In *Thermophysics and Thermal Control*. AIAA-2005-7634. 49, 59

Wood, B. E., Uy, O. M., Green, B. D., Bertrand, W. T., Lesho, J. C., and Hall, D. F. (2003). Review of Midcourse Space Experiment (MSX) satellite quartz crystal microbalance contamination results after 7 years in space. In K. Fletcher, editor, *Materials in a Space Environment*, volume 540 of *ESA Special Publication*, pages 503–508. 78

Appendix

Appendix A

Stationary Flow Properties Near Cryogenic Surfaces

It is tempting to take a pressure reading from a gauge on a vacuum chamber and assume that the pressure is uniformly that number throughout the chamber. Indeed, for a chamber at room temperature this may be an accurate assumption. However, as clearly indicated in Chapter 2, the situation is different for cryogenic chambers. Whenever there is a temperature distribution in the chamber there is also a pressure, number density, and flux distribution. One of the drawbacks to the method of angular coefficients is that it does not explicity calculate gas properties. However, for stationary flow conditions anyway, these properties can be simply determined. Consider a cryogenic substrate surrounded by a gas of number density n_0 in free molecular flow conditions. The probability that any one molecule from the gas will move to hit the substrate is (in 2D for simplicity)

$$P = \frac{\phi}{2\pi}, \tag{A.1}$$

where ϕ is the angle subtended by the cryogenic surface at the location of the molecule (see Figure A.1). Hence, if a number of molecules, N, arrive at that location at various times, the number of those molecules that will hit the substrate and be removed from

the gas is N times P. Therefore the number of those molecules remaining in the gas is
$N - PN$ or $(1 - P)N$. Extending this thought from a single point to an infinitesimal
volume allows the number density near an adsorbing surface to be written as (Cai
and Liu (2008); Cai and Sun (2010))

$$n = (1 - \frac{\phi}{2\pi})n_0. \tag{A.2}$$

Of course the extension to three dimensions is given by

$$n = (1 - \frac{\Omega}{4\pi})n_0, \tag{A.3}$$

where Ω is the solid angle subtended by the cold surface. Equation A.2 is compared
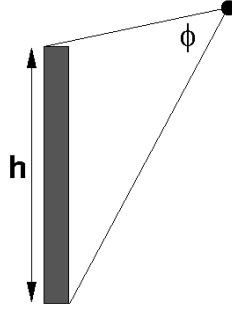to a 2D DSMC simulation in Figure A.2.

Figure A.1: Schematic to describe the gas properties near an adsorbing surface (in 2D).
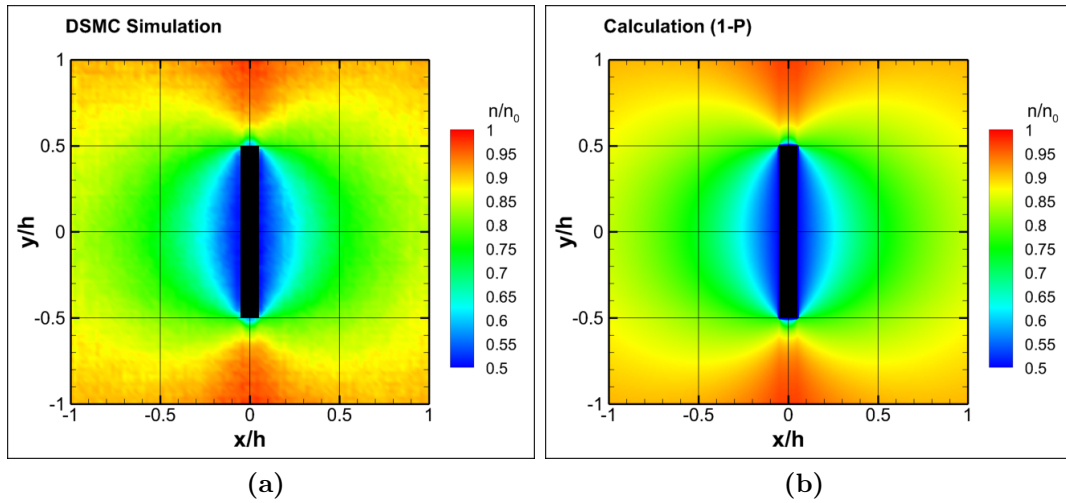
Figure A.2: A 2D DSMC simulation (a) compared to Equation A.2, (b), for a cold surface surrounded by a free molecular gas in stationary flow.

Appendix B

Discussion of the FMFlux Program

In Chapter 2, the terms *nodes* and *integration points* were used interchangeably. This is because in FMFlux they are the same thing. Nodes are points distributed across the geometry at which the flux density is calculated. Integration points are the points assigned to each face of the geometry in order to be able to integrate over the surface. The methodology in FMFlux is to use the integration points as the nodes. However, one could also choose nodes to be a different set of points and then interpolate flux density values from the nodes to the integration points when performing the integration. The benefit of the latter method becomes clear when considering geometries in which blocked views can occur. In this case, the amount of surface area visible to one node is not the same as the amount visible to a neighboring node. The 'view' is different from each node. In order to get an accurate integration over the surface, the integration points should be assigned to the visible area for each node. In other words, each node would have it's own set of integration points corresponding to it's view of the geometry. With the method used in FMFlux, the same set of integration points is used for every node. Simple illustrations of the different methods are shown in Figures B.1 and B.2. Certainly the former method is the more accurate one. However, the computational strain of that method could easily get enormous. As an example, consider a simple geometry

consisting of only 10 rectangular faces using 5 integration points per dimension per face. With the methodology used in FMFlux, this results in 250 nodes distributed across the geometry and the matrix in Equation 2.10 would be 250×250 for a total of 62500 elements. For the same number of nodes in the latter method, one could have up to 250 of these matrices, one for each node, and $250^3 = 1.5625 \times 10^7$ total elements.
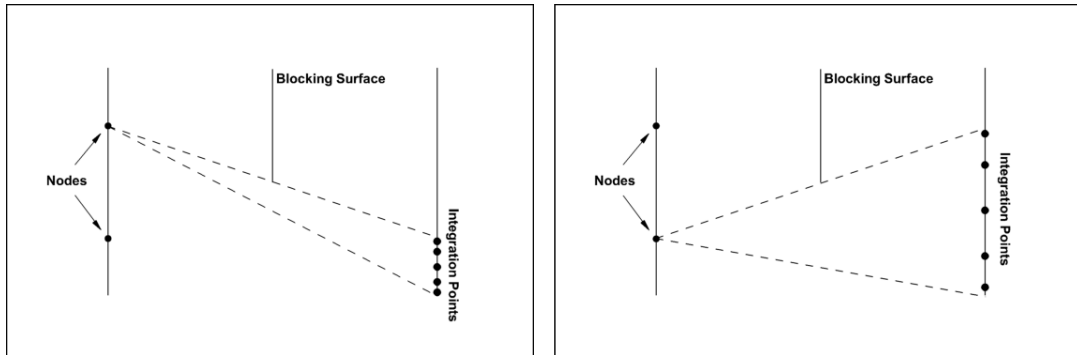
Figure B.1: Illustration of calculating visible areas using a different set of integration points for each node.
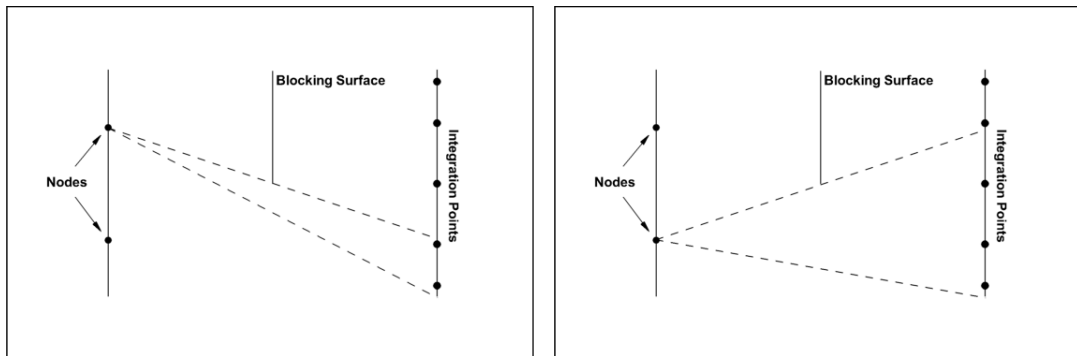
Figure B.2: Illustration of calculating visible areas using the method in FMFlux. The same set of integration points is used for each node, but only the integration points visible to the node contribute.

The error resulting from using the method in FMFlux can be illustrated by considering a rectangular area that is blocked in increments by some other surface. In FMFlux, when the line of sight between a node and an integration point is blocked,

95

the node receives zero contribution from the integration point. This results in Figure B.3. As can be seen, the error in the calculated area can be mitigated by using more integration points. However, this results in a heavier computational load so the trade-off must be considered. In situations of either no blockage or complete blockage of surface areas, this error is not present.
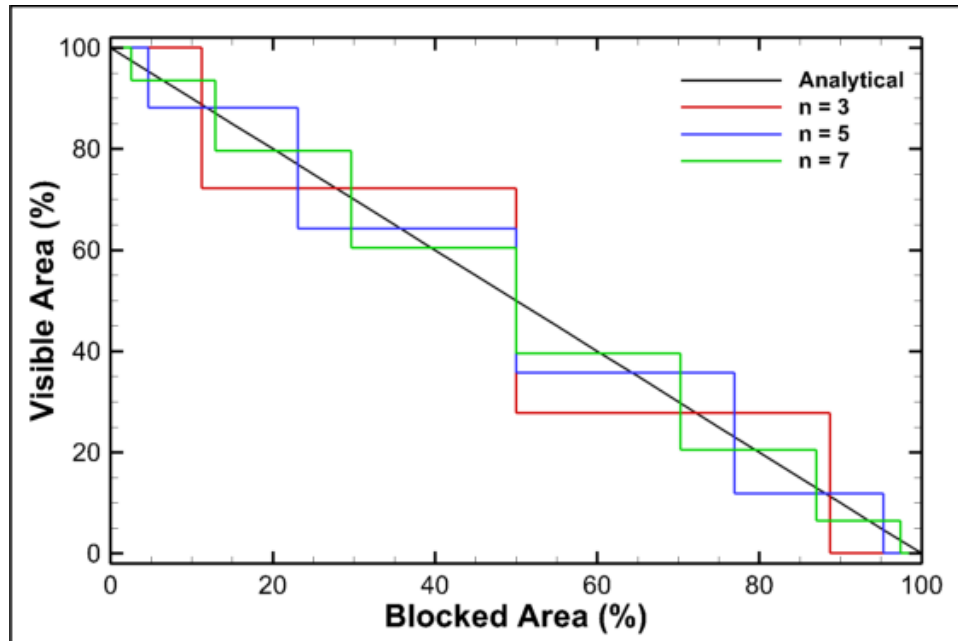

Figure B.3: Illustration of the error inherent to the method used in FMFlux when calculating areas that are partially blocked. Shown are the results for a rectangle as a function of blocked area. The area calculated by FMFlux is shown for 3, 5, and 7 integration points per dimension.

Appendix C

Characterization of the Effusion Cell

The experiment outlined in Chapter 4 requires the film to be grown uniformly over the QCM and the mirror in order for the measurements from each component to be comparable to the other. The film uniformity can be determined by analyzing the flux distribution arising from the effusion cell. The effusion cell is essentially a can with a large orifice in the back to allow water vapor to enter and a small orifice in the front for water vapor to exit towards the deposition surfaces. A drawing of the effusion cell can be seen in Figure C.1. If the flow is free molecular inside the effusion
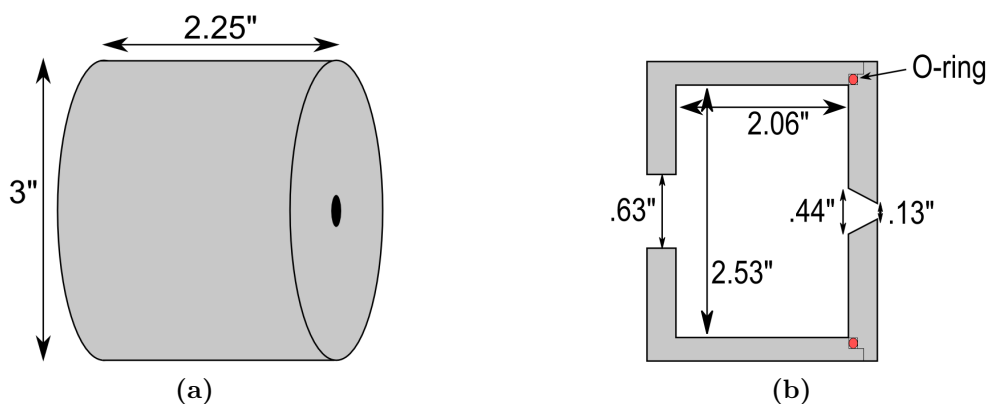

Figure C.1: An external view of the effusion cell, (a), and a cutaway view through the axis, (b).

Approved for public release; distribution is unlimited.

cell, then the flux leaving the orifice is described by the Knudsen cosine distribution. The leaving flux from the effusion cell orifice into the solid angle $d\Omega$ is then

$$q_{lvg} = \frac{n\langle v \rangle}{4\pi} \cos \phi \, d\Omega, \qquad (\text{C.1})$$

$$\langle v \rangle = \sqrt{\frac{8k_B T}{\pi m}}$$

where n is the number density inside the effusion cell and ϕ is the angle from the effusion cell axis. The part of this flux that arrives onto some deposition surface is given by the projection of $d\Omega$ onto the surface such that

$$q_{arr} = \frac{n\langle v \rangle A}{4\pi s^2} \cos \phi \, \cos \gamma, \qquad (\text{C.2})$$

where A is the area of the effusion cell orifice, $\mathbf{s}$ is the vector from the orifice to a point on the deposition surface and γ is the angle from the deposition surface normal to $\mathbf{s}$ (see Figure C.2).
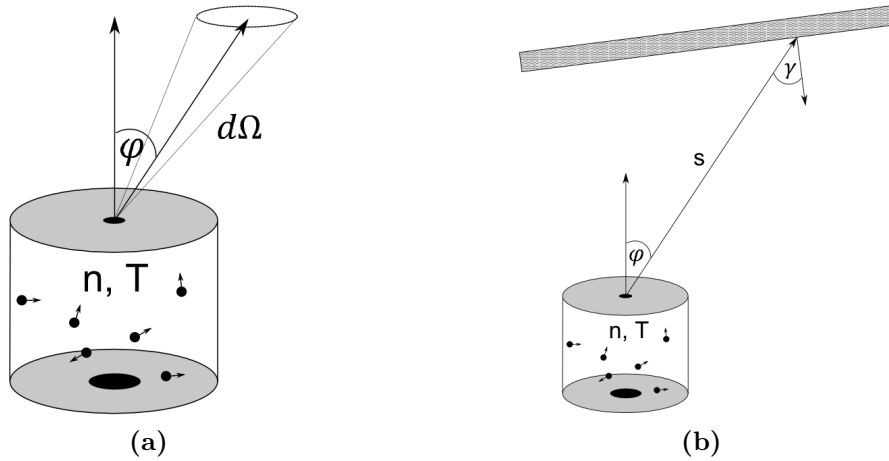

Figure C.2: Geometry to describe the flux leaving from the effusion cell (a) into solid angle $d\Omega$ and (b) onto a surface.

The QCM and mirror are 1.6cm off of the effusion cell axis and each has a diameter of about 1.27cm. To find the uniformity over the area of both of them, a disc of radius

1.6cm + .635cm = 2.235cm centered on the effusion cell axis is used to model the deposition area. The angle of incidence to the effusion cell axis is 20°. Denoting the vector from the center of the orifice to the center of the deposition disc as $\mathbf{s}_0$ and the angle of incidence as ϕ_0 and setting coordinates as in Figure C.3 the vector $\mathbf{s}$ can be written as

$$\mathbf{s} = \mathbf{s}_0 + \mathbf{r} = r\cos\theta\,\hat{\mathbf{i}} + (r\sin\theta + s_0\sin\phi_0)\,\hat{\mathbf{j}} + s_0\cos\phi_0\,\hat{\mathbf{k}}, \tag{C.3}$$

where θ is the angle on the disc from the x-axis. The required angles are

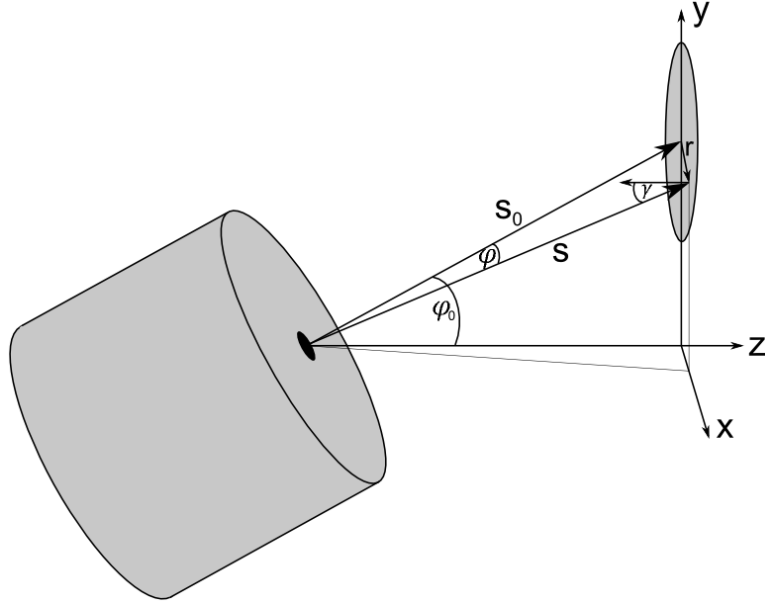**Figure C.3:** The setup to find the film uniformity over the QCM and mirror.

$$\cos\phi = \frac{\mathbf{s}_0 \cdot \mathbf{s}}{|\mathbf{s}|\,|\mathbf{s}_0|} = \frac{s_0 + r\sin\theta\sin\phi_0}{\sqrt{r^2 + s_0^2 + 2rs_0\sin\theta\sin\phi_0}}, \quad \text{and} \tag{C.4}$$

$$\cos\gamma = \frac{\mathbf{s} \cdot \hat{\mathbf{k}}}{|\mathbf{s}|} = \frac{s_0\cos\phi_0}{\sqrt{r^2 + s_0^2 + 2rs_0\sin\theta\sin\phi_0}},$$

99

and, defining $q_0 \equiv \frac{n\langle v \rangle}{4}$, the normalized flux density arriving on the deposition disc is

$$\frac{q_{arr}}{q_0} = \frac{A}{\pi} \left[\frac{s_0^2 \cos \phi_0 + r s_0 \sin \theta \sin \phi_0 \cos \phi_0}{(r^2 + s_0^2 + 2 r s_0 \sin \theta \sin \phi_0)^2} \right]. \tag{C.5}$$

Equation C.5 is shown in Figure C.4 where the values $\phi_0 = 20°$, $s_0 = 18.25$ cm, and $A = .08$ cm^2 have been inserted.
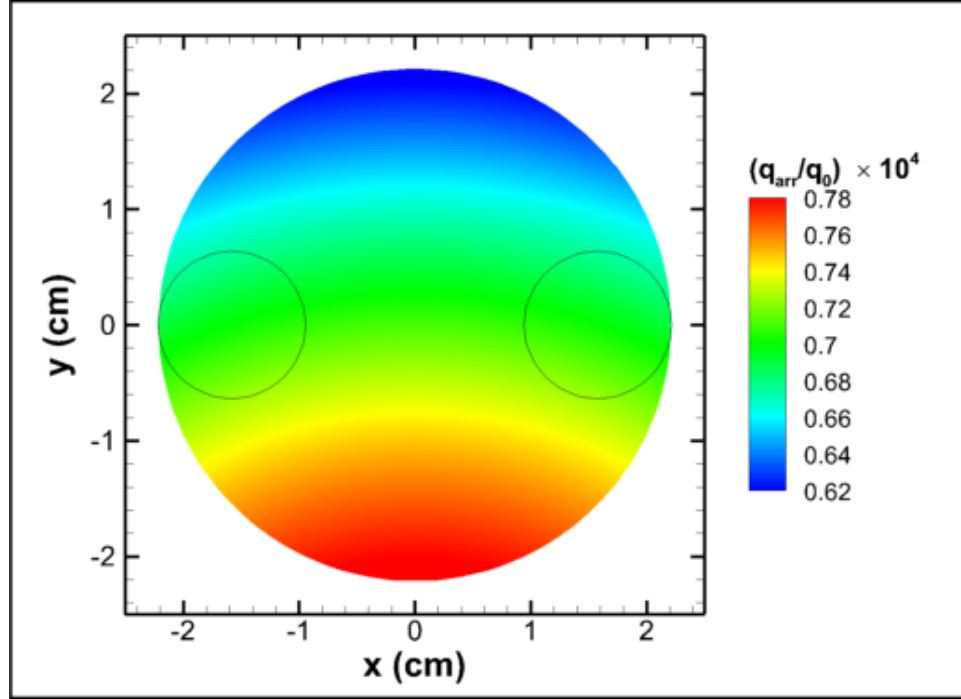
Figure C.4: Equation C.5 for the deposition disc. The outlined circles show the locations of the mirror (left circle) and QCM (right circle).

The result shown in Figure C.4 has assumed that the flow in the effusion cell is free molecular. This is quantified through the Knudsen number which is defined as the ratio of the mean free path to some characteristic dimension of the system, i.e.

$$Kn = \frac{k_B T}{\sqrt{2} \pi d^2 P L}, \tag{C.6}$$

where d is the kinetic diameter of the gas molecule, P and T is the pressure and temperature of the gas, and L is a characteristic dimension. Knudsen numbers greater

than one indicate the flow is free molecular. Knudsen numbers between about 1 and
.01 indicate transitional flow where the rules of free molecular flow do not strictly
apply. The kinetic diameter of water molecules is $d \approx 2.8\text{Å}$ and for the effusion cell
$L \approx 5.23\text{cm}$. Equation C.6 is shown with these values in Figure C.5 for a 300K gas.
As can be seen, pressures of about 1mTorr or less are needed for free molecular flow
in the effusion cell.
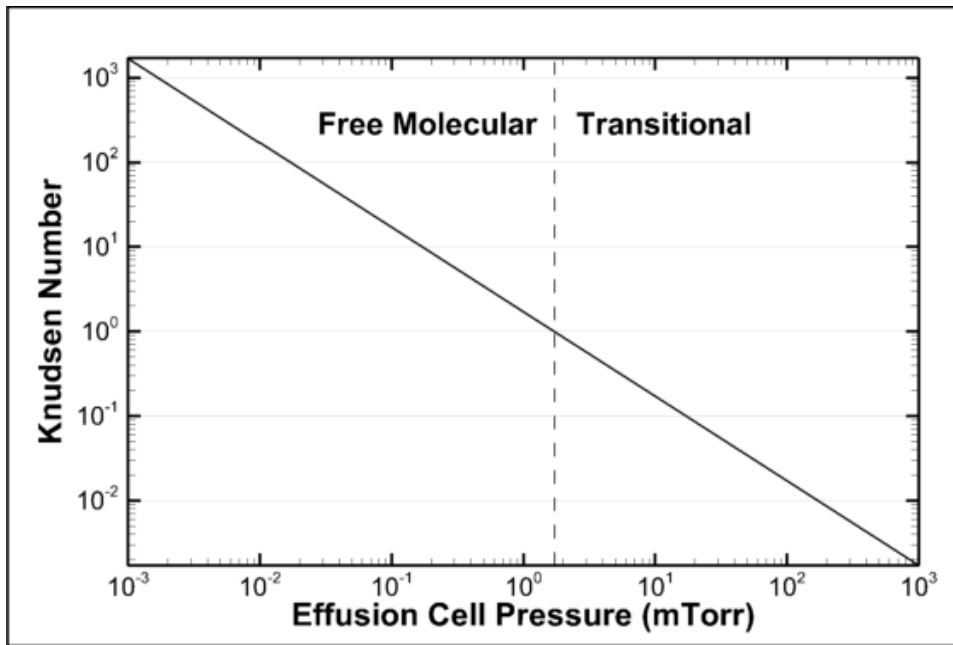
Figure C.5: Knudsen number inside the effusion cell over a range of pressures.

During the testing of the zeolites (see (Rogers (2011))), the mass loss rate (mg/s)
was measured over time. The effusion cell pressure can be found by conservation of
mass in steady state through

$$P = \frac{\dot{m}}{A}\sqrt{\frac{2\pi k_B T}{m}}, \tag{C.7}$$

where $\dot{m}$ is the mass loss rate of the zeolites. This is shown in Figure C.6 for a typical
mass loss rate curve of the zeolites using an approximately 40g sample. Although the
outgassing in the UHV chamber should be faster than what was measured in Figure
C.6 (due to a lower chamber base pressure) the effusion cell pressures can be expected

Figure C.6: A typical mass loss rate curve for a 40g sample measured during testing of the zeolites shown with the predicted effusion cell pressure (Equation C.7).
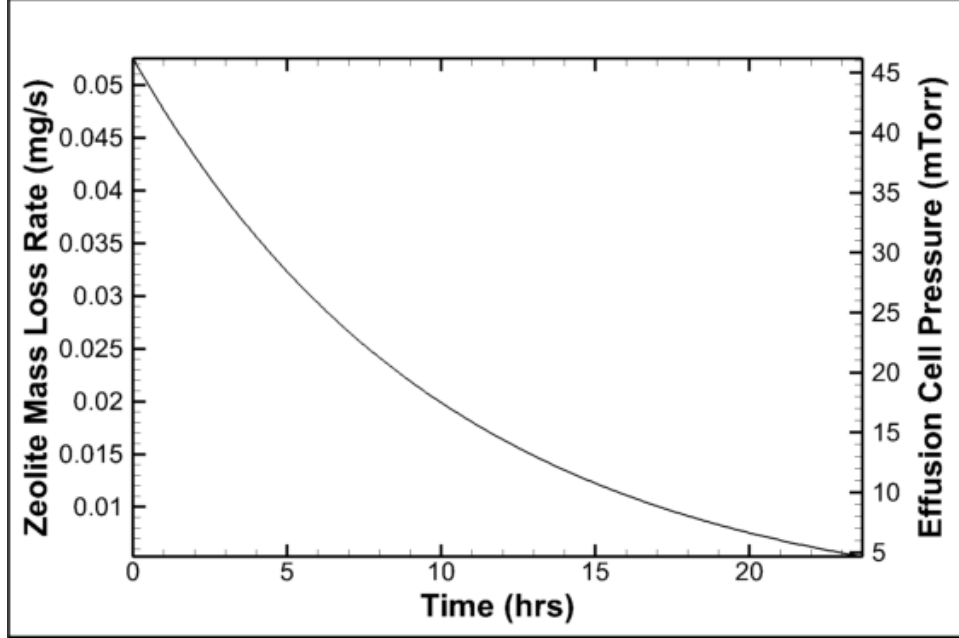
to stay above the $\approx$ 1mTorr range needed for free molecular flow in the effusion cell for quite some time.

Flux distributions from an orifice when the flow is in the transitional regime are more directional than the cosine distribution of free molecular flow. Accordingly, these flux distributions are often fit to a cos^n distribution of the form (Ohring (2001); Thakur and Sahu (2004); Sahu and Thakur (2006))

$$\frac{q_{arr}}{q_0} = \frac{A(n+1)}{2\pi s^2} \cos^n \phi \cos \gamma. \tag{C.8}$$

Consider the setup shown in Figure C.3 for normal incidence deposition such that $\phi_0 = 0°$. In this case, the situation is axisymmetric and can be simulated using the 2D/Axisymmetric DSMC code DS2V (Bird (2005)). Two cases were simulated, the first set the pressure in the effusion cell to 1mTorr to verify free molecular flow at that point. In the second case the pressure was set to 40mTorr, a point near the peak shown in Figure C.6. Images of the two simulations can be seen in Figure C.7.

102
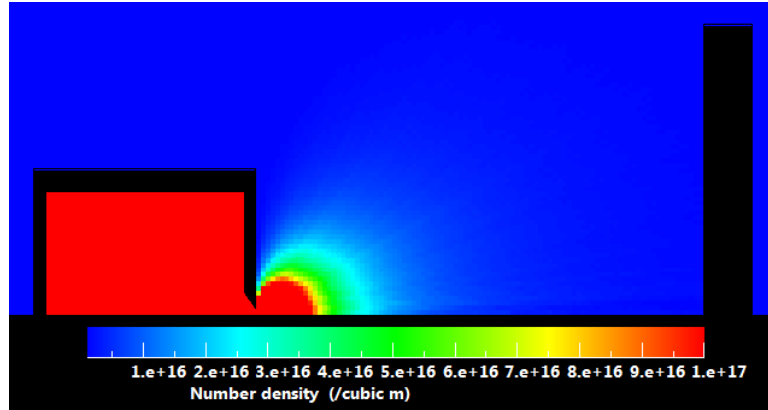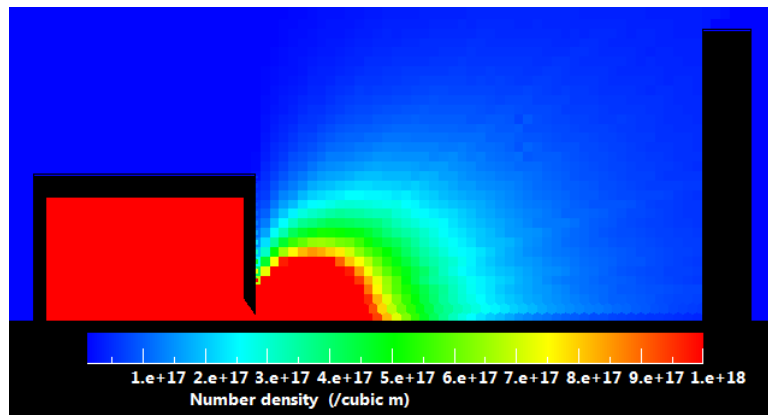
Figure C.7: Screenshots from the DS2V simulation of the effusion cell with pressures of 1mTorr (a) and 40mTorr (b). The black surface on the right in the images is a perfect absorber.

The effusion cell is to scale, but the absorber was placed only 11.8cm away from the orifice (rather than the 18.25cm of the experimental setup) in order to increase the flux arriving on the surface and decrease the statistical error in the simulation. The flux on the absorber is shown in Figure C.8. The flux distribution is already beginning to pull away from the cosine distribution at 1mTorr. At 40mTorr the distribution is significantly different. A non-linear least-squares fitting algorithm (e.g. see (Landau et al. (2007))) was used to fit Equation C.8 to the 40mTorr simulation data shown in Figure C.8. The resulting value for the exponent was $n = 1.35$.
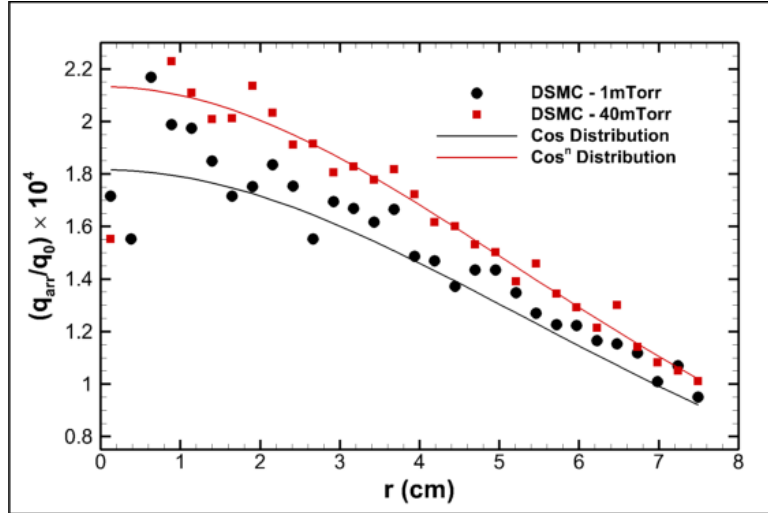
Figure C.8: The flux on the absorber for effusion cell pressures of 1 and 40mTorr. The cosine distribution shown is given by Equation C.5 with $s_0 = 11.8$cm, $A = .08$cm^2, and $\phi_0 = 0$. The cos^n distribution is given by Equation C.8 with $n = 1.35$.

Figure C.9 shows the use of Equation C.8 to analyze the flux distribution on the deposition disc of the experimental setup (Figure C.3) and a side-by-side comparison to the pure cosine distribution is shown in Figure C.10. The total flux on either component is identical. However, it would be desired for the flux to be more uniform over both components. The interferometer only measures the thickness at the center of the mirror while the QCM measures the total mass deposited. As such an accurate determination of the density of the film requires a uniform distribution. One option to get a more uniform distribution would be to modify the effusion cell to produce a more collimated molecular beam. However, a more uniform distribution can be obtained with the current setup. By plotting the flux along the y-axis of Figure C.3, it can be seen that the peak of the distribution actually occurs a few centimeters below the effusion cell axis (see Figure C.11). If the location of the mirror and QCM were set to coincide with the peak of the distribution rather than the effusion cell axis, then a more uniform distribution could be obtained.
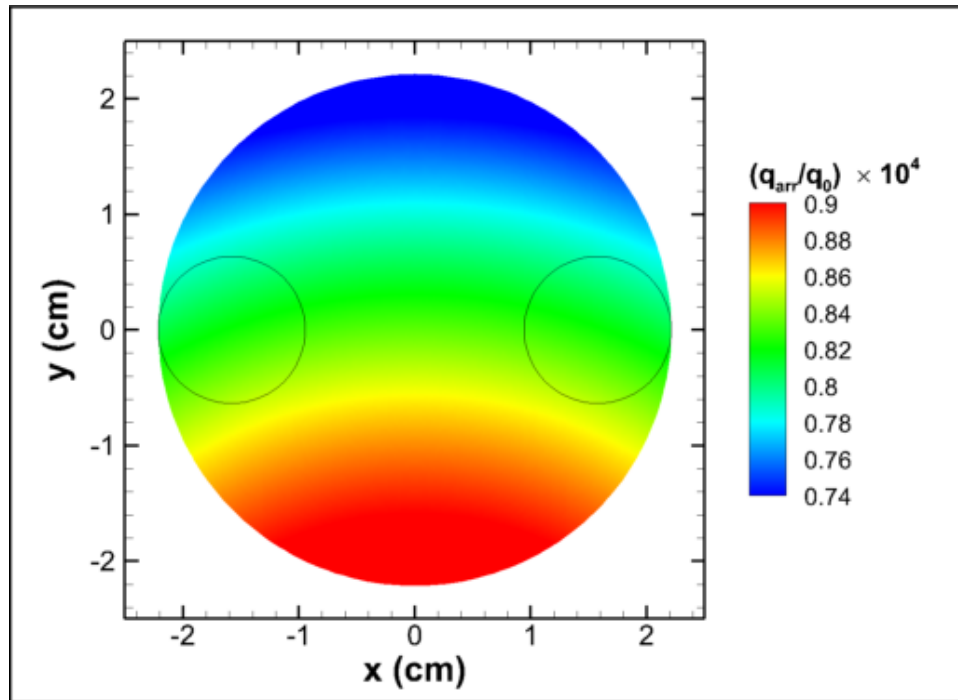
Figure C.9: The predicted flux distribution on the QCM and mirror at 40mTorr using the cos^n distribution of Equation C.8 with $n = 1.35$. The outlined circles show the location of the mirror (left circle) and QCM (right circle).
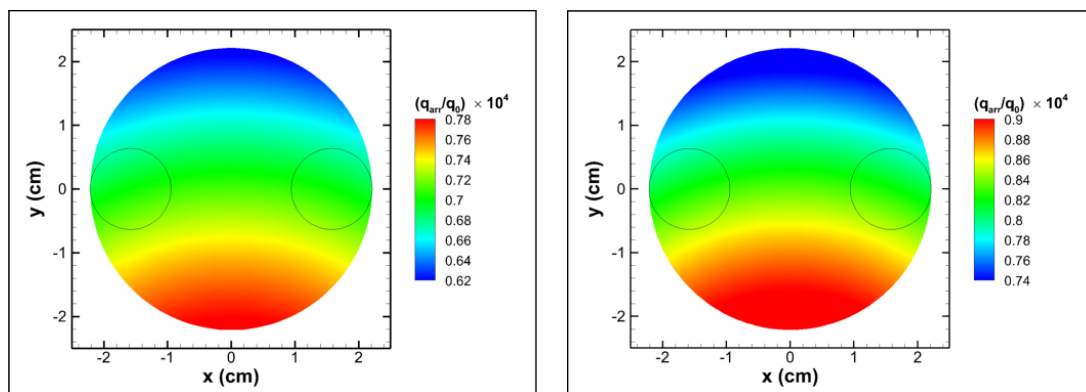

Figure C.10: Side by side comparison of the flux arriving on the QCM and mirror from (a) a pure cosine distribution and (b) the cos^n distribution.
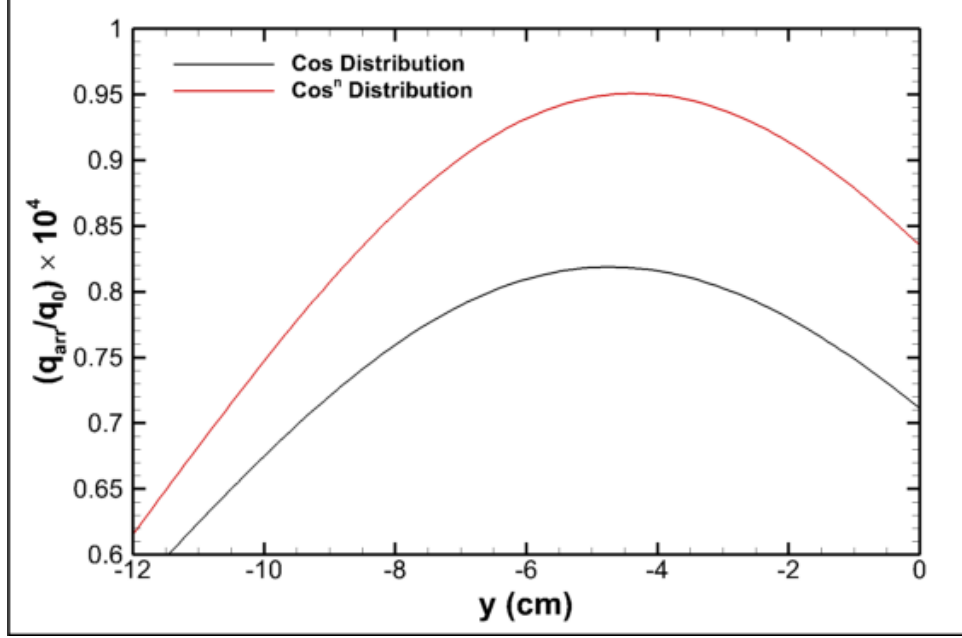
Figure C.11: The calculated flux distributions along the y-axis for a pure cosine distribution and the cos^n distribution with $n = 1.35$. The peak of the distributions occur about 4 to 5cm below the effusion cell axis for the $20°$ angle of incidence.

Shifting the deposition disc down a distance y_0 (Figure C.12) along the y-axis gives

$$\mathbf{s} = r \cos\theta \, \hat{\mathbf{i}} + (r \sin\theta + s_0 \sin\phi_0 - y_0) \, \hat{\mathbf{j}} + s_0 \cos\phi_0 \, \hat{\mathbf{k}},$$

$$\cos\phi = \frac{s_0 + r \sin\theta \sin\phi_0 - y_0 \sin\phi_0}{\sqrt{r^2 + s_0^2 + y_0^2 + 2\left(rs_0 \sin\theta \sin\phi_0 - ry_0 \sin\theta - s_0 y_0 \sin\phi_0\right)}}, \quad \text{and} \quad \text{(C.9)}$$

$$\cos\gamma = \frac{s_0 \cos\phi_0}{\sqrt{r^2 + s_0^2 + y_0^2 + 2\left(rs_0 \sin\theta \sin\phi_0 - ry_0 \sin\theta - s_0 y_0 \sin\phi_0\right)}}.$$

This result of centering the QCM and mirror on the peak of the distributions is seen in Figure C.13. They receive a greater magnitude of flux and a more uniform distribution at the peak location relative to what they receive at the location of the effusion cell axis.
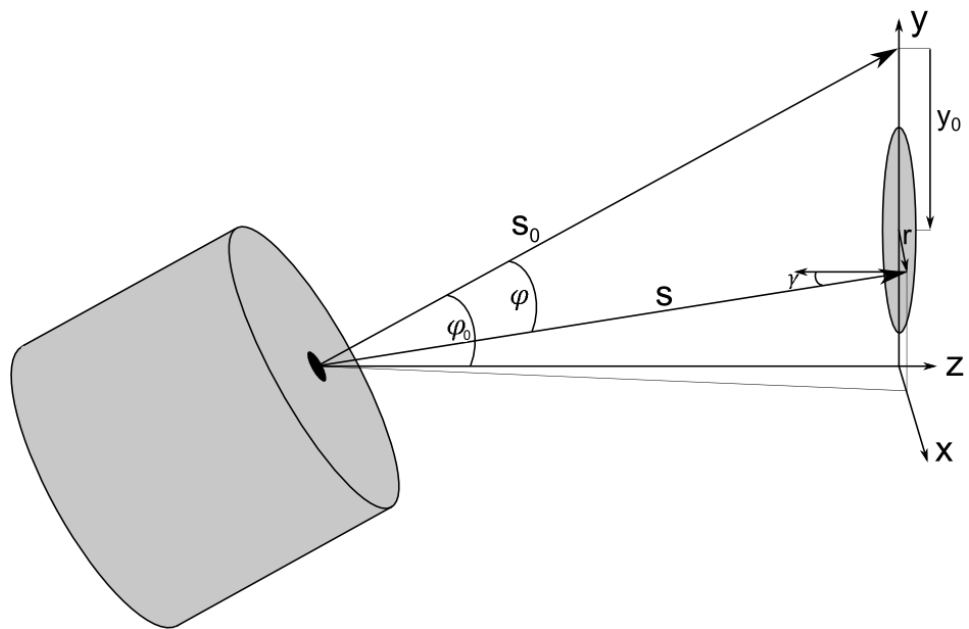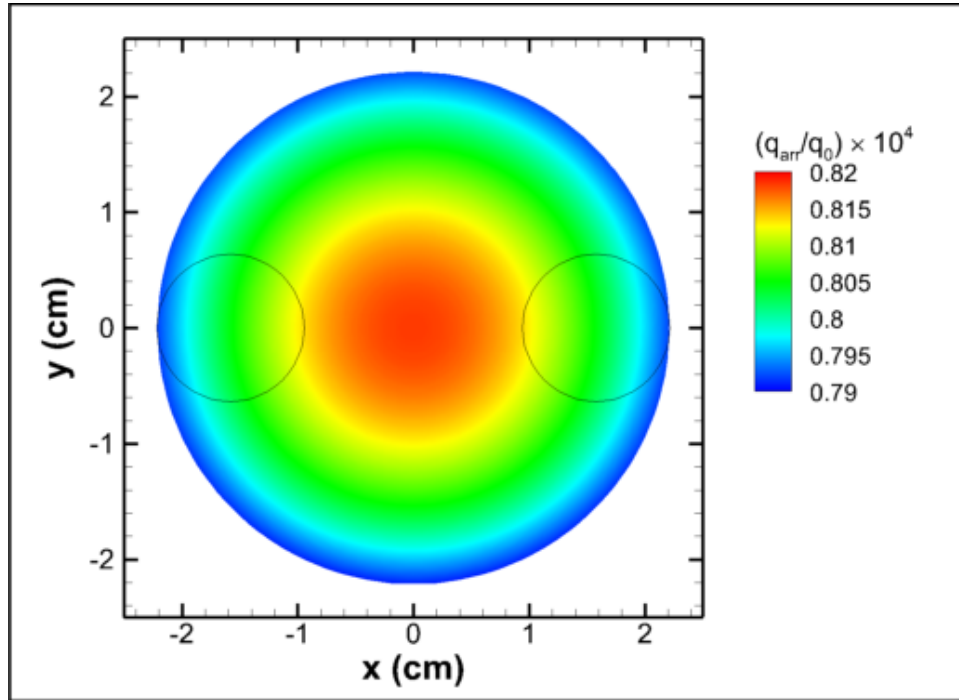
Figure C.12: The coordinate system with the deposition disc being lowered along the y-axis away from the effusion cell axis.

(a)
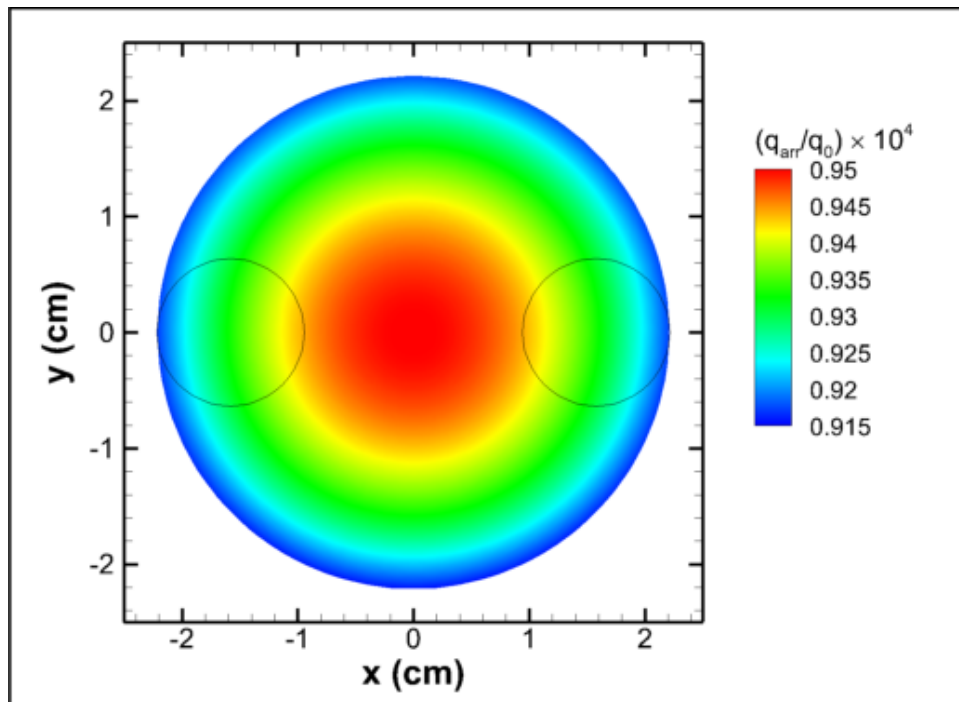
(b)

Figure C.13: The flux from (a) a pure cosine distribution, and (b) the cos^n distribution with the mirror and QCM centered on the peak of the distributions rather than the effusion cell axis.

Appendix D

Discussion on Prevention and Non-Thermal Removal of Cryodeposits

The ideal solution to cryodeposits would be to prevent them from ever forming in the first place. A close second would be to have a non-thermal method of easily removing them. Neither of these calls to mind an obvious method to attain them nor has any practical method been established. There are some ideas that may eventually be made effective, however, and this section discusses some of them.

D.1 Molecular Barrier

One idea to prevent cryodeposits on cryogenic optics is to use a molecular barrier (see Figure D.1). Helium and hydrogen are the only two common gases that do not condense in deep cryovacuum (see Figure 4). Helium is the logical choice of the two as it is the heavier molecule and so can influence impinging contaminant molecules better through molecular collisions. Also, hydrogen is flammable and could cause safety hazards in large concentrations. Use of helium has been considered for

contamination control on satellites in orbit and has been shown that it could be effective at reducing contamination by maintaining a cloud of non-condensable gas around cryogenic optics (Cathcart and Macrossan (1995); Tribble et al. (1996)). In a vacuum chamber though, there are additional considerations. Release of a non-condensable gas in the chamber will raise the chamber pressure which, in a cryogenic vacuum chamber, can also cause undesired heat transfer between warm and cold surfaces. The result is that a molecular barrier will only be practical if it can reduce contamination at flow rates less than the rate that it can be pumped out of the system. This is a very difficult requirement to meet. The pumping speed of helium is notoriously slow and requires specially designed pump systems, such as those used in helium leak detectors, to be pumped efficiently (Hablanian (1997)). Also, a molecular barrier will be completely ineffective unless the helium flow rate is large enough to create a localized high pressure region, a region that is not in free molecular flow, around the surface to be protected.

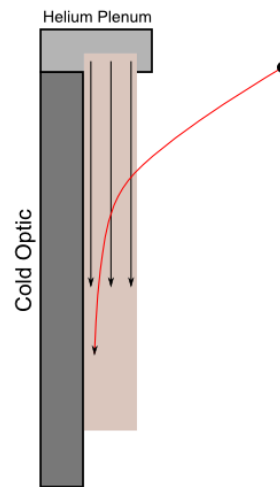**Figure D.1:** Sketch of the molecular barrier or 'helium curtain' idea.

Quantifying what flow rates of helium would be necessary to create an effective molecular barrier is a difficult task. The situation is a mix of free molecular flow (the contaminant background gas) with viscous flow of helium near the cryogenic surface. DSMC is the standard tool for calculation of free molecular and transitional flow

properties. However, it is not well suited to this situation. DSMC operates by directly simulating gas molecules and tracking their movement throughout the flow region. Of course not every gas molecule that would exist in the real gas is simulated, rather each simulated molecule is weighted to represent a large number of real gas molecules. For DSMC to be accurate, the percentage of simulated molecules for each species must be the same as that in the real gas. This leads to problems in situations where the number density of various species is disparate. For the case of the molecular barrier, either the number of simulated helium molecules is too large to be simulated practically (within a run time of days to weeks) or the number of background molecules is too small to give accurate contamination statistics. Several trial and error attempts were made to find a compromise in the simulated to real molecule weight that would allow for a reasonable simulation. The results were limited at best, but did indicate that the helium flow rates would need to be considerably larger than the estimated pumping speed of helium in order to reduce any contamination on the optics. This indication reduced the attractiveness of pursuing the problem further and effectively rules out the molecular barrier as a prevention technique under normal operation of the chambers although it could still find use as an emergency precaution in the event of refrigerator failure.

D.2   Infrared Desorption

Given the resonant character of water ice desorption around the $3\mu m$ O-H stretch band (see section 1.5.2), infrared photodesorption appears to be a promising candidate to remove cryodeposits non-thermally. There are two main quantities to consider here, the amount of energy required to desorb a water molecule and the thermal dissipation time in an ice film. For photodesorption to occur, enough energy must be imparted to a molecule to desorb it before that energy begins to dissipate into the film. The energy required to desorb a molecule is the adsorbtion energy, $E_a \approx .5eV$. The thermal dissipation time for 20K LDA films at $\lambda = 3\mu m$ is about 200ns (Dreisewerd (2003);

Approved for public release; distribution is unlimited.

Prialnik et al. (2004)). Using the nominal $0.94g/cm^3$ density of LDA and the $.3\mu m$ skin depth at this wavelength gives a value of $75mJ/cm^2$ for the threshold fluence. This ballpark value is on the order of the threshold fluences found experimentally at this wavelength (e.g. see Krasnopoler and George (1998); Focsa et al. (2006)). The power density required is then about $375kW/cm^2$. This is a large number that cannot be achieved by many infrared sources and certainly no small sources like infrared LED's that could be easily incorporated into the chamber.

A more practical path to desorption using infrared radiation would be to use it as a selective heat source and induce thermal desorption of the ice films. There are now commercial infrared heaters that emit blackbody radiation peaked at three microns. Such heaters could be placed near optics to induce thermal desorption in ice without overly heating the optical component. This would be preferable to heating the optical component itself as it would eliminate thermal cycling of the optic which causes stress and fracture. However there are still problems with this idea as the heaters would certainly introduce new spectral background into the chamber. As such, testing would have to stop while the contamination removal was taking place and could not continue until the heater cooled back down to wall temperatures. This process would likely take longer than just heating the optic itself.

D.3 Electric Field Effects

Growing ice films through vapor deposition in the presence of a constant electric field can cause a voltage across the ice film by alignment of the dipoles. In some situations 'electric needles' of ice can form. These needles can amplify the electric field and grow more rapidly than in the absence of an external field (Hobbs (1974)). Applying an alternating field should cause the molecules to attempt to reorient themselves with the field and, hence, induce rotations. This is the same principle that a microwave oven operates on. However, a microwave works on water in a liquid state where the molecules are more free to rotate than in a solid state. Microwaves do not work well

on ice where molecules are more tightly bound, as noted by the less efficient defrost cycle. An interesting question is whether an alternating electric field can prevent or reduce cryodeposits by giving impinging molecules additional rotational energy. The experiment discussed in Chapter 4 will be modified to study this by placing a voltage on the mirror and leaving the QCM grounded. For this to be effective, the electric field will have to do its work before a water molecule adsorbs as it will likely have very limited effect once a molecule is bound on the surface.

D.4 Superhydrophobic Coatings

In recent years a number of permanent superhydrophobic coatings have been developed and studied (e.g. see (Vinciquerra (2009); Brinker (2008))). These coatings are different than a normal oil-based hydrophobic coating such as those used to keep a windshield clear in rain because they are based on a geometrical structure. One common design is that of evenly spaced micron scale posts that simulate the very fine hair found on some things in nature. Superhydrophobic means a material where a droplet of water placed on it has a contact angle of greater than $150°$ (see Figure D.2). These coatings are targeted for application to the aerospace community as a

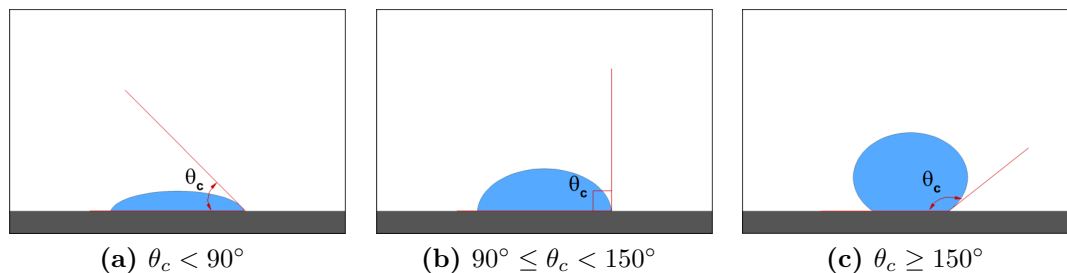**(a)** $\theta_c < 90°$ **(b)** $90° \leq \theta_c < 150°$ **(c)** $\theta_c \geq 150°$

Figure D.2: Illustration of a water droplet on (a) hydrophilic, (b) hydrophobic, and (c) superhydrophobic surfaces.

means of preventing ice build-up on planes and to the commercial optics community for non-fogging displays and goggles. The coatings targeted to the optics community are necessarily optically transparent in the visible region at least. If such coatings are

Approved for public release; distribution is unlimited.

also transparent in the infrared, they could find an application in the space chambers. It is unknown whether any of these coatings would retard frost formation under cryovacuum conditions, but some have been shown to be effective at preventing or reducing frost and ice adhesion at normal conditions (Cao et al. (2009); He et al. (2010)).

Vita

Jesse Labello was born in Baton Rouge, LA to parents Donnie and Marie. He has two brothers, Nicholas and Brady. He graduated from Louisiana State University with a BSc in 2004 and began graduate study at the University of Tennessee Space Institute in Tullahoma, TN in 2005. Graduate research was performed on Arnold Air Force Base, adjacent to UTSI. He received a MSc degree in 2007 for work performed there and continued research in the PhD program. Jesse currently resides in Tullahoma, TN with his wife Amanda. Jesse's free time is spent golfing, boating, playing softball, and exercising. More extreme interests include flying, skydiving, and whitewater rafting.